Imperial College London
Department of Physics

Stochastic Dynamics of Crystal Defects

Thomas D Swinburne

February 2015

Supervised by
Professor Sergei L Dudarev
and
Professor Adrian P Sutton

Submitted in part fulfilment of the requirements for the degree of
Doctor of Philosophy in Physics of Imperial College London
and the Diploma of Imperial College London

Declaration

I herewith certify that all material in this dissertation which is not my own work has been properly acknowledged.

Thomas D Swinburne

Abstract

The state of a deformed crystal is highly heterogeneous, with plasticity localised into linear and point defects such as dislocations, vacancies and interstitial clusters. The motion of these defects dictate a crystal's mechanical behaviour, but defect dynamics are complicated and correlated by external applied stresses, internal elastic interactions and the fundamentally stochastic influence of thermal vibrations.

This thesis is concerned with establishing a rigorous, modern theory of the stochastic and dissipative forces on crystal defects, which remain poorly understood despite their importance in any temperature dependent micro-structural process such as the ductile to brittle transition and irradiation damage.

From novel molecular dynamics simulations we parametrise an efficient, stochastic and discrete dislocation model that allows access to experimental time and length scales. Simulated trajectories of thermally activated dislocation motion are in excellent agreement with those measured experimentally.

Despite these successes in coarse graining, we find existing theories unable to explain stochastic defect dynamics. To resolve this, we define crystal defects through projection operators, without any recourse to elasticity. By rigorous dimensional reduction we derive explicit analytical forms for the stochastic forces acting on crystal defects, allowing new quantitative insight into the role of thermal fluctuations in crystal plasticity.

To Juliette.

Acknowledgements

This is a welcome opportunity to sincerely thank Professor Adrian Sutton and Professor Sergei Dudarev for making my PhD so enjoyable. I feel very lucky not only to have had access to two distinguished scientists with their constant intellectual agility and insight, but also to have had two receptive and responsive mentors who allowed me to take my own course whilst keeping me useful! I am very aware that under different guidance my mild idiosyncrasies could have seriously affected my scientific development, and their role in ensuring this did not happen cannot be overestimated.

The wider community at Imperial College (both Condensed Matter Theory and Theory and Simulation of Materials CDT) and CCFE have been fantastic environments; thanks in particular to Fabian Renn and Mark Gilbert for their endless patience with my numerous coding questions. I would also like to thank my thesis examiners, Dr Peter Derlet and Dr Gunnar Pruessner, for their critical reading of the submitted thesis and their resilience against the numerous spelling mistakes, which I hope have now all been corrected.

Finally, thanks to my parents for their constant support throughout my education and of course to my beloved Juliette for keeping my mind open, often through force.

TDS, February 16, 2015, South Kensington, London

Publications

The work of this thesis has at the time of submission appeared in the following publications:

Theory and simulation of the diffusion of kinks on dislocation lines in bcc metals, T. D. Swinburne, S. L. Dudarev, S. P. Fitzgerald, M. R. Gilbert and A. P. Sutton, Physical Review B, 2013[1].
The work carried out by myself and reported in [1] is presented primarily in sections 4.1 and 5.

Collective transport in the discrete Frenkel-Kontorova model, T. D. Swinburne, Physical Review E, 2013[2].
The work carried out by myself and reported in [2] is presented primarily in section 5.5.

Thermally-activated Non-Schmid Glide of Screw Dislocations in W using Atomistically-informed Kinetic Monte Carlo Simulations, A. Stukowski, D. Cereceda, T. D. Swinburne, T. D., and J. Marian, International Journal of Plasticity, 2015[3].
The work carried out by myself and reported in [3] is presented primarily in section 4.1.4.

The classical mobility of highly mobile crystal defects, T. D. Swinburne, S. L. Dudarev and A. P. Sutton, Physical Review Letters, 2014[4].
The work carried out by myself and reported in [4] is presented primarily in section 6.

Contents

1. Introduction

The plasticity of metals is a subject of critical importance and fundamental interest in physics, engineering and materials science[5]. To understand how metals deform one must investigate crystal defects- specifically, the motion of line-like defects known dislocations, which are subject to intrinsic and extrinsic stresses, long range elastic interactions with other dislocations and atmospheres of point defects, as well as the stochastic influence of thermal vibrations. Whilst there has been sustained effort in coarse graining and calculating the long range elastic interactions between dislocations, the stochastic thermal force has received essentially no direct attention, despite its rôle in driving an immense range of diffusive and thermally activated micro structural processes. This thesis is concerned with modelling and understanding this stochastic thermal force.

The most accurate method for investigating structurally significant ($> 10^6$) numbers of atoms has been fully 'atomistic' molecular dynamics (MD) simulations, which explicitly simulate point particles interacting through an empirical inter atomic potential.

In recent years increasing computational power has allowed material simulations involving millions of point particles interacting through empirical potentials. These simulations, which will be used extensively here, provide valuable insight at the nanoscale but cannot be used beyond nanoseconds and micrometers, obscuring any direct comparison to experiment. As a result, the dynamics from these atomistic simulations must be 'coarse grained': the salient phenomenology must be extracted and preserved as best as possible to be used and understood in treatments where the full atomic structure is implicit, leaving only the crystal defects.

The vast majority of crystal defect modelling is performed with dislocation dynamics (DD) codes[6] which use conservative forces from elasticity

theory supplemented with phenomenological forces derived from atomistic simulation. The equations of motion are first order, deterministic viscous drag laws $\dot{x} = -f/\gamma$, where γ is some friction coefficient. Whilst existing codes are extremely powerful, being able to simulate macroscopic dislocation networks, such a system has no meaning of temperature as it violates the fluctuation-dissipation theorem and thus cannot capture transient bound states or the highly stochastic defect motion widely observed in materials science. Consequently any temperature dependence, often the predominant behaviour of interest in structural settings, can only be recreated in an *ad hoc* manner through parameter fitting with little or no quantitative predictive capability.

This failure of traditional DD codes to accurately capture the stochastic influence of heat is a matter of great concern to the fusion power community, which has a urgent need to understand the ageing of structural metals subject to extreme environments[7]. In these extreme environments and even at room temperature[8] nanoscale defects are observed[9, 10] to have a highly stochastic motion due to the prominence of fluctuating thermal forces. Low dimensional stochastic glide and shape fluctuations, long range correlations due to the elastic field and non-conservative reaction processes are clearly present and observable in real time. Such phenomenology can only be captured through a detailed understanding of the stochastic thermal forces acting on crystal defects.

Previous approaches to the modelling of thermally dominated dynamics all rely on a master equation approach[11, 12, 13] which attempts to assign probabilities to transitions between state vectors characterising the entire system then realising this distribution with a kinetic Monte Carlo (KMC) simulation. Such an approach has a better relationship with the underlying thermodynamics, typically assigning probabilities from a Gibbs distribution. However, despite successes there are many limitations. The 'dynamics' are always constrained to be a set of independent discrete time 'hops' which may bear little relation to the physical processes modelled. Including anything other than contact interactions requires a exponentially divergent state vector; even if the spatial configurations may be coarse grained in a sensible manner enumerating the possible states and assigning transition probabil-

ities becomes extremely complicated even for an isolated dislocation line without long range elastic interactions. On short time scales or highly non-equilibrium situations the assignment of a Gibbsian probability distribution becomes difficult or impossible to justify. The algorithm is extremely difficult to parallelise, and whilst the logarithmic time scale employed improves efficiency it obscures comparison to the real-time trajectories given by experiment.

An alternative approach is the Langevin equation[14, 15], which includes heat on a microscopic scale through the inclusion of fluctuation and dissipation forces, drawn from an appropriate statistical distribution. The resulting system may then be stochastically integrated and it can be shown that the ensemble statistics are Gibbsian in the steady state, yielding equivalent results to a KMC simulation. As ensemble averages are by definition over independent simulation runs, parallelising such a method is trivial. The atomistic degrees of freedom of the defect cores are removed through a *localised* coarse graining procedure which ideally does not affect the long range interactions, in a similar manner to conventional DD codes, though we shall see that the nodal discretisation required to reproduce thermal fluctuations differs significantly. Given such a coarse graining procedure, the typically first order equations of motion may be derived in a well defined manner from the established methods of stochastic dynamics. The coarse grained system possesses a fluctuation-dissipation theorem and therefore a statistically rigorous temperature. We may therefore calculate the long range elastic forces as in DD simulations but extract the thermal dynamics KMC simulations approximate. These characteristics make the Langevin approach an ideal tool to investigate thermally driven micro-structure evolution. However, as in all such microscopic approaches, the coarse graining procedure is a challenging task. We are attempting to integrate out the configurational complexity on atomistic length scales whilst retaining the correct fluctuation statistics required to give practically useful results. This latter point is essential for capturing the thermal dynamics.

This thesis is concerned with accurately modelling thermal defect dynamics and establishing a rigorous, modern theory for the stochastic and dissipative forces on crystal defects, which remain poorly understood despite

their importance in any temperature dependent micro-structural process. In order to unambiguously quantify the effect of thermal fluctuations we primarily demonstrate the efficacy and accuracy of the Langevin equation approach applied to the dynamics of isolated crystal defects. Aside from *internal* elastic interactions we do not treat the long range elastic forces which govern the interaction of dislocations as this large topic is essentially independent to the stochastic thermal force. For specific test cases we focus in particular on screw dislocation lines and edge dislocation loops, as these are commonly considered to be the major arbiters of plastic deformation in (potentially irradiated) structural, body centred cubic metals such as Iron and Tungsten, which are of central interest to the fusion community.

After an introduction to crystal defects and the mathematical foundations of stochastic motion, we present results from novel atomistic simulations of thermally stochastic crystal defects. We develop a simple, crystallographically discrete stochastic dislocation model carefully parametrised from atomistic simulations which can produce dislocation trajectories directly comparable to experiment. We then extend modern statistical mechanics techniques to many-body systems to study the thermodynamics of coarse-grained dislocations. We finally develop a new theory for the stochastic thermal force acting on crystal defects which yields analytical expressions in quantitative agreement with atomistic simulation. We discuss how this agreement is achieved by avoiding an erroneous canonisation of defect coordinates implicit in all previous theories. The future prospects for the developed formalisms are then discussed. Throughout we aim to focus only on new results rather than give summaries of well-established topics for which excellent treatises already exist. In this manner we hope to maintain a brisk readability throughout, only known results when it is essential or at least very useful to the exposition of the ideas developed here. We additionally assume some basic knowledge of crystallography and statistical physics.

2. Dislocations

A first attempt to understand how crystals deform was made by Frenkel[16], who posited that under an applied shear stress a crystal undergoes the bulk shear strain illustrated in Figure 2.1, meaning that the shear stress σ between two crystal planes must vary periodically with the shear displacement strain, i.e. $\sigma = \sigma_0 \sin(k\epsilon)$. Requiring Hooke's law $\sigma = \mu\epsilon$ to hold at small strain, where μ is the shear modulus, one obtains a maximum shear strength of $\sigma_0 \sim \mu/5$[5]. Unfortunately for this elegant picture, it was already known that the shear stress required to induce plastic deformation was known to be at most $\mu/10^3$, going down to $\mu/10^9$ for ductile metals such as Copper.

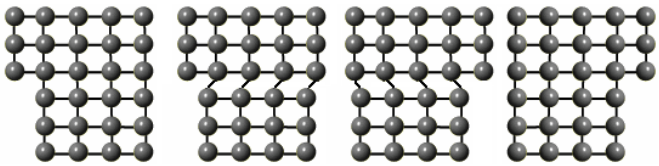

Figure 2.1.: A crystal deforming in Frenkel's model.

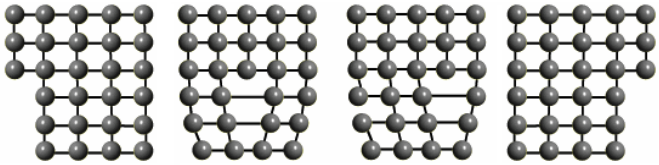

Figure 2.2.: A crystal deforming by dislocation motion.

After many attempts to explain this discrepancy a solution was proposed independently by Taylor, Orawan and others in 1934[17]. It was argued that in contrast to the collective planar movement of Frenkel's model, a real crystal *localises* its deformation into linear regions known as *dislocations*. As shown in Figure 2.2, when the deformation is localised an 'excess'

atomic plane can be transferred from one side of a crystal to another without requiring the bulk motion of atoms, which has a much lower energy cost compared to the collective motion required in Frenkel's theory. This was famously analogised by Bragg to the action of moving a carpet by creating a 'ruck' or ripple at one end and then pushing the ruck rather than trying to slide the whole carpet. As with anything that buckles rather than homogeneously deforming, it is energetically cheaper to heavily deform a small amount of material rather than lightly deforming a large amount of material. This phenomena is central to dislocations and cannot occur in a harmonic system. The comparative ease of dislocation motion was quantified in a seminal paper by Peierls[18], who showed that a dislocation motion requires a shear stress exponentially smaller than Frenkel's σ_0.

It could be argued that Frenkel's ground-breaking work was an attempt to keep crystal plasticity in the realm of linear response, i.e. bulk deformation must be a 'long-wavelength' excitation requiring the collective motion of all the atoms in the system. It is important to note that this did not work, showing immediately that dislocations are intrinsically non-linear objects unsuited to interpretation by conventional field theories. Furthermore, it is very difficult to construct a continuum field theory that possesses both translational invariance and the ability to sustain static, localised excitations[19], especially in more than one dimension. In contrast, this has been shown to be a *generic property* of non-linear *discrete* systems[20], which obviously provide a better approximation to a crystal.

These observations strongly imply that dislocations should be treated as non-linear, discrete objects. This is ill suited to the linear continuum of classical elasticity theory, which treat dislocations as line singularities in a vector field of displacements $\mathbf{u}(x)$ that are regularised either by ad-hoc cut-offs in traditional elasticity[5] or more advanced non-singular methods that suppress singularities through the mapping $\mathbf{u}(x) \to \mathbf{u}(x) + \boldsymbol{\lambda} \cdot \boldsymbol{\nabla}\mathbf{u}(x)$ then applying the same linear field theory[21].

Despite such conceptual failings the predictions of elasticity theory are valid in the far-field when the deformation induced by dislocations is weak and slowly varying, and these interactions are essential to describe realistic

dislocation networks. However, in the current work we focus on accurately coarse graining the stochastic forces acting on thermally fluctuating crystal defects, meaning that we need to be explicitly aware of the non-linear, discrete structure of the dislocation core. This investigation is essentially orthogonal to the valid and important far-field results of elasticity theory. Whilst we will review the topology of dislocation formation and motion, and briefly report initial work on combining the stochastic force with long range elastic interactions, we do not give a review of elasticity theory as there already exist many excellent works on the subject[5, 22, 23].

2.1. Topology and Burgers' vector

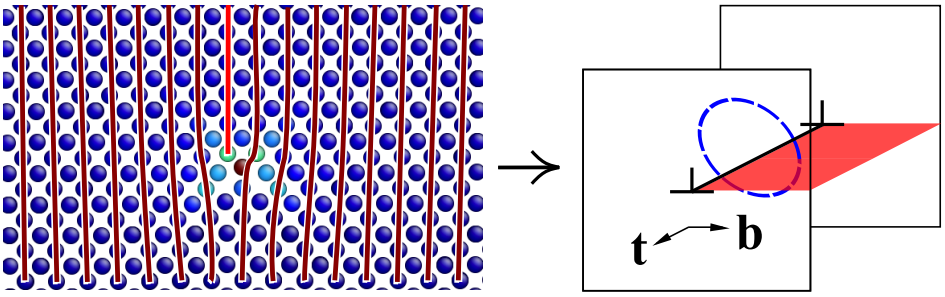

Figure 2.3.: Left: An $\langle 100 \rangle (010)$ edge dislocation in Iron. An edge dislocation is formed through the insertion of an additional semi-infinite crystalline plane. Right: A cartoon of the same edge dislocation line with an example surface bounded by the line and a possible Burgers path, with the line direction $\mathbf{t}$ and Burgers vector $\mathbf{b}$ shown.

Dislocations are defined as *line like* defects in a crystalline material, as distinct from point defects such as impurities, vacancies and self-interstitials atoms or areal defects such as surfaces and grain boundaries. These defects are obviously not mathematically ideal entities, but their configurational space has topological restrictions which can be identified with the topology of points, lines and planes.

For example, a line of point defects do *not* form a line defect, as this linear cluster of point defects can clearly be continuously transformed to any other cluster of arbitrary shape, losing any topological definition. The topology of a line is defined by Jordan's curve theorem[24] in the plane, which states

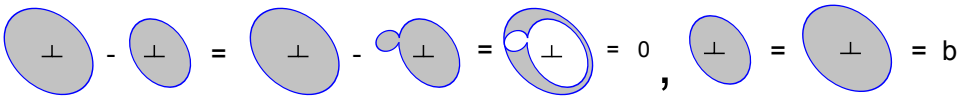

Figure 2.4.: A demonstration of Burgers path independence. The difference between two paths can always be considered as a closed loop enclosing no defects which cannot therefore contribute to the path integral.

that a *closed* curve which does not cross itself (either a loop or a line terminating on the boundaries of the containing plane, which may be at infinity) divides a plane into two distinct regions. An open curve can only be contained in the topology of lines if it is considered as the limiting case of an infinitely thin loop. This two-dimensional construction can be translated to three dimensions if we instead consider the continuous family of concave surfaces bounded by a dislocation line[25] as opposed to the division of a plane.

These considerations give our first main topological constraint, namely that for a linear defect to be a dislocation, i.e. to have the topology of a line, it must either form a closed curve or terminate on the boundaries of an areal defect.

For the dislocation to be a structural defect there must be some topologically identifiable structural 'charge' associated with the line, which we will restrict to be rigid translations by a vector $\mathbf{b}$[1]. In close analogy with Ampère's law[27], the appropriate operation to extract this 'charge' is any closed path around the line, known as a 'Burgers circuit' after its creator. Starting from an arbitrary atom and taking steps only to nearest neighbours, execute a closed path enclosing one or many dislocation lines, in close analogy to an Ampère circuit. As we know the vectors representing nearest neighbour atomic separations of a perfect crystal, for each step calculate the vectorial difference between the 'ideal' vector and the actual step vector, then sum all of these vectors around the path. In a perfect, dislocation-free crystal this would give identically zero, meaning that dislo-

[1]There also exist rotational defects called *disclinations*, but as they can only appear where the violation of bulk translational symmetry induced by this lattice rotation has a controllable energy cost, such as in nanocrystalline metals[26] or liquid crystals[25] we do not consider them here.

cations are defined to be linear defects which contribute a a non-zero result, giving the total displacement $\mathbf{b}$ induced by the defect which will be independent of the details of the path taken. This independence is simple to demonstrate by comparing two paths which both enclose the same dislocations. First, if the paths do not overlap, add a closed loop to one path to give overlap with the second path. The two paths now form a set closed loops which do not enclose any dislocation and thus give no contribution to the net displacement (c.f. Figure 2.4). As these closed loops represent the transformation from one path to the other the path independence is proved.

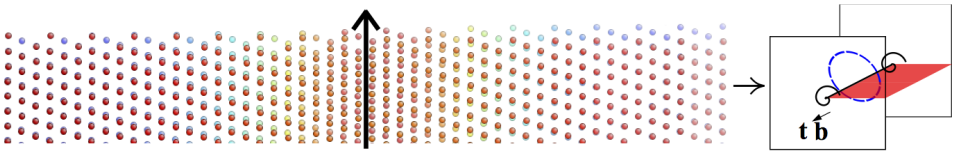

Figure 2.5.: Left: A $(1\bar{1}0)$ plane containing a $1/2\langle 111\rangle[1\bar{1}0]$ screw dislocation overlaid on an unfaulted $(1\bar{1}0)$ plane in Tungsten. We see that the 'disregistry' between the two planes eventually becomes equal to $\mathbf{b}$. Right: A cartoon of the same dislocation.

Crucially, if the Burgers vector $\mathbf{b}$ is not a symmetry operation of the host lattice, an areal stacking fault equal in size to the minimal plane bounded by the dislocation line would develop (the shaded area in Figures 2.3, 2.5), meaning that the dislocation becomes a stacking fault and so can no longer be classified as a line defect. This leads to the second main topological constraint on dislocations- the 'Burgers vector' $\mathbf{b}$ must be a vector of the host lattice[2].

We now have all the topological elements to build arbitrary dislocations. For straight dislocation lines, the relationship between the line direction $\mathbf{t}$ and the Burgers vector $\mathbf{b}$ defines the *character* of a dislocation line; when $\mathbf{b}\cdot\mathbf{t} = \mathbf{0}$ the dislocation is of 'edge' character and the line represents the boundary of an inserted semi-infinite crystallographic plane of normal $\mathbf{b}$ as illustrated in Figure 2.3. When $|\mathbf{b}\wedge\mathbf{t}| = \mathbf{0}$ no additional material is required

[2]Strictly, this restriction only applies to dislocation in the bulk. On surfaces this restriction does not apply, meaning a different partial dislocations can exist depending on the coincident site lattice[28] of grain boundaries or simply the crystallographic character of a free surface.

and we say the line is of 'screw' character- the line represents the centre of a spiralling displacement that translates the crystal by **b** around one circuit; an overlay of a plane containing a screw dislocation and a perfect lattice plane is shown in Figure 2.5.

2.2. Dislocation core structure

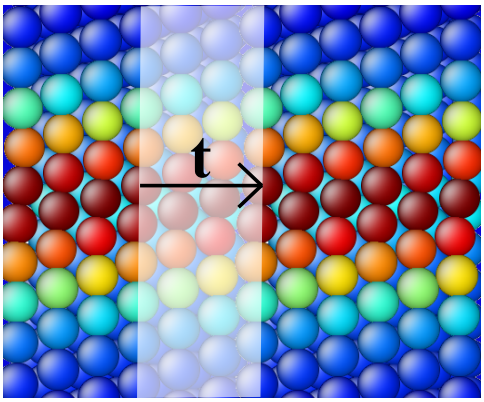

Figure 2.6.: Illustration of a dislocation core 'unit' for a $1/2\langle 111\rangle(1\bar{1}0)$ edge dislocation in bcc Iron. The atoms are coloured from blue to ref by potential energy. We see the core structure repeats over the line direction lattice vector $\mathbf{t} = [11\bar{2}]$.

We have discussed how the non-linear discrete structure of a crystal localises deformation into dislocations, such that the bulk of the inserted half plane, or spiral deformation, is accommodated in a tight *core* region within which a line co-ordinate may be defined. For a straight line dislocation lying along a lattice vector **t**, the core structure will be periodic with a period of **t** by the discrete translational symmetry of the host crystal, as demonstrated in Figure 2.6. This naturally leads to a definition of dislocation core 'units', a concept which we find very useful to understand the dynamics of dislocation cores. Whilst the picture of a compact core is always appropriate for dislocation formation, in some close packed structures such as face centred cubic metals[3] it can be the case that a compact dislocation can be unstable

[3]Hexagonal close packed and face centred cubic crystal structures assume the optimal packing of spheres, meaning in turn that they maximise inter-planar distances[30], which often leads to very glissile dislocation structures with a low stacking fault

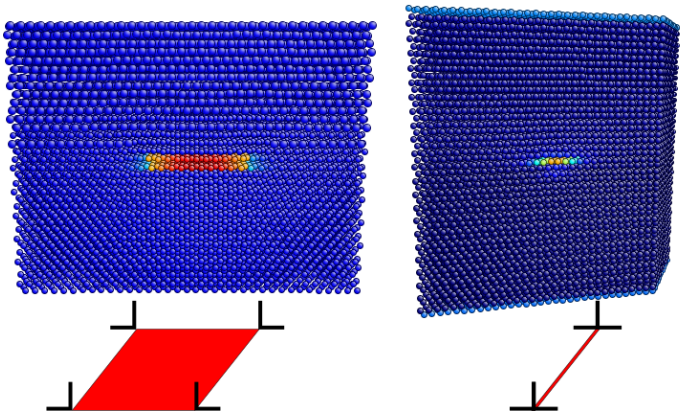

Figure 2.7.: Comparison of dislocation cores. Left: a disassociated $1/2\langle 110\rangle(\bar{1}12)$ edge dislocation in fcc Nickel. The wide stacking fault can clearly be seen, though a line picture emerges far from the core. Right: the compact core of a $1/2\langle 111\rangle(1\bar{1}0)$ edge dislocation in bcc Iron. As bcc metals have no metastable stacking faults dislocation cores never disassociate[29].

to core disassociation: an areal stacking fault band bound by two 'partial' dislocations where only the total Burgers vector is a lattice vector[5]. As shown in Figure 2.7, such an arrangement can either be considered as an areal defect or, far from the stacking fault band, a dislocation line.

Such an ambiguity is to be expected as the topological definitions only strictly apply to ideal mathematical entities rather than real localised deformations. Nevertheless, the two restrictions that a dislocation line must be closed and that the (potentially total) Burgers vector must be a lattice vector remain valid as to violate this would induce a stacking fault of a size only determined by the geometry of the line rather than any 'intrinsic' energetic considerations that lead to a disassociated core.

2.3. Dislocation motion and the kink mechanism

As mentioned above, when $\mathbf{t}, \mathbf{b}$ are not aligned the dislocation requires the addition of material to the host crystal proportional to $M|\mathbf{b} \wedge \mathbf{t}|$, where $\mathbf{b}, \mathbf{t}$ are lattice vectors and L is the shortest distance from the dislocation line

energy[29].

to the boundary of the crystal. As the dislocation line itself can be thought of as the boundary of this additional material, if the dislocation line moves out of the plane defined by $\mathbf{b} \wedge \mathbf{t}$, M will change, meaning that material will have to be added or removed. Such non-conservative motion is known as *climb* motion and is typically facilitated by the biased diffusion of vacancies to the dislocation core[31]. Whilst such a motion is certainly dependent on stochastic thermal forces to drive vacancies over their large migration barriers, these barriers are very large meaning that climb motion is extremely slow (and consequently atomistic simulation becomes extremely expensive). In this thesis we focus on *glide* motion, where dislocation motion is restricted to the *glide plane* of normal $\mathbf{t} \wedge \mathbf{b}$. As glide motion is conservative it occurs much more readily and is the dominant form of dislocation mediated deformation under typical mechanical conditions. Such is the predominance of glide motion, dislocations are typically characterised by their Burgers vector and glide plane in the form

$$\langle \text{Burgers Vector} \rangle \{ \text{Glide Plane} \} \quad \text{Character}, \quad \text{i.e.} \quad \langle 100 \rangle \{ 010 \} \quad \text{Edge}.$$

Glide planes are normally low index lattice planes, as these have the greatest atomic density hence a larger interplanar separation[30]. However, although dislocation glide is a conservative process, the discrete structure of a crystal breaks any continuous translational symmetry, meaning minimum energy configurations will only by invariant after rigid translation by a lattice vector. In between these positions the energy varies periodically under rigid translation. This energy barrier to dislocation motion is called the Peierls barrier and is a rate limiting process in transition metals such as Iron and Tungsten, where the highly directional bonding accentuates this discreteness effect. To see the influence of the Peierls barrier, consider an infinitely long straight dislocation sitting in a minimum energy position. It is clear that the magnitude of the energy barrier to rigid motion will scale linearly with the dislocation line length (the Peierls barrier is defined by unit length) implying that an infinitely long dislocation line has an infinitely large barrier between adjacent minimum energy positions. Nevertheless, the dislocation can still migrate through the a process known as the kink mechanism.

The kink mechanism can be pictured in direct analogy to a first order phase transition, with the initial and final configurations as two phases.

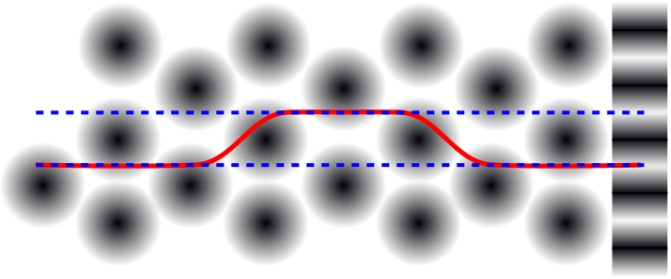

Figure 2.8.: A cartoon of the kink mechanism. The background gradient illustrates the variation of dislocation core energy due to the discrete structure, which when aggregated into motion perpendicular to the bulk line direction gives a one dimension periodic function known as the Peierls barrier, as illustrated in the right hand strip. The red line illustrates the typical kink pair configuration a dislocation line takes to migrate through the periodic landscape. This occurs because the barrier for rigid migration scales linearly with the line length, whilst the kink pair energy is length independent.

Rather than a homogeneous change of state, a small region of the new phases is nucleated, then grows through the motion of domain walls. The domain walls are short segments known as kinks. A more physical picture of the kink mechanism is given in Figure 2.8; we shall explain the kink mechanism in more detail when investigating the atomistic simulation of dislocations.

2.4. Dislocations and Phonon Scattering Theory

All treatments of dissipative defect forces have employed scattering theory to describe the interaction between dislocations and thermal vibrations[32, 33, 5]. As we take an entirely independent approach in this thesis we will only summarise the qualitative results. Indeed, one disadvantage of scattering theory predictions is even under drastic assumptions of dislocation core structures the resulting expressions involve complicated integrals meaning quantitative predictions are sensitive to regularisation techniques such as infra-red/ultraviolet cut-offs or gradient approximations[34] required by all continuum linear field theories[35].

Scattering theories assume that dislocations and phonons are canonical

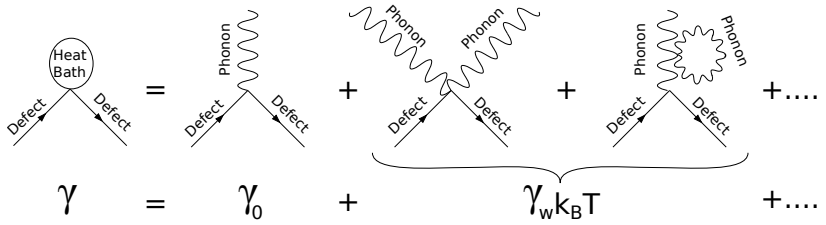

Figure 2.9.: A diagrammatic picture of phonon scattering. The dislocations and phonons are assumed to be well defined entities which to only interact through scattering processes which may be systematically evaluated. Higher order processes contribute terms of higher order in temperature. The linear and quadratic dispersion relations mean the first order term vanishes for subsonic defect speeds. The second process represents a simple 'in-out' scattering and represents the well-known 'Phonon Wind' mechanism.

objects which are non-interacting to quadratic order, meaning each have well defined energy and momenta. One then perturbs this harmonic system with higher order terms giving an expression for γ which be evaluated in a series of scattering events. A cartoon diagrammatic representation is shown in Figure 2.9. Given that we expect the phonon number to be proportional to temperature, it is not surprising that higher order scattering events lead to higher order temperature dependence in γ. However, given the simulation evidence we only consider the zeroth and first order terms γ_0 and $\gamma_{\mathrm{w}}\mathrm{k_B T}$.

As dislocations and phonons are assumed to be canonical in this scattering approach each diagram is dependent on the phase space available for the scattering process they represent. This means the temperature independent term γ_0 is reliant on a one-body absorption or emission, whilst $\gamma_{\mathrm{w}}\mathrm{k_B T}$ includes more typical 'in-out' process. Selection rules for these terms can be derived when noting that we are concerned only with subsonic dislocations moving much slower than the wave speed. Taking a linear phonon dispersion relation $\hbar\omega_{\mathrm{ph}} = \hbar ck$ where c is the wave speed (it turns out that more complicated dispersion relations do not qualitatively affect the results) and a quadratic dislocation dispersion $\hbar\omega_{\mathrm{dis}} = (\hbar K)^2/2m$, we obtain the balance

$$\hbar ck + (\hbar K)^2/2m = (\hbar K + \hbar k)^2/2m \quad \Rightarrow \quad c \simeq \hbar K/m. \tag{2.1}$$

But we know that the dislocation speed is subsonic, i.e. $\hbar K/m \ll c$, meaning

that the above balance cannot be met in the subsonic regime. This is universally invoked in all scattering approaches to conclude that

$$\gamma_0 = 0. \tag{2.2}$$

We will show, through the analysis of extensive atomistic simulations by ourselves and many other researchers that this conclusion is false. This qualitative failure is a manifestation of the erroneous canonisation present in all scattering theories. The main result of this thesis is an entirely new approach that solves these shortcomings.

For higher order processes the phase space is not so restrictive and so continuum theories in general predict that

$$\gamma \simeq \gamma_{\mathrm{w}} \mathrm{k_B T}, \tag{2.3}$$

with the second term in Figure 2.9 being the dominant contribution.

3. Stochastic Motion

3.1. The Langevin and Fokker-Planck equations

The microscopic theory of heat was initiated after experiments in 1827 by Brown[36], who observed that pollen grains floating in water were never stationary, but constantly agitated by numerous weak collisions. In a famous 1905 paper Einstein[37] quantified the observed dynamics, showing how although each grain received no net momentum on average, they were nevertheless displaced by *diffusion*.

Consider observing a particle, submersed in some thermal bath, on a coarse grained time scale τ over which the velocity and position undergo changes $\delta x, \delta \dot{x}$. Within τ the particle will experience a net impulse from thermal collisions I_τ and a net impulse from any external forces $-\tau \partial_x V(x)$. Using these impulses we can write

$$m\delta\dot{x} = -\tau\partial_x V(x) + I_\tau. \tag{3.1}$$

Such an equation can *only* be defined on a coarse grained timescale τ in order to treat thermal collisions statistically. The statistical properties of I_τ are defined through an average over all possible dynamics of the bath, denoted by $\langle ... \rangle$. By the central limit theorem[38] we expect that the bath statistics will be entirely characterised by the average $\langle I_\tau \rangle$ and covariance $\langle I_\tau I_{\tau'} \rangle - \langle I_\tau \rangle \langle I_{\tau'} \rangle$[1]. If the particle has a net momentum, thermal equilibrium requires it give this to the bath (which has none). For small velocities we assume that the rate at which momentum is given to the bath is proportional

[1] The central limit theorem concerns the statistics of ensembles. To hold it requires the ensemble constituents posses a finite standard deviation. In principle it is possible for the forces of some system to have a vanishing or infinite standard deviation, which gives so-called anomalous diffusion[15]. We do not consider these cases as our heat bath is a vibrating crystal, which has well defined elastic properties that demand a non-zero, finite standard deviation in the thermal force.

to the particle momentum, giving an *average* impulse from the bath of

$$\langle I_\tau \rangle = -\gamma \tau \dot{x} + O(\tau^2) \tag{3.2}$$

where γ measures the impulse density of the bath[2]. It is natural to take the rate of thermal collisions to be constant and completely uncorrelated over different time periods, as the bath should be completely incoherent to maximise its entropy. This means we expect the uncertainty in the thermal impulse, characterised by the covariance $\langle I_\tau I_{\tau'} \rangle - \langle I_\tau \rangle \langle I_{\tau'} \rangle$ to only exist for $\tau = \tau'$. In addition, we expect the uncertainty to grow *linearly* with the coarse grained integral τ as we are free to construct this interval from many shorter, completely uncorrelated intervals, meaning the variance will increase linearly. These considerations mean the second moment of the thermal impulse reads

$$\langle I_\tau I_{\tau'} \rangle - \langle I_\tau \rangle \langle I_{\tau'} \rangle = 2\Gamma \tau \delta_{\tau\tau'} + O(\tau^2) \tag{3.3}$$

This last equation shows I_τ has a component of order $\sqrt{\tau}$, meaning the associated force $\lim_{\tau \to 0} I_\tau / \tau$ diverges, a mathematical restatement of the fact we must work on a coarse grained timescale to treat the bath statistically and therefore introduce the concept of temperature. Nevertheless, it is customary to use a force balance equation though it is understood the time differentials are strictly finite differences.

This force balance equation is the celebrated *Langevin equation*[15], devised to model a single realisation of a stochastic process as idealised thermal collisions completely uncorrelated in time. It is derived from (3.1) using the expectation values above. It reads

$$m\ddot{x} = -\partial_x V(x) + -\gamma \dot{x} + \sqrt{2\Gamma}\eta(t), \tag{3.4}$$

where $\eta(t)$ is an idealised white noise, defined by the ensemble averages

$$\langle \eta(t) \rangle = 0 \qquad \langle \eta(t)\eta(t') \rangle = \delta(t - t'), \tag{3.5}$$

[2]For simplicity, we have neglected the possibility that γ depends on position. This is treated below.

where the delta function is understood to be a Gaussian of width $\sim \tau$. To see how temperature emerges in this picture, we look at the ensemble average dynamics. Taking some function $\phi(x(t), \dot{x}(t))$, where $x(t), \dot{x}(t)$ solves a particular realisation of (3.4), we define

$$\Phi(x, \dot{x}, t) = \langle \phi(x(t), \dot{x}(t)) | x(0) = x, \dot{x}(0) = \dot{x} \rangle. \tag{3.6}$$

Note that $\Phi(x, \dot{x}, t)$ depends on the *past* position and velocity $x, \dot{x}$. The evolution equation of $\Phi(x, \dot{x}, t)$ may be evaluated using (3.4), recalling that $\eta(t)$ is of order $\sqrt{\mathrm{d}t}$ to write

$$\begin{aligned} \partial_t \Phi(x, \dot{x}, t) &= \dot{x}\partial_x \Phi - (\partial_x V(x) + \gamma)/m \partial_{\dot{x}} \Phi + \Gamma \partial_{\dot{x}}^2 \Phi & (3.7) \\ &= \hat{L}\Phi. & (3.8) \\ \Rightarrow \Phi(x, \dot{x}, t) &= e^{\hat{L}t} \Phi(x, \dot{x}, 0) & (3.9) \end{aligned}$$

This is the so-called *backwards* Kolmogorov equation (BKE) for the evolution of the ensemble average of a smooth function. An evolution equation for a function which depends on the current time and position can be obtained by considering the evolution of the probability density $\rho(x, \dot{x}, t)$, which was initially $\rho(x, \dot{x}, 0)$. We average over all initial conditions with ρ_0 allowing us to write

$$\begin{aligned} \int \rho(x, \dot{x}, 0) \Phi(x, \dot{x}, t) \mathrm{d}x \mathrm{d}\dot{x} &= \int \rho(x, \dot{x}, t) \Phi(x, \dot{x}, 0) \mathrm{d}x \mathrm{d}\dot{x} \\ &= \int e^{\hat{L^*}t} \rho(x, \dot{x}, 0) \Phi(x, \dot{x}, 0) \mathrm{d}x \mathrm{d}\dot{x}, \end{aligned} \tag{3.10}$$

where $\hat{L}^*$ is the adjoint (in the space of square integrable functions, where ρ must reside) of the functional operator $\hat{L}$. This holds for all smooth functions Φ and thus $\rho(x, \dot{x}, t) = e^{\hat{L^*}t} \rho(x, \dot{x}, 0)$, meaning

$$\begin{aligned} \partial_t \rho &= \hat{L}^* \rho, & (3.11) \\ &= \partial_x (\dot{x}\rho) + \partial_{\dot{x}} \left((\partial_x V(x)/m + \gamma \dot{x}/m)\rho + \Gamma/m^2 \partial_{\dot{x}} \rho \right) & (3.12) \end{aligned}$$

which is the famous *Fokker-Planck equation* for the distribution function ρ. It can be shown directly that the steady state equation $\partial_t \rho_\infty = 0$ is solved by

$$\rho_\infty = \exp -\frac{\gamma}{\Gamma} \left(\frac{m}{2} \dot{x}^2 + V(x) \right) / Z \tag{3.13}$$

which becomes identical to Gibbs' distribution if and only if

$$\Gamma = \gamma \mathrm{k_B T}, \tag{3.14}$$

a result known as the fluctuation-dissipation theorem. Using this relationship in (3.12) we see that whilst the temperature T characterises *equilibrium*, the impulse density γ characterises *non-equilibrium*. This statement is made even clearer if we rewrite (3.12) in terms of the deterministic probability current $\mathbf{j} = (\dot{x}\rho, -\partial_x V(x)/m\rho)$,

$$\dot{\rho} = \partial_t \rho + \boldsymbol{\nabla} \cdot \mathbf{j} = (\gamma/m)\partial_{\dot{x}} \left(\dot{x}\rho + (\mathrm{k_B T}/m)\partial_{\dot{x}}\rho\right) \tag{3.15}$$

showing that probability flux out of the system is proportional to γ.

3.1.1. Strong Damping Limit

It is often the case that the dynamics of a stochastically agitated particle can be partially integrated, allowing a statistical description that depends only on position. This *strong damping* regime is much easier to handle mathematically and thus very attractive for modelling purposes. Happily, it also happens to be legitimately applicable in a wide range of cases where inertia is not observed to play an important role. To obtain a condition for the strong damping limit, consider the variable $w = x + m\dot{x}/\gamma$. The dynamics of w follow

$$\dot{w} = -\partial_x V(x)/\gamma + \sqrt{\frac{2\mathrm{k_B T}}{\gamma}}\eta(t). \tag{3.16}$$

This would be a first order stochastic equation for w providing

$$\partial_x V(x) \simeq \partial_w V(w), \tag{3.17}$$

which requires that the force does not vary significantly over the thermal mean free path $\sim m\dot{x}/\gamma$. As $\gamma \to \infty$ this will be true for all potentials, hence the 'strong damping' label, but in principle this can apply anywhere (3.17) holds. The associated ensemble dynamics can be evaluated by working with the orthogonal coordinates $(w = x + m\dot{x}/\gamma, z = \dot{x} - mx/\gamma)$. In these

coordinates the Fokker-Planck equation reads

$$\begin{aligned}&(1+\frac{m^2}{\gamma^2})\partial_t\rho(w,z,t)\left(\partial_w-\frac{m}{\gamma}\partial_z\right)\left(z+\frac{m}{\gamma}w\right)\rho-\left(\frac{1}{m}\partial_z+\frac{1}{\gamma}\partial_w\right)\left(\partial_w-\frac{m}{\gamma}\partial_z\right)V\rho\\ =\;&\frac{\gamma}{m}\left(\partial_z+\frac{m}{\gamma}\partial_w\right)\left(\frac{mw}{\gamma}+z\right)\rho+\frac{\gamma}{m}\left(\partial_z+\frac{m}{\gamma}\partial_w\right)^2\rho,\end{aligned}\tag{3.18}$$

which upon integration over surfaces of constant w gives to leading order in $1/\gamma$

$$\partial_t\rho(w,t)=\frac{1}{\gamma}\partial_w\left(\partial_w V(w)\rho+\mathrm{k_B T}\partial_w\rho\right)+O(1/\gamma^2),\tag{3.19}$$

which is commonly referred to as the Smolchowski equation. In the absence of any external forces we obtain the Diffusion equation

$$\partial_t\rho(x,t)=\frac{\mathrm{k_B T}}{\gamma}\partial_x^2\rho(x,t)=D\partial_x^2\rho(x,t),\tag{3.20}$$

demonstrating the Einstein relation $D=\frac{\mathrm{k_B T}}{\gamma}$

3.1.2. State dependent damping

We saw above how stochastic collisions can only strictly be defined as impulses. Furthermore, it is not possible to unambiguously integrate (3.4) with standard methods as a stochastic 'force' has unbounded variation, giving different continuum limits depending on method of integration (rectangle, trapezium etc) used. We have implicitly used the *Îto* interpretation throughout, where only initial values need be used to propagate in time-the rectangle $\delta\tau x(\tau)$ is used for the interval $\tau,\tau+\delta\tau$. A more physical approximation is to use the *Stratanovich* interpretation which is sensitive to both initial and final values (c.f. Hamilton's principle) where the trapezium $\delta\tau/2(x(\tau)+x(\tau+\delta\tau))$ is used for the interval $\tau,\tau+\delta\tau$. However, the strictly Markovian form of the Îto interpretation is essential to safely convert between ensemble dynamics and individual realisations of the Langevin equation. Thankfully, it can be shown that the Stratonovich interpretation can be converted to an Îto Langevin equation of the form[39]

$$m\ddot{x}=-\partial_x V(x)+\partial_x\gamma(x)/2-\gamma\dot{x}+\sqrt{2\gamma(x)\mathrm{k_B T}}\eta(t),\tag{3.21}$$

As is clear, this only affects the equation of motion when $\gamma(x)$ depends on position. It is simple to show that the appropriate distribution function in the strong damping limit is

$$\partial_t \rho(x,t) = \partial_x \left(\frac{1}{\gamma(x)} \left(\partial_x V(x) \rho + \mathrm{k_B T} \partial_x \rho \right) \right), \tag{3.22}$$

and so does not affect the equilibrium distribution ρ_∞. This emphasises the fact that $\gamma(x)$ is concerned with non-equilibrium (i.e. dynamical) system properties.

3.1.3. Projection Operators for Dimensional Reduction

Liouville's theorem states that the volume of phase space an isolated system fills is conserved under Hamiltonian dynamics[14]. This is expressed in the continuity equation $\partial_t \rho + \boldsymbol{\nabla} \cdot \mathbf{j} = 0$, i.e. the Fokker-Planck equation (3.15) with $\gamma = 0$.

However, if we only determine the state of a partition of this system the phase space volume of this partition does, and should, change under the Hamiltonian evolution of the entire system. The motion of the undetermined variables can only be treated statistically. It is typically appropriate to invoke the central limit theorem characterised by two variables, $\mathrm{k_B T}$ and γ. The *effective* microscopic evolution equation for the degrees of freedom we measure evolves according to a stochastic equation of motion possessing fluctuation and dissipation operators. This replacement of many degrees of freedom by a statistical distribution is in essence is the nature of thermal motion. Brown could only track the pollen grains, not the water. The grain's motion thus appeared stochastic but with well defined averages.

In a theoretical treatment we realise this partition of phase space through a projection operator $\mathbf{P}$, which by definition is idempotent i.e. $\mathbf{P}^2 = \mathbf{P}$. A simple example is the position of a particular particle from a set of particle positions $\{x_i\}_{i=0..N}$. Constructing the state vector $\mathbf{X} = \oplus_i x_i$ the projection operator for the $\mathrm{m^{th}}$ particle would be $P_i = \delta_{im}$.

In a more abstract setting $\mathbf{P}$ is not necessarily a vector, but an operator

P in the system's Hilbert space $\mathbb{H}$. The variables that we wish, or are able to, determine lie in a smaller Hilbert space $\mathbb{G} \in \mathbb{H}$. The projection operator projects any function in $\mathbb{H}$ onto $\mathbb{G}$.

The following derivation varies slightly from standard treatments[40, 41] but arguably obtains the desired result more directly. We start from the adjoint Liouville equation for a function $\phi \in \mathbb{H}$ which depends on the entire system state, then derive a formally exact equation for the projected function $\phi_s = P\phi \in \mathbb{G}$ which depends on the known initial conditions ϕ_s^0 of the tracked variables and the unknown initial conditions ϕ_f^0 of the untracked projection $\phi_f = (1-P)\phi = Q\phi \in \mathbb{H}/\mathbb{G}$. The subscripts s, f anticipate a common and physical approximation, where the tracked variables are 'slow' compared to the 'fast' untracked variables. By defining the initial conditions for ϕ_f^0 statistically we obtain a non-Markovian Langevin equation for ϕ_s. In the limit where the tracked variables evolve much more slowly the equation of motion becomes directly analogous to the stochastic equations treated above. We write the adjoint Liouville equation using the operator L as

$$\partial_t \phi(t) = \mathrm{L}\phi(t) = \mathrm{L}\phi_s(t) + \mathrm{L}\phi_f(t). \tag{3.23}$$

To give time reversibility $\mathrm{L}^T = -\mathrm{L}$. The projected equations of motion read

$$\partial_t \phi_s(t) = P\mathrm{L}\phi_s(t) + P\mathrm{L}\phi_f(t), \quad \partial_t \phi_f(t) = Q\mathrm{L}\phi_s(t) + Q\mathrm{L}\phi_f(t), \tag{3.24}$$

which admit a formally exact solution for $\phi_f(t)$ as

$$\phi_f(t) = e^{tQ\mathrm{L}}\phi_f^0 + \int_0^t e^{(t-\tau)Q\mathrm{L}} Q\mathrm{L}\phi_s(\tau)\mathrm{d}\tau = e^{tQ\mathrm{L}}\phi_f^0 + \int_0^t e^{\tau Q\mathrm{L}} Q\mathrm{L}\phi_s(t-\tau)\mathrm{d}\tau. \tag{3.25}$$

These may be substituted into the $\phi_s(t)$ equation to give

$$\partial_t \phi_s(t) = P\mathrm{L}P\phi_s(t) + \int_0^t P\mathrm{L}Qe^{\tau Q\mathrm{L}Q} Q\mathrm{L}P\phi_s(t-\tau)\mathrm{d}\tau + P\mathrm{L}Qe^{tQ\mathrm{L}Q}\phi_f^0, \tag{3.26}$$

where we have used the identities $P^2 = P, Q^2 = Q$ which imply $P\phi_s = \phi_s, Q\phi_f = \phi_f$ and $e^{\tau Q\mathrm{L}} = e^{\tau Q\mathrm{L}Q}$. The first term on the right hand side is clearly the 'internal' dynamics within the projected subspace and is un-

affected by distribution of $Q\phi_f^0$. We therefore label $PLP = \mathrm{L}_s$ and in a similar fashion $Q\mathrm{L}Q = \mathrm{L}_f$. The terms $P\mathrm{L}Q = -(Q\mathrm{L}P)^{\mathrm{T}}$ clearly couple the projected subspace to the 'bath' dynamics.

So far we have only manipulated the Liouville equation. To obtain a generalised non-Markovian Langevin equation we must consider the case that $\phi_{s,f}$ are composed of (possibly non-canonical) momentum and position variables, i.e. $\phi_{s,f} = (p_{s,f}, x_{s,f})$. To introduce the concept of temperature and dissipation we must treat the unknown initial conditions ϕ_f^0 statistically. For a total system energy[3]

$$H = \frac{p_s^2 + p_f^2}{2m} + V(x_s, x_f), \tag{3.27}$$

the natural initial distribution for (p_f^0, x_f^0) which maximises the system entropy subject to the constraints that initially $(p_s, x_s) = (p_s^0, x_s^0)$ is the partial partition function

$$\langle ... \rangle = \int \mathrm{d}x_f \mathrm{d}p_f ... \exp \beta(V(x_s^0, x_f) + p_f^2/2m), \tag{3.28}$$

where $\beta = 1/\mathrm{k_B T}$. This gives the ensemble averages

$$\langle x_f^0 \rangle = 0, \quad \langle p_f^0 \rangle = 0. \tag{3.29}$$

If $\langle x_f^0 \rangle \neq 0$ then the tracked dynamics would have a systematic bias even at zero temperature, inconsistent with our definition that the bath is unbiased. The second moment then reads

$$\langle (x_f^0)^2 \rangle = \frac{\mathrm{k_B T}}{k}, \quad \langle (p_f^0)^2 \rangle = m\mathrm{k_B T}, \tag{3.30}$$

where we have invoked the equipartition result $\langle p^2 \rangle / 2m = \mathrm{k_B T}/2$ and $k\langle x^2 \rangle / 2 = \mathrm{k_B T}/2$ for some curvature k. The bath dynamics may have a more complicated higher moments but in order to keep a static temperature we assumed these can all by expressed (by e.g. Wick's theorem) in terms of the two point correlations (3.30).

[3] For simplicity we have written the Hamiltonian in a simply partitioned system of particles. The significantly more complicated case of crystal defects are treated at the end of this thesis.

In addition, we further assume that the untracked variables only induce a force on the tracked variables, not any drift motion. This means that PLQ couples only to p_s, a physical assumption as otherwise dissipation could occur without any motion. We are now in a position to define the stochastic force $\eta(t)$ as

$$\eta(t) = PLQe^{t\mathrm{L}_f}p_f^0, \tag{3.31}$$

where by the above assumptions $\eta(t)$ has the statistical properties

$$\langle\eta(t)\rangle = 0, \quad \langle\eta(t+\tau)(\eta(t))^{\mathrm{T}}\rangle = -PLQe^{\tau\mathrm{L}_f}\langle(\phi_f^0)^2\rangle QLP = \mathrm{k_B T K}(\tau), \tag{3.32}$$

which defines the 'memory kernel' $\mathrm{K}(t)$ as the time autocorrelation of η divided by temperature, which represents a non-Markovian generalisation of the fluctuation-dissipation theorem. We note that $-\mathrm{K}(\tau)$ is closely related to the term $PLQe^{\tau QL}QLP$ occurring in the formally exact equation of motion (3.26), and $\mathrm{K}(\tau)$ can also be thought of as the time autocorrelation of the total force as $\langle \mathrm{L}_s\phi_s\rangle \equiv \mathrm{L}_s\phi_s$.

After all these manipulations, we can combine (3.26) with the above definitions, using the Liouvillian results inside the projected subspace ($\mathrm{L}_s p_s = -\langle\partial_{x_s}V(x_s,x_f)\rangle = -\partial_{x_s}F(x_s)$ and $p_s = m\dot{x}_s$) to obtain the more recognisable non-Markovian Langevin equation

$$m\ddot{x}_s = -\partial_{x_s}F(x_s) - \int_0^t \mathrm{K}(\tau)\dot{x}_s(t-\tau)\mathrm{d}\tau + \eta(t), \tag{3.33}$$

which represents the first main result of this section. We note that the velocity dependent dissipation term $-\int_0^t \mathrm{K}(\tau)\dot{x}_s(t-\tau)\mathrm{d}\tau$ is ensured to be negative by the time reversibility of $\mathrm{L}^{\mathrm{T}} = -\mathrm{L}$ and the positivity of $\mathrm{k_B T} > 0$. Finally, we investigate the timescale separated regime that often closely approximates physical reality. We have seen that the tracked dynamics evolve on a timescale $\tau_s \sim |PLP|^{-1}$ and the untracked on a timescale $\tau_f \sim |QLQ|^{-1}$. Let us take the ratio of these two timescales to be a factor $\tau_f/\tau_s = \lambda \ll 1$, implying the tracked variables are very slow compared to the untracked variables. Whilst $\dot{x}_s(t-\tau)$ has a leading order term $\sim \tau/\tau_s$, by expanding the exponential it is clear that the first time dependent part of $\mathrm{K}(\tau)$ is of order τ/τ_f^3; to give a scale separation to leading order we therefore only need to

assume that over a time $\tau_f^3 < \tau_f \ll \tau_s$ $\dot{x}_s(t)$ is constant. We can then take $\dot{x}_s(t-\tau)$ outside of the convolution in (3.33) through the approximation

$$\mathrm{K}(\tau)\dot{x}_s(t-\tau) \sim \gamma \dot{x}_s(t)\delta(\tau), \quad \gamma \equiv \int_0^\infty \mathrm{K}(\tau)\mathrm{d}\tau, \tag{3.34}$$

which represents the second main result of this section, defining γ from 'first principles' i.e. the underlying dynamics of the entire system. We now finally obtain the standard Langevin equation

$$m\ddot{x}_s = -\partial_{x_s} F(x_s) - \gamma \dot{x}_s + \eta(t), \quad \langle \eta(t+\tau)\eta(t)\rangle = \mathrm{k_B T}\gamma\delta(\tau). \tag{3.35}$$

This equation still has an extremely large phenomenological reach and we will employ further techniques to both simulate its dynamics and theoretically predict and interpret its results in later sections. The main result of this thesis will be an explicit form for the force autocorrelation $\mathrm{K}(\tau)$ for a wide range of crystal defects and dislocations, allowing direct evaluation of γ from the projected defect force. However, we now return to the stochastic motion of dislocations in atomistic simulation,which provide the physically important data that we wish to interpret using the techniques outlined above.

4. Atomistic simulations in bcc Metals

It is clear that numerical methods essential when trying to understand the detailed atomic structure and dynamics. The most popular quantum mechanical approach is density functional theory[42] (DFT), which exploits an isomorphism between the ground state wave function and ground state electron density to approach the many-body Schrödinger equation variationally, often allowing efficient evaluation of complex structures and energy landscapes. However, even with significant simplifications to the underlying Hamiltonian such techniques are currently limited to less than 500 metallic atoms, meaning that they only be used to inform coarse grained models of atomic interaction. At present, short segments of screw dislocation cores can be simulated in DFT allowing accurate parametrisation of the Peierls barrier and dislocation formation energies, along with similar properties for point defect formation energies, as well as bulk properties such as the lattice parameter and bulk modulus[43]. It is the aim of any coarse grained model to quantitatively reproduce these features as accurately as possible.

Born and Oppenheimer[44] were the first to realise that much insight into *atomic* rather than *electronic* motion can be gained if one works on a coarse grained timescale of femtoseconds, where the electronic co-ordinates are assumed to instantaneously assume the minimum energy configuration consistent with the given atomic positions. In this way one can argue that only the atomic positions need be retained along with some phenomenological interaction potential which attempts to recreate the energy landscape generated by the full quasistatic quantum mechanical system.

In practice, molecular dynamics (MD) simulation aims to use an interatomic potential that best reproduces the features from DFT. The simplest

choice is some isotropic pair potential $\phi(r)$ such that

$$V = \sum_{ij} \frac{1}{2}\phi(|\mathbf{x_i} - \mathbf{x_j}|), \tag{4.1}$$

where the factor of $1/2$ accounts for the exchange symmetry between i, j. Despite the appeal of this simple and efficient form, it can be shown that this can only produce two independent elastic constants, meaning immediately that the elastic properties of cubic crystals, which require three, cannot be captured. This is not surprising as a simple pair potential has no concept of structure, and thus cannot be expected to capture structural features such as anisotropy. However, including orientations explicitly would require calculation of inverse trigonometrical functions at every timestep which significantly increases the computational demand, so a central force potential is still desired.

An answer inspired by tight-binding theory[30] was first given by Daw and Baskes in 1983[45]. They showed that a simple *embedding function* can capture the structure surrounding an atom, by independently summing over each atomic site rather than in the symmetric manner of (4.1). An embedded atom interatomic potential, used exclusively here, is of the form

$$V = \sum_l a_l \sum_i \left(\sum_j \rho_l(|\mathbf{x_i} - \mathbf{x_j}|) \right)^{C_l}, \tag{4.2}$$

where in general $C = 1, 0.5$ and other higher (integral) powers. For $C = 1$ we obtain the pair potential (4.1), but crucially when $C \neq 1$ the contribution from each atom, in particular the curvature, are sensitive to the proximity and arrangement of its neighbours through $\sum_j \rho_l(|\mathbf{x_i} - \mathbf{x_j}|)$.

After an interatomic potential is created, an initial atomic configuration is specified which is then dynamically integrated with Newton's equations. Temperature is typically introduced through some statistical procedure based on the Langevin equation or the Maxwell-Boltzmann distribution, but to extract intrinsic thermal results it is physically more appealing to rely on the molecular chaos of a large system rather than the often highly artificial connection of the system to an external heat generator.

We do not perform any interatomic potential development in this thesis, instead using 'state of the art' potentials used widely across the atomistic modelling community. Our main aim is to use large scale atomistic simulations to understand the complex nature of thermal fluctuations in such systems, which due to the complex form of (4.2) and its derivatives (please see Appendix A.3) has so far resisted detailed quantitative study.

4.1. The Drift and Diffusion of Kinks

Dislocation motion is limited by two general processes, the formation and migration of kinks and pinning by impurities and other defects [46]. In this section we investigate the motion of kink-limited screw and edge dislocations in bcc Fe, where the kink formation energy is much larger than the thermal energy. To obtain dislocation motion on the time-scales accessible to molecular dynamics (MD) simulations some researchers have resorted to inducing kink formation by applying stresses some six orders of magnitude greater than those pertaining experimentally [47, 48]. But dislocation core structures and Peierls barriers are known to be highly stress-dependent[49], making it difficult to relate simulation to the vanishingly low stress conditions found in thermally activated evolution of dislocation microstructures.

The periodic potential in the slip plane of a crystal leads to stable positions for a straight dislocation line separated by maxima in the potential energy known as Peierls barriers. When the Peierls barrier is large compared to the available thermal energy, the mobility of dislocations is limited by the discreteness of the crystal structure. In that case dislocation glide takes place by the thermally activated nucleation and propagation of kinks[5], which are localized regions connecting dislocation segments lying in adjacent valleys of the potential in the slip plane. The existence of kinks is clearly exhibited in MD simulations reported here and in many other investigations[48, 6, 50], and their movement effects the glide of the dislocations on which they lie. To understand the kink mechanism it is necessary to investigate both kink propagation and nucleation of pairs of kinks.

When the formation energy of kink pairs is large compared to the thermal energy it becomes impossible to obtain statistically significant data on kink nucleation within MD time scales without resorting to unrealistic applied stresses, typically six orders of magnitude larger than those encountered in experiments[47]. As a result, while the kink mechanism is well established in dislocation theory there is a sparsity of MD data on the parameters controlling kink motion, without which it is impossible to predict the velocity-stress relationship of the host dislocation for realistic stresses.

To circumvent the problem of kink nucleation in MD we use boundary conditions on the simulation supercell which enforce the existence of an isolated kink on the dislocation line. We use the MD code LAMMPS[51] with a recently developed potential by Gordon *et al.*[52] which gives the best available representation of the screw dislocation core structure and bulk phonon dispersion. To avoid free surfaces, periodic boundary conditions must be imposed. The dislocation supercell must contain defects with no net Burgers vector to avoid a divergent elastic energy, and in this work we use dislocation dipoles. Thus the supercell contains two dislocations with equal and opposite Burgers vectors, and each dislocation has one kink in the supercell.

Dislocation dipoles were introduced by removing an appropriate number of atoms for an edge dislocation dipole or shearing the simulation supercell for a screw dislocation dipole[53], and then applying the anisotropic elastic displacement field for the dipole. The system was relaxed by a conjugate gradients algorithm, followed by an annealing process which heated the system to 200K then back to zero temperature over 100ps (100,000 timesteps) to ensure that the system was in the ground state. To heat the system, atomic velocities were gradually rescaled according to a Maxwell-Boltzmann distribution of increasing temperature. Once the desired temperature was achieved the system was evolved microcanonically and data was taken. This has a firmer statistical basis than using a thermostat because it relies on the real atomistic heat bath of a large system rather than any particular thermostat algorithm. However, unrealistic results can be obtained if there is significant heat generation or absorption as this may affect the probability of other activated processes[47]. This is likely to be the case, for example, when a high energy kink pair annihilates or is created during the simulation. However, due to their large activation energies such processes did not occur during the simulations with the zero stress conditions investigated here, and the system temperature was observed to be constant throughout the simulation runs.

4.1.1. The Kink Vector

A kink connects two straight dislocation segments both parallel to a lattice vector $\mathbf{t}$ lying in the same slip plane. For the segments to be crystallographically equivalent they must be separated by a lattice vector, which may be uniquely identified, modulo $\mathbf{t}$, with a lattice vector $\mathbf{k}$ which we call the 'kink vector'. Some dislocations may exist with a variety of core structures and there is a corresponding variety of atomic structures of kinks [54, 55]. Nevertheless, the kink vector uniquely identifies any kink on a dislocation line in a given slip plane with a given Burgers vector and the same core structure on either side of the kink. We note in passing that a similar classification may also be applied to jogs, the sessile equivalent of a kink[5], where the 'jog vector' will be a lattice vector with a component normal to the slip plane. While the term kink vector has already appeared in the literature[55, 56] there has been no attempt to relate it to the host crystal lattice. To see the utility of our definition, consider a relaxed straight dislocation dipole, parallel to a lattice vector $\mathbf{t}$, in a supercell formed from lattice vectors $N_x\mathbf{m}$, $N_y\mathbf{t}$ and $N_z\mathbf{n}$, where the $N_{i=x,y,z}$ are all integers. To impose the boundary conditions required for a kink on each dislocation we create a new supercell from $N_x\mathbf{m}$, $N_y\mathbf{t}+\mathbf{k}$ and $N_z\mathbf{n}$, as shown in Figure 4.1. In principle $\mathbf{k}$ may be any lattice vector modulo $\mathbf{t}$ lying in the slip plane, but for high index lattice vectors the relaxed structure will possess multiple kinks as one might expect if $\mathbf{k}$ spans many minima of the potential in the slip plane. The set of low index lattice vectors lying in the slip plane quickly provides an enumeration of the possible kinks a straight dislocation line may support, generalizing the approach taken in previous work[56] to produce isolated kinks on dislocation lines. We have used this procedure to generate the simulation supercell geometries employed here. Each supercell contained approximately 700,000 atoms, with the dislocation line either initially sharply kinked as in Figure 4.1 or parallel to the $N_y\mathbf{t}+\mathbf{k}$ supercell vector. The relaxed configurations were independent of this initial preparation.

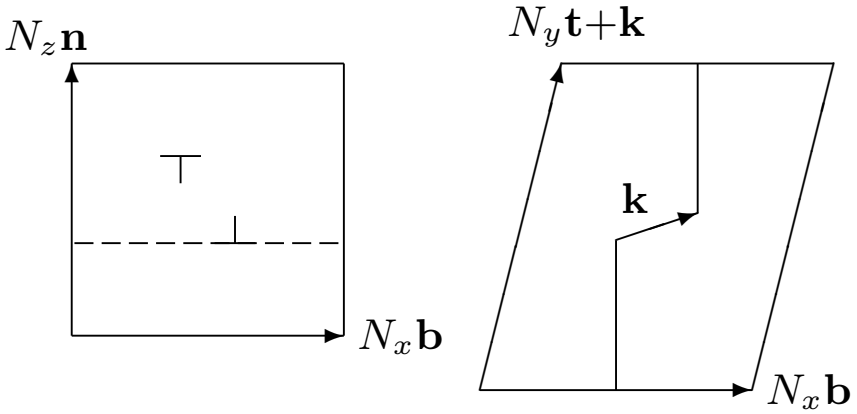

Figure 4.1.: Cartoon plan of the simulation supercell for an edge dislocation dipole, formed from lattice vectors $N_x\mathbf{b}$, $N_y\mathbf{t}+\mathbf{k}$ and $N_z\mathbf{n}$. The broken line in the left figure highlights one of the two slip planes, which are separated by half the supercell height $\frac{1}{2}N_z|\mathbf{n}|$.

4.1.2. A Coarse Graining Procedure for Atomistic Simulation

Having obtained a relaxed configuration, the atoms were grouped into atomic planes normal to the unkinked dislocation line direction $\mathbf{t}$. The potential energy in each plane has clearly defined peaks, the centres of gravity of which identify the positions of the dislocation core, as illustrated in Figure 4.2. The coarse grained representation of the dislocation comprises a line threading nodes at each of these core positions. There is one node for each atomic plane normal to the dislocation line. The coarse grained representation is well defined, independent of dislocation character, and it yields the position of the dislocation with atomic resolution. The unique mapping between the atomistic and coarse grained representations enables the energy of the coarse grained representation to be determined at each time step of the simulation. The position of each node on the dislocation line moves in one dimension, normal to $\mathbf{t}$ and the slip plane normal $\mathbf{n}$. The kink position and width were determined from the center and width of the maximum in the core energy along the dislocation line, with the trajectories of the two kinks in each supercell each forming a time series $\{x_{n\Delta t}\}$,$n = 0, 1, ...N$. The kink position is readily located graphically as shown in Figure 4.3, where the dislocation segments on either side of the kink are straight lines at ab-

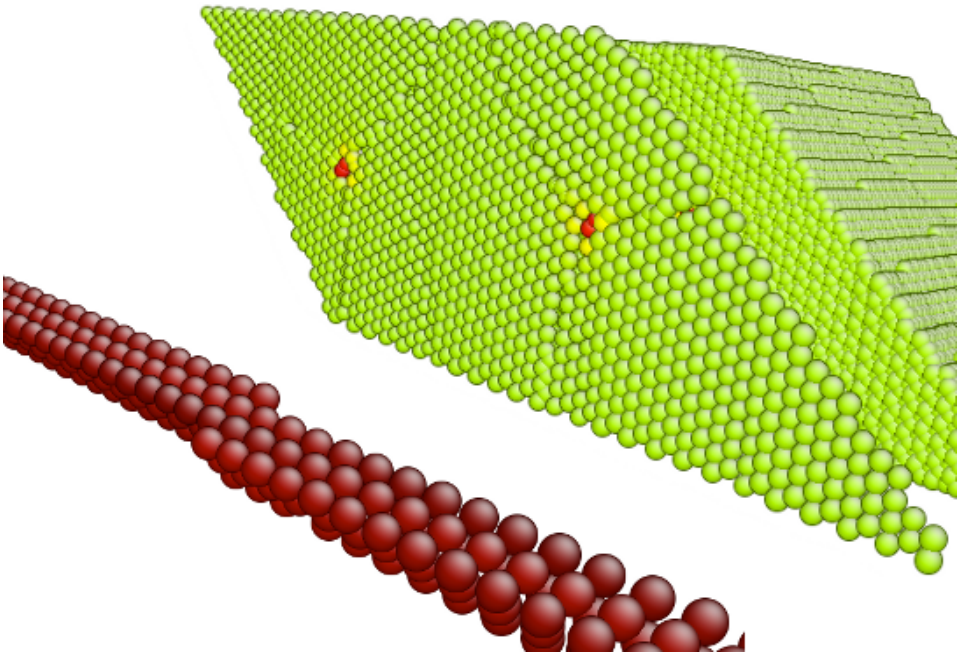

Figure 4.2.: Above: An atomic plane normal to a screw dislocation dipole is exposed with the higher energy atoms coloured progressively red. The dislocation cores are clearly identified. Below: Plotting only the highest energy atoms in successive atomic planes (red) along the supercell reveals a kinked dislocation line.

solute zero. The dynamics of the kink positions are simulated with MD in the following section and we aim to reproduce the dynamics with a coarse grained, many body, stochastic model.

The effectiveness of the coarse graining relies on the uniformity of the potential energy of atoms in the bulk; however, at finite temperature it is expected and observed that random fluctuations in atomic positions and energies due to thermal vibrations obscure the dislocation position. To filter out this noise it is necessary to average atomic positions and energies over a period of a few thermal oscillations. The atomic coordinates and energies can then be processed in an identical fashion to the relaxed zero temperature system, again yielding localized dislocation core positions. Kinks appear as localized geometric and energetic regions along the coarse grained dislocation line, allowing the determination of the kink position, width and formation energy by calculating the total deviation from the core energy of a straight dislocation line.

Other techniques to determine the dislocation position are to calculate the deviation of the atomic displacements from the anisotropic elastic field[56], or the bonding disregistry across the slip plane[57]. However, we found that the procedure employed here gave better localization at finite temperature and is applicable to many different dislocation geometries.

4.1.3. Diffusion simulations

Table 4.1 shows kink formation energies calculated for edge dislocations in bcc Fe. These values were obtained by calculating the excess energy in a cylindrical slice coaxial with the average dislocation line direction, relative to the energy of a slice containing the same number of atoms for a straight dislocation. The slices contain one atomic plane normal to the dislocation lines. The radius of the cylinder was enlarged, using the periodic boundary conditions if necessary to generate atomic coordinates outside the supercell, until the excess energy of the dislocation core in the slice reached a constant asymptotic value. This excess core energy is plotted in green in Figure 4.3. The kink formation energy is the sum of these excess core energies along

the dislocation line. Convergence in the core energy per atomic plane was typically achieved for a supercell length of thirty Burgers vectors for kinks on edge dislocations. This implies that the interaction energy between a kink and its periodic images along the line is not detectable at separations of more than thirty Burgers vectors. The kink formation energies are in broad agreement with other studies[58, 48, 59].

Burgers vector (**b**)	Glide plane	Tangent vector (**t**)	Kink vector (**k**)	Formation energy
$\frac{1}{2}[111]$	$(1\bar{2}1)$	$[10\bar{1}]$	$\frac{1}{2}[111]$	0.15 eV
	$(\bar{1}01)$	$[1\bar{2}1]$	$\frac{1}{2}[1\bar{1}1]$	0.03 eV
			$\frac{1}{2}[1\bar{3}1]$	0.02 eV
$[100]$	(001)	$[010]$	$[100]$	0.61 eV
	(011)	$[01\bar{1}]$	$\frac{1}{2}[11\bar{1}]$	0.25 eV

Table 4.1.: Kink vectors and fully relaxed kink formation energies (to 2 s.f.) on edge dislocations at absolute zero, calculated using the potential developed by Gordon *et al.*[52] for bcc Fe. The tangent vector **t** is the primitive lattice vector along the unkinked dislocation line.

As $[100](011)$ edge dislocations have not been directly observed in experiment they are of little interest and we do not consider them further here.

The very low formation energy of 0.03 eV for kinks on $(1/2)\langle 111\rangle\{1\bar{1}0\}$ edge dislocations indicates that the mobility of these dislocations is not limited by kinks except possibly at the very lowest temperatures. Therefore we investigate isolated kinks on $(1/2)[111](1\bar{2}1)$ and $[100](010)$ edge dislocations, whose motion is known to be kink-limited, at temperatures up to which kinks remain isolated on MD time-scales.

The kink formation energy for $\frac{1}{2}[111](1\bar{2}1)$ dislocations is 0.15eV. At temperatures below 300K it is possible to observe and analyse the stochastic motion of an isolated kink for MD runs of several nanoseconds. Similarly, for $[100](010)$ edge dislocations no additional kinks are expected to be nucleated in MD runs of several nanoseconds at temperatures up to 700K owing to their large formation energy of 0.61eV. This large formation energy is due to the non-planar core, shown in Figure 4.4. An isolated kink is localized

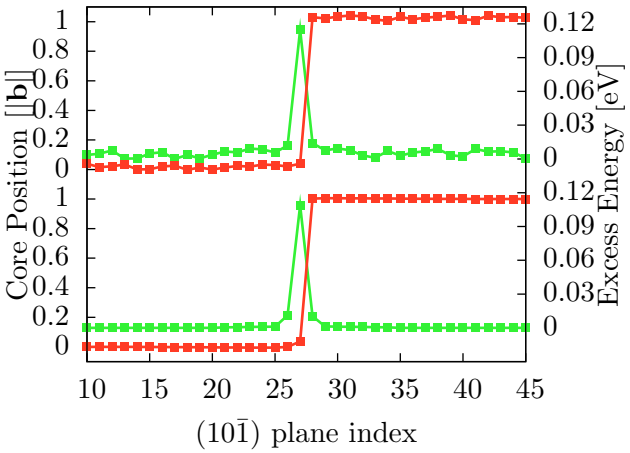

Figure 4.3.: Illustration of the coarse grained data from atomistic simulation of a kink on a $(1/2)[111](1\bar{2}1)$ edge dislocation line at 0K (bottom) and 90K (top). The kink is clearly localized as measured by the position of the core (red) and the core energy (green). Note the narrow kink width in contrast to the screw dislocation kinks in Figure 4.9.

geometrically and energetically as shown in Figure 4.3.

Figure 4.5 shows the trajectories of the two kinks in a simulation supercell on a $(1/2)\langle 111\rangle(1\bar{1}0)$ edge dislocation dipole. The two kinks appear to be moving independently, but we cannot be sure that there is no significant interaction between them. Any correlation arising from their interaction may be eliminated by analysing the center of mass $\bar{x}$, defined here to be the mean of the two kink positions, $\bar{x} = (x^{(1)} + x^{(2)})/2$. It may be shown[60, 14] that such a quantity is independent of any interaction, and it yields a diffusion constant one half that of a free kink, $D_{kink}/2$. Thus we construct from the two kink positions a single time series $\{\bar{x}_{n\Delta t}\}, n = 0, 1, ...N$ for the center of mass to ensure such correlation effects do not affect our results. We look for diffusive behaviour in the mean squared displacement (MSD)

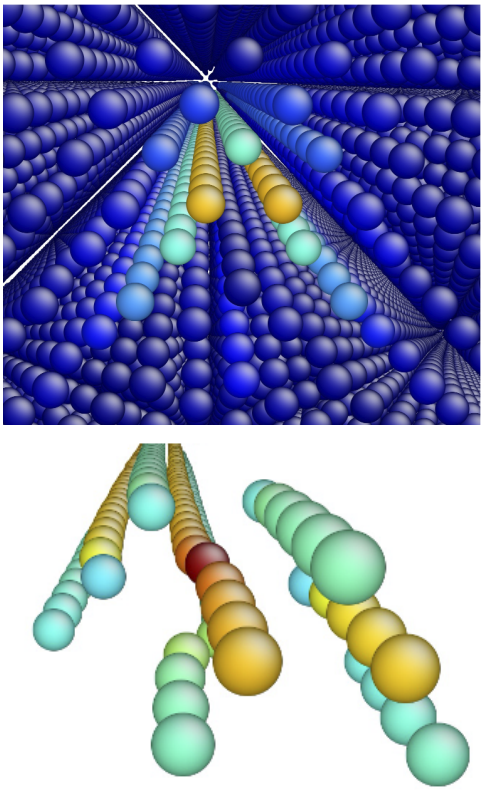

Figure 4.4.: Above: a [100](010) edge dislocation in the bulk. Below: a kink on this dislocation with the bulk atoms removed. The non-planar core gives a large kink formation energy of 0.61eV.

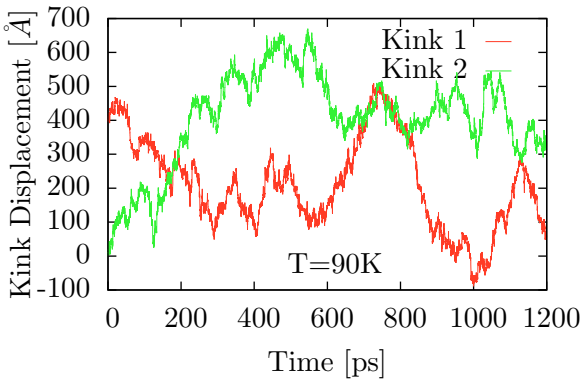

Figure 4.5.: The trajectories of the two kinks on a $\frac{1}{2}[111](1\bar{2}1)$ edge dislocation dipole at T=90K.

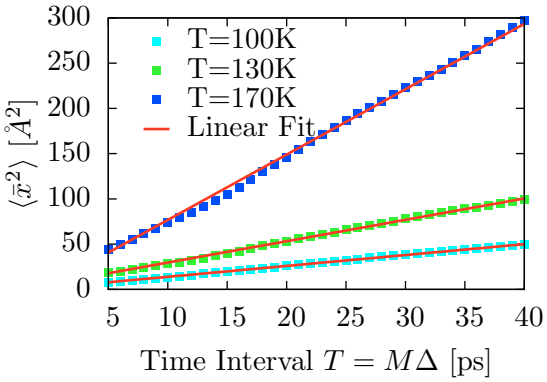

Figure 4.6.: The mean square displacement as defined in equation (4.4) for the kink center of mass on a $(1/2)[111](1\bar{2}1)$ edge dislocation dipole. The linear relationship with time is in agreement with diffusive behaviour, equation (4.4).

$\langle \Delta \bar{x}^2 \rangle$ over a range of intervals τ, defined as

$$\langle \Delta \bar{x}^2 \rangle(\tau) = \sum_{n=0}^{N-\tau/\Delta t} \frac{(\bar{x}_{n\Delta t+\tau} - \bar{x}_{n\Delta t})^2}{N - \tau/\Delta t} - \left(\sum_{n=0}^{N-\tau/\Delta t} \frac{(\bar{x}_{n\Delta t+\tau} - x_{n\Delta t})}{N - \tau/\Delta t} \right)^2, \tag{4.3}$$

which is the variance of the displacement. It is well known[14] that for diffusive motion with a diffusion constant $D_{kink}/2$,

$$\langle \Delta \bar{x}^2 \rangle(\tau) = D_{kink}\tau. \tag{4.4}$$

Examples of the MSD are shown for the system of kinks on edge dislocations considered above in Figure 4.6. The MSD clearly shows the linear time dependence characteristic of diffusive behaviour, with the diffusion constant as defined in equation (4.4) shown in Figure 4.7 for kinks on $\frac{1}{2}[111](1\bar{2}1)$ edge dislocations. Kinks on $a[100](010)$ edge dislocations exhibit similar behaviour. The diffusivity rises exponentially with temperature in both cases, indicating that the kink motion is thermally activated across the kink migration barrier[5]. We therefore conclude that the kink performs one dimen-

sional stochastic motion in a periodic migration potential $V(x+a)=V(x)$ whose amplitude $E_{mig}=V_{MAX}-V_{MIN}$ is large compared to the thermal energy. While the traditional analysis for such data is to fit an Arrhenius form $D_0 \exp(-E_{mig}/k_BT)$ for the diffusion constant, in one dimension there exists an exact solution, given by the Lifson-Jackson formula[61]

$$D_{kink} = \frac{k_BTa^2}{\gamma_{kink}} \left(\int_0^a e^{-V(x)/k_BT} dx \int_0^a e^{V(x)/k_BT} dx \right)^{-1}, \tag{4.5}$$

where k_B is Boltzmann's constant and γ_{kink} is the friction, or dissipation, parameter[15], which measures the rate of momentum transfer from the diffusing object (here a kink) to the heat bath. γ_{kink} plays a key rôle in the stochastic equations of motion introduced in 5.2, defining the frictional force $-\gamma_{kink}v$ and it is the inverse of the kink mobility. To gain insight into equation (4.5) we investigate limiting cases. When the amplitude of the migration potential $E_{mig}=V_{MAX}-V_{MIN}$ is much greater than thermal energy k_BT, as for the case of kinks on edge dislocations here, we may evaluate the integrals in (4.5) by the method of steepest descents. Denoting V'' for the second derivative, (4.5) becomes

$$D_{kink} \simeq a^2 \frac{\sqrt{V''_{MIN}V''_{MAX}}}{2\pi\gamma_{kink}} e^{-(V_{MAX}-V_{MIN})/k_BT}, \tag{4.6}$$

which is precisely the Arrhenius form given by Kramers[62] for thermally activated diffusive motion. We note that the traditional temperature independence of the prefactor in (4.6) requires that γ_{kink} be independent of temperature. In the other limit, when the thermal energy k_BT is much larger than E_{mig}, the integrals (4.5) are constant, giving a diffusivity

$$D_{kink} \simeq \frac{k_BT}{\gamma_{kink}} \tag{4.7}$$

as first described by Einstein[63] for a freely diffusing particle. We note that a linear temperature dependence in the diffusivity (4.7) implies γ_{kink} is again independent of temperature. We will see that kinks on screw dislocations exhibit the diffusive behaviour of (4.7) due to their negligible migration barrier and thus the relation (4.5) is able to capture the wide range of diffusive behaviour exhibited by kinks on dislocation lines. A numerical illustration of (4.5) is shown in Figure 4.8, where we indeed see the failure

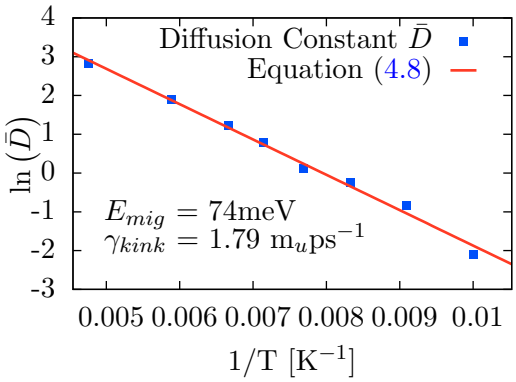

Figure 4.7.: Arrhenius plot of the diffusion constant $\bar{D}$ for the kink center of mass on a $(1/2)[111](1\bar{2}1)$ edge dislocation dipole. A two-parameter fit of equation (4.8) gives a migration barrier of 74meV, comparable the 150meV kink formation energy. The linear gradient implies the dissipation parameter γ_{kink} is independent of temperature (see text).

of the Arrhenius law when $k_B T \gg E_{mig}$. In section 5.2 we show that to an excellent approximation the migration barrier for a kink is sinusoidal, $V(x) = E_{mig} \sin^2(\pi x/a)$, allowing an exact expression of (4.5)

$$D_{kink} = \frac{k_B T}{\gamma_{kink}} \frac{1}{I_0^2(E_{mig}/2k_B T)}, \tag{4.8}$$

where $I_0(x)$ is the zeroth order modified Bessel function[64]. We thus perform a two parameter fit of (4.8) to the kink diffusion constant with temperature to determine γ_{kink} and E_{mig} for the kink systems investigated here, the results of which are shown in Table 5.1.

There are two points of note in the MD results for kinks on edge dislocations in Table 5.1. Firstly, we find that the migration barrier is comparable to the formation energy, implying that the nature of the kink mechanism on edge dislocations is complex, with double kink nucleation and kink migration occurring on similar timescales. This agrees with previous simulations on edge dislocations[48] where the mobility was found to be independent of the dislocation segment length. Secondly, the linear gradient of the Arrhenius plot in Figure 4.7 also implies, by equation (4.6), that the dissipation parameter for the kink γ_{kink} is temperature independent.

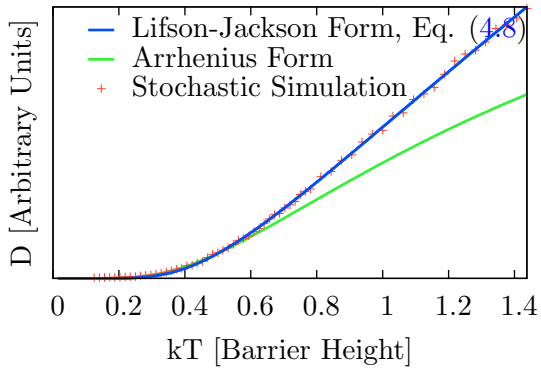

Figure 4.8.: Diffusivity in a one dimensional periodic potential. Equation (4.8) (blue), the appropriate Arrhenius form (green) and numerical data (red) are compared across a wide temperature range. At low temperatures all three agree but at intermediate to high temperatures a linear temperature dependence emerges in simulation and equation (4.8).

We show in 5.2 that the dissipation parameter for a kink is proportional to the dissipation parameter for the host dislocation line, which should therefore also be temperature independent. Although this agrees with several [65, 47, 66, 67], though not all[68, 69], atomistic simulations of dislocations and other defect systems in bcc Iron, decades of theoretical work[70, 32, 5] conclude that the dissipation parameter for a dislocation should increase linearly with temperature due to the increasing phonon population. We return to this important issue concerning the coupling of dislocations to the heat bath in the following section on screw dislocations, as the diffusive form (4.7) they exhibit allows an even more direct investigation of γ_{kink}.

While edge dislocations may be thought of as an inserted half plane of atoms[5] producing a bonding disregistry perpendicular to the dislocation line direction, screw dislocations create a bonding disregistry along the dislocation line direction, which does not require the addition or removal of material. Screw dislocations possess a non planar core structure in bcc metals, which gives a large Peierls barrier[29, 71]. The complex core structure is heavily influenced by the choice of interatomic potential used in classical atomistic simulations. The vast majority of existing potentials predict a screw dislocation has multiple core structures[72, 73], leading many authors to suggest that a screw dislocation may pass through a metastable core

structure during the kink nucleation process[71]. Under an applied stress this can produce a new kink formation pathway leading to a discontinuity in the flow stress[46, 52, 66]. However, this discontinuity is not shown in experiment, and recent *ab initio* calculations[74, 75] rule out any metastable core structure, with the nucleation pathway seen to occur almost entirely in the $\{1\bar{1}0\}$ slip planes. A recently developed potential by Gordon *et al.*[52] attempts to address these issues, concluding that while the metastable core may be removed from the nucleation pathway, multiple core structures remain. Using this potential, we introduce kinks with the core structure predicted from first principles calculations, thereby minimizing unphysical effects due to the interatomic potential.

A screw dislocation dipole requires a triclinic simulation cell to avoid spurious image stresses; we refer the reader elsewhere for details of the simulation method[76, 6, 77] which are well established. As before, the kink vector was added to the supercell vectors to give the boundary conditions required for isolated kinks to form on each dislocation under relaxation.

Previous zero temperature calculations of isolated kinks on screw dislocations in bcc Iron[56] with the Mendelev *et al.* potential[73] found a noticeable difference between the formation energies of 'right' and 'left' kinks, which correspond to kink vectors $\mathbf{k}_R=(1/2)[1\bar{1}1]$ and $\mathbf{k}_L=[010]$. They also found the kink formation energy converged to a constant value when the supercell length was greater than the widths of two kinks. The supercell length measures the separation between a kink and its periodic images. These findings are inconsistent with elasticity theory of kink interactions[78], according to which the far field interaction between kinks should decrease with the inverse of the kink separation.

To investigate these discrepancies we performed similar calculations with the improved potential by Gordon *et al.*, extending the supercell length to 240 Burgers vectors, more than double that used in [56]. In agreement with elasticity theory we found that when the supercell length was greater than two kink widths the kink formation energy decreased with the inverse of the supercell length, by 0.011eV for both right and left kinks over a distance of 200 Burgers vectors. The formation energy for the right and left kinks was

0.604eV and 0.13eV respectively, giving a double kink formation energy of 0.734eV, in good agreement with [56].

We conclude that the long range kink interaction, while decaying inversely with separation as predicted by elasticity theory[78], is a small perturbation to the kink formation energy in the atomistic simulations performed here and in [56]. However, the difference in formation energies of left and right kinks is still unexplained. To gain insight into the kink structure, Figure 4.9 shows the excess potential energy, relative to a straight dislocation, per atomic plane normal to the line of a screw dislocation with a right or left kink, obtained by the coarse graining procedure described above. The kinks appear as well defined peaks of approximately the same height but also with long range tails which differ markedly between the two kinks. These long range tails are the source of the difference in the formation energies, with the 'core' of each kink very similar in size and energy.

The nature of these tails may be understood by noting that the kinks may be regarded formally as two short segments of dislocation with edge character. The edge segments are of equal and opposite sign because their line senses are reversed, which implies their fields cancel at long range. To test this we average the energy per unit length for the left and right kinked screw dislocation lines, shown in Figure 4.9, where we indeed see a localized peak with a width of around $20|\mathbf{b}|$, much wider than the sharp kinks of width $3|\mathbf{b}|$ seen on edge dislocations. It is this core energy and width which we take to define kinks on screw dislocations.

At finite temperature, the kink trajectories were analysed in a similar manner to that detailed above for edge dislocations. However, the temperature dependence of the kink diffusivities, shown in Figure 4.10, is markedly different. They exhibit a linear temperature dependence, which by equations (4.5), (4.7) implies a negligible migration barrier, as found in static calculations[56]. It also implies that the dissipation parameter γ_{kink} is independent of temperature.

The temperature independence is significant as all theories of dislocation damping since Liebfried[70, 32] have concluded that the dissipation

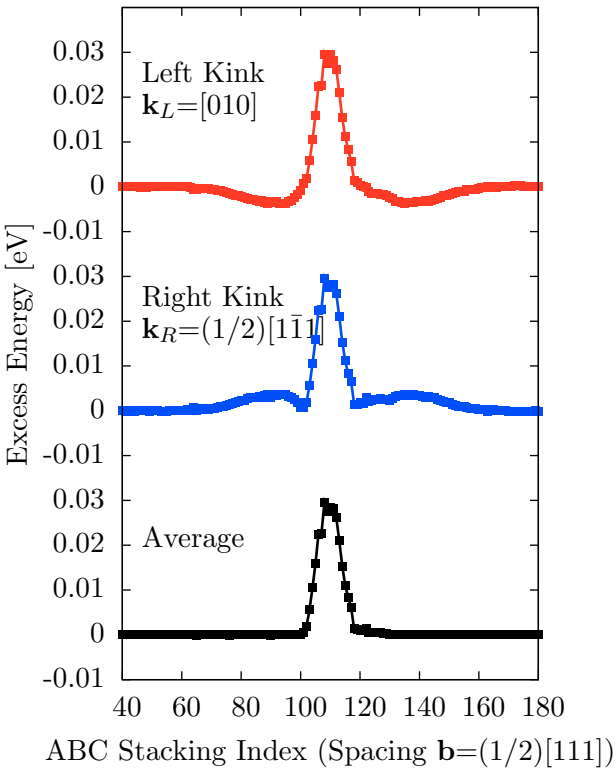

Figure 4.9.: Excess energy per ABC stacking sequence (see text) for right (blue) and left (red) kinks on a (1/2)[111](1$\bar{1}$0) screw dislocation. The kinks appear as peaks of similar height with asymmetric tails. The tails are removed under averaging (black) as described in the text. Note the large kink width as compared to the edge dislocation kinks in Figure 4.3.

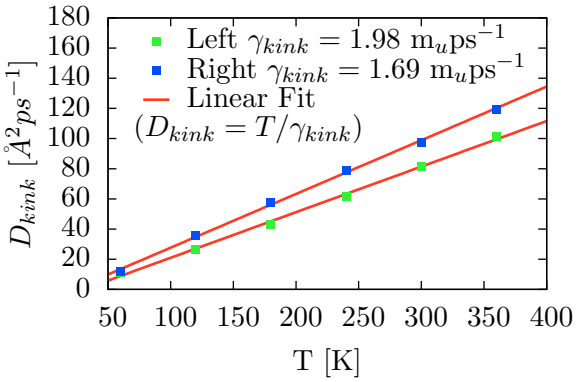

Figure 4.10.: Diffusion constant for left and right kinks. A linear temperature dependence is exhibited, which implies the dissipation parameter does not depend on temperature.

parameter for a dislocation must increase linearly with temperature due to the increased phonon population. We emphasize that the temperature independence of the dissipation parameter is exhibited in both thermally activated diffusion, i.e. the prefactor of the Arrhenius law is independent of temperature, and in essentially free diffusion, i.e. the gradient of the diffusion constant with temperature is independent of temperature. This discrepancy between theory and simulation has remained unexplained but will be addressed in the final chapter.

4.1.4. Drift Simulations

Whilst we have seen that kinks diffuse in equilibrium, they will also drift under an applied stress[5]. To accurately test our parametrization of the kink mobility we must therefore determine the kink velocity under applied stress. To apply a shear stress of σ to a screw dislocation we apply a force of $A\sigma$ to each atom in two bounding $(1\bar{1}0)$ planes, where A is the area per atom, as illustrated in Figure 4.11. As opposed to the kink diffusion simulations, we now only have periodicity normal to these bounding planes. For these simulations we studied kinks in bcc Tungsten, using a recently developed potential by Marinica *et al.*[43] which gives the best available representation of the screw dislocation core structure and bulk phonon dispersion. The simulation output was time averaged and energy filtered in both zero and finite stress conditions to produce a series of kink positions from which a kink drift and diffusivity were statistically determined.

The results of these simulations are displayed in Figure 4.12. Kinks were observed to freely diffuse with a diffusivity $D = \mathrm{k_B T}/\gamma_{\mathrm{kink}}$ under no applied stress with fully periodic boundary conditions, whilst under stresses of $2 - 10$MPa applied to the bounding $(10\bar{1})$ planes kinks were observed to drift with a viscous drag law $\dot{X} = |\boldsymbol{\sigma} \cdot \mathbf{b}|/\gamma_{\mathrm{kink}}$. Although the two screw dislocations would eventually annihilate under the applied stress, for a sufficiently wide and long supercell the kinks drift independently for at least two supercell lengths ($\sim$600Å) before any influence of their mutual attraction could be detected.

The drift and diffusion simulations showed excellent agreement with the Einstein relation $D = \mathrm{k_B T} \lim_{|\boldsymbol{\sigma}\cdot\mathbf{b}|\to 0}(\dot{X}/|\boldsymbol{\sigma}\cdot\mathbf{b}|)$, with the viscous drag γ_{kink} *independent* of temperature and showing little variation between left and right kinks. The final mobility laws were determined to be v =0.037Å/ps/MPa for $\mathbf{k} = 1/2[1\bar{1}1]$ ('right' or 'interstitial') kinks and v =0.040Å/ps/MPa for $\mathbf{k} = [010]$ ('left' or 'vacancy') kinks.

We again see a violation of phonon scattering treatments[5] which predict that γ_{kink} should increase linearly with temperature due to the increased phonon population, meaning the observed temperature *independence* of γ_{kink} agrees with the kink diffusion and other dislocation and defect

simulations addressed below.

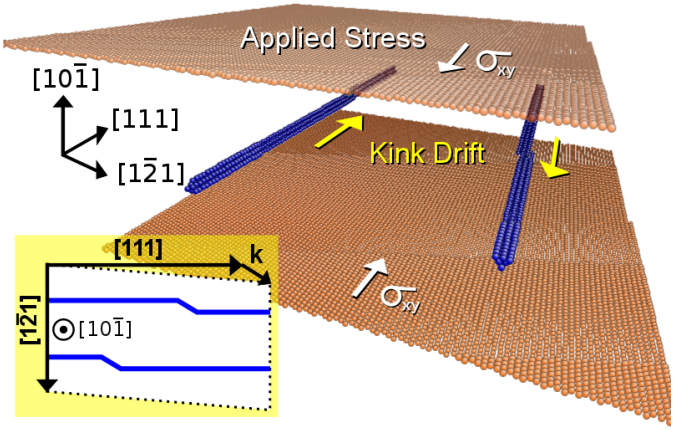

Figure 4.11.: Illustration of kink drift simulations. Kinks on a $1/2\langle 111\rangle\{10\bar{1}\}$ screw dislocation dipole, characterized by a lattice 'kink' vector **k**, are subject to an applied stress on bounding $(10\bar{1})$ planes. Under no applied stress with fully periodic boundary conditions the kinks diffuse freely. Inset: Cartoon of the supercell along $[10\bar{1}]$, illustrating the relation of the kink vector to a kinked dislocation line.

In this section we have reported the results from large scale molecular dynamics simulations of isolated kinks on edge and screw dislocation lines in bcc iron. The large simulation cells required significant computational power to obtain statistically significant results; however the total real time simulated was still of the order of nanoseconds. In subsequent chapters we will introduce a model which aims to reproduce the coarse grained data from the full atomistic simulation at a fraction of the computational cost, allowing access to experimentally relevant time and length scales.

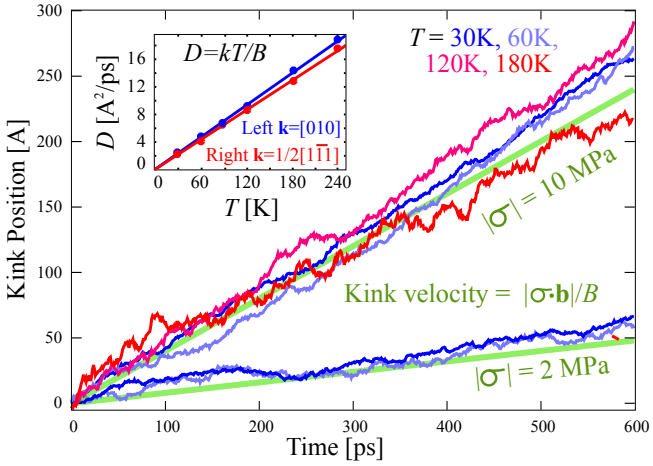

Figure 4.12.: Results of kink drift simulations for $\mathbf{k} = 1/2[1\bar{1}1]$ (right) kinks on $1/2\langle 111\rangle\{10\bar{1}\}$ screw dislocations. We see a temperature independent[1] drift velocity $v = |\boldsymbol{\sigma} \cdot \mathbf{b}|/B$ in very good agreement with γ_{kink} determined from zero stress kink diffusion simulations (green lines). Inset: Results from kink diffusion simulations. We see the diffusivity $D = \text{k}_\text{B}\text{T}/\gamma_{\text{kink}}$ rises linearly with temperature, meaning that $\gamma_{\text{kink}} = \text{k}_\text{B}\text{T}/D$ is independent of temperature.

4.2. The Drift and Diffusion of Lines and Loops

Through procedures essentially identical to those employed to determine γ for kinks, it is also possible to determine γ for any mobile crystal defect which can exhibit stochastic motion on MD timescales. Although drift simulations can be performed for extended dislocation lines under the application of a homogeneous applied stress, any isolated crystal defects are either point defects or loops with no net line direction they only respond to a stress gradients[5]. This means drift simulations would need a highly heterogeneous applied stress which can confuse the analysis and is often very difficult to accommodate within the periodic boundary conditions required for dynamics without surface stresses. As a result zero stress diffusion simulations are employed, allowing the extraction of a diffusion constant by analysis of the timeseries of positions which may then be inverted to obtain γ through the Einstein relation $\gamma = \text{k}_\text{B}\text{T}/D$.

Due to their importance and predominance in radiation damage, previous

calculations (e.g. [67, 79, 65]) have focused on the diffusion of single and multi atom self interstitial atom (SIA) defects, illustrated in figure 4.13. Representative results are presented in figures 4.14,4.15; in all cases we see that the diffusivity rises linearly with temperature, implying that γ is temperature independent, i.e.

$$D = \frac{\mathrm{k_B T}}{\gamma} \propto \mathrm{k_B T} \quad \Rightarrow \quad \gamma = \gamma_0. \tag{4.9}$$

We have also extracted γ by drift and diffusion methods for extended $\mathbf{b} =$

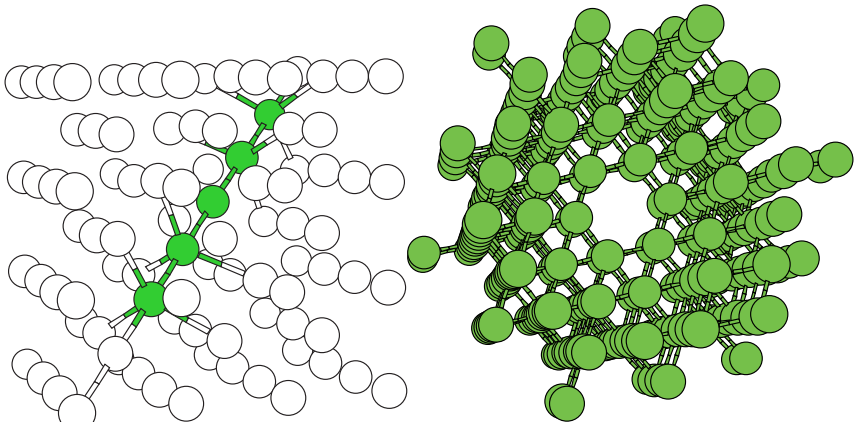

Figure 4.13.: Representations of a single atom self interstitial atom defect known as a crowdion, and a 37 atom SIA prismatic loop. From[65].

1/2[111] edge dislocation lines in bcc iron and tungsten, which are known to be highly mobile. As shown in figure 4.16 the drift diffusion law $\langle \dot{x} \rangle / \sigma \cdot b = D/\mathrm{k_B T}$ is obeyed, but we see a markedly different temperature dependence as compared to prismatic loops. We find that in general $\mathrm{k_B T}/D = \gamma$ has the mixed dependence

$$\gamma = \gamma_0 + \gamma_\mathrm{w} \mathrm{k_B T}, \tag{4.10}$$

in very good quantitative agreement with Gilbert *et al.*[47], though they did not comment on the temperature independent offset γ_0. Instead, in common with other authors[69, 80] they focussed on the temperature dependent term $\gamma_\mathrm{w} \mathrm{k_B T}$, as this is in closer agreement with traditional phonon scattering theories (see chapter 2). The origin of these different terms is a central point of this thesis and will be discussed extensively in later chapters. Importantly,

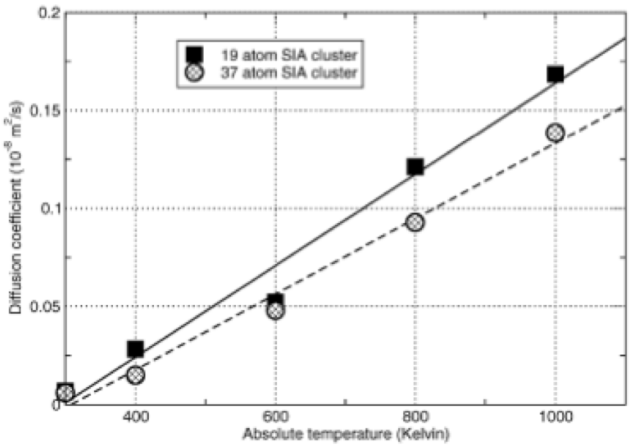

Figure 4.14.: $D = k_B T/\gamma$ for 19 and 37 atom SIA clusters in tungsten. The linear temperature dependence implies $\gamma = \gamma_0$ is independent of temperature. From[65].

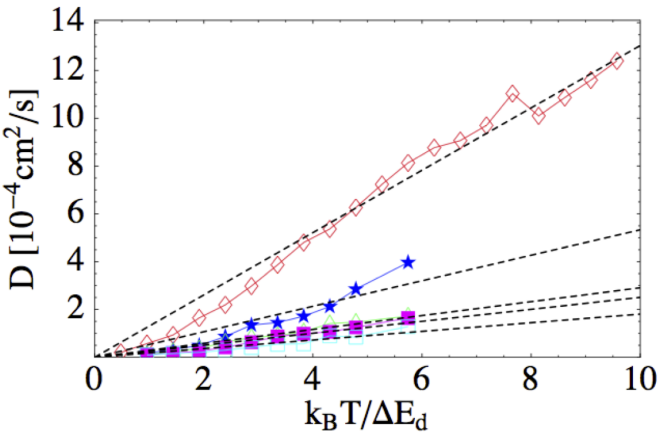

Figure 4.15.: $D = k_B T/\gamma$ for a single SIA (red), 7 (blue), 19 (green), 37 (pink) and 61 (light blue) atom SIA clusters in vanadium. Again, the linear temperature dependence implies $\gamma = \gamma_0$ is independent of temperature. From[79].

we found γ to be independent of line length, providing very strong evidence that the frictional coupling is independent of any long range correlations induced by vibrational modes of the line. To further investigate the source of the different temperature dependence between dislocation lines and loops, we also constructed a rather obtuse defect, a 'string' of $1/2\langle 111\rangle$ crowdions.

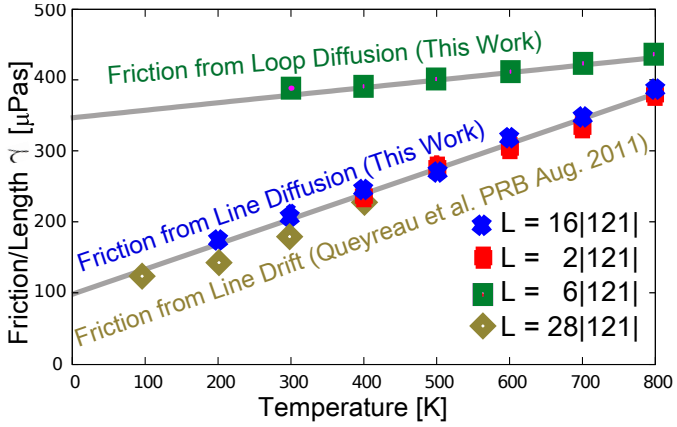

Figure 4.16.: γ extracted from the estimated diffusivity D through the Einstein relation $\gamma = \mathrm{k_B T}/D$ for a $\mathbf{b} = 1/2[111]$ edge dislocation line and prismatic loop. We see $\gamma = \gamma_0 + \gamma_\mathrm{w}\mathrm{k_B T}$, but γ_w dominates for the line whilst γ_0 dominates for the loop.

The intention was to determine the influence of a dislocation line's core in comparison to point defects or small loops. The asymmetry of an inserted half plane inherent to a line significantly deforms the lattice and gives the long range $1/r$ elastic field as compared to the $1/r^2$ field of a loop. In contrast, the crowdion string may look like a line (see figure 4.17) and possess the same configurational complexity, but there is no inserted half plane and no net line direction, meaning it will not move under a homogeneous stress and is perhaps best thought of as the limiting case of an infinitely eccentric loop. In this way we may unambiguously differentiate between core and configurational influences on the temperature dependence of γ. The results of these simulations are shown in figure 4.17. Interestingly, we see an almost perfect temperature independence in γ for the crowdion string, strongly implying that the significant core distortions that give rise to the long range elastic field are also responsible for the temperature dependent $\gamma_\mathrm{w}\mathrm{k_B T}$ component of γ.

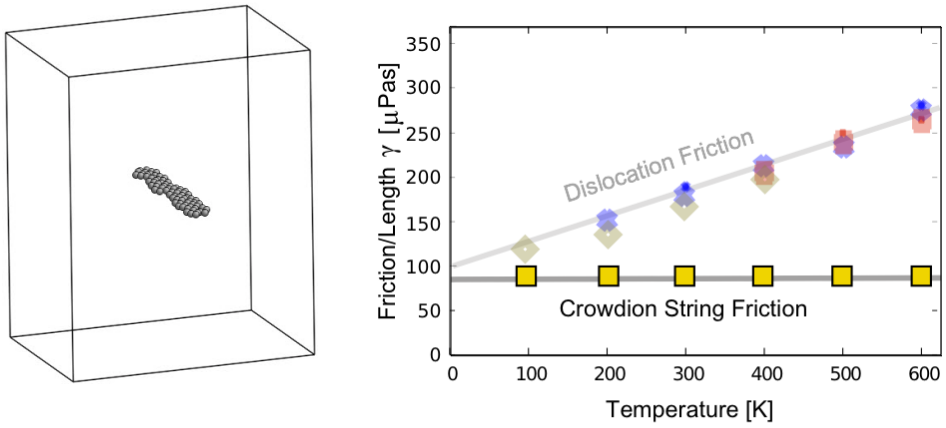

Figure 4.17.: Left: A 'string' of 1/2[111] crowdions, which has the configurational complexity of a line but is in fact a loop of infinitesimal width, deforming a lattice much less than a true dislocation line and without the long range elastic field. Right: Measurements of γ for the string in comparison with γ for a $\mathbf{b} = 1/2[111]$ edge dislocation line. We see the temperature dependent component $\gamma_w k_B T$ disappears for the string, implying that the significant deformation of a dislocation line gives rise to the long range elastic field and the 'phonon wind' term $\gamma_w k_B T$.

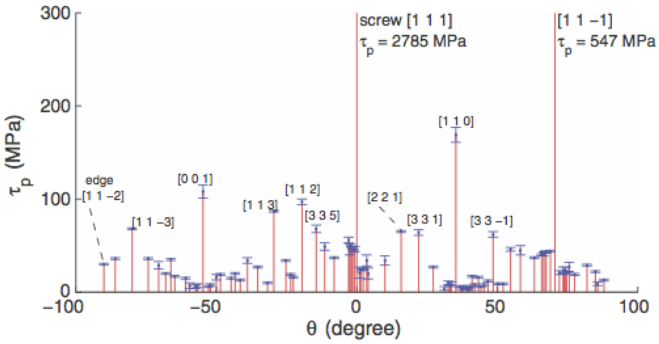

Figure 4.18.: Peierls stresses (the maximum gradient of the Peierls Barrier) for a wide range of $1/2\langle 111\rangle(1\bar{1}0)$ line orientations in bcc Ta, as reported in [83]. We see the screw ([111]) and M111 ([11$\bar{1}$]) dislocations have much higher barriers than all others. We have investigated these dislocations and found the reported high stresses for M111 arise from an erroneous migration pathway.

4.3. Formation and Migration of M111 dislocations

In the preceding analysis we have focussed on pure edge and screw dislocations. For the dominant $1/2\langle 111\rangle(1\bar{1}0)$ slip system we saw that edge dislocations lying along $\langle 1\bar{2}1\rangle$ are highly mobile and pure screw dislocations lying along $1/2\langle 111\rangle$ are highly immobile with large kink formation barriers. Naturally, there has been much investigation of the intermediate line directions. In early simulation studies[81, 82] it was found that a particular mixed dislocation, named M111, possessed a potentially large Peierls barrier and could be an important rate limiting process. Since this conclusion was also found in a very recent systematic study of Peierls barrier dependence on line orientation for the $1/2\langle 111\rangle(1\bar{1}0)$ slip system[83], as shown in figure 4.18, we have also investigated these dislocations. A M111 dislocation lies along $1/2\langle 1\bar{1}1\rangle$, at $\cos^{-1}(1/3) = 71°$ to the Burgers vector. The core structure of the M111 dislocation is best described in terms of the 'core units' introduced above. Figure 4.19 shows the energy per unit length for a pure edge and M111 dislocation along with illustrations of their structure. We see that the pure edge dislocation is formed of units of three atomic planes sheared by $90° - 71° = 29°$ which form a frustrated 'zig-zag' into a straight line, whilst the M111 dislocation can be thought as units of single atomic

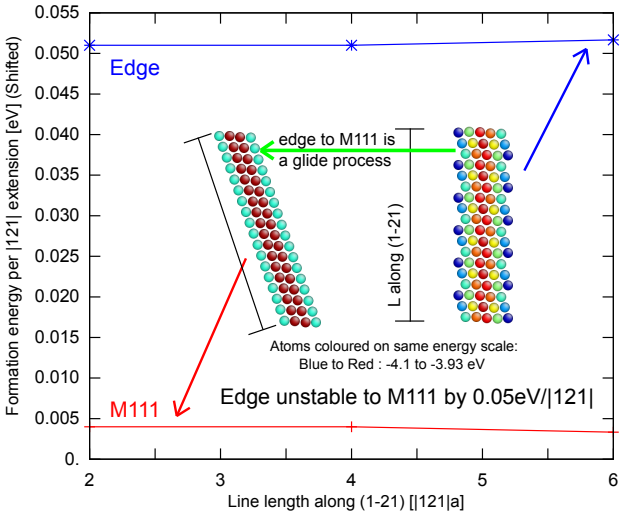

Figure 4.19.: Energy per unit length for M111 and $1/2\langle 111\rangle(10\bar{1})$ edge dislocations of various lengths. The two flat lines show convergence of the calculations, and we see that if unconstrained by the periodic boundary conditions conventionally applied, $1/2\langle 111\rangle(10\bar{1})$ edge dislocations are unstable to M111 formation. We propose that this is the origin for the anomalous habit plane of large $1/2\langle 111\rangle$ prismatic loops seen in MD and TEM experiments[60, 9].

planes sheared by 29°. The energetic calculations show that the M111 dislocation is additionally lower energy than the pure edge and the two are linked by a glide process. Crucially, this would never be seen in typical simulations as the conventional periodic boundary conditions frustrate an edge dislocation to be straight. This frustration provides a rationalisation for the erratic motion of such dislocation lines. We further note that this instability to M111 formation provides a compelling explanation for the observed anomalous habit plane for $1/2\langle 111\rangle$ prismatic dislocation loops[50]. We now turn to M111 migration. In previous studies[83] migration barrier calculations have always been performed using dislocation configurations where the initial and final configurations are separated by a rigid translation perpendicular to the line direction; barrier climbing algorithms[84] then find the minimum energy pathway between these two configurations. Given the ease of pure edge dislocation movement along [111] and the observed

similarity of M111 dislocations to pure edge dislocations, we investigated the migration barriers along [121] (perpendicular to $[1\bar{1}1]$), as previously used) and along [111].

As shown in Figure 4.20 we find a migration barrier comparable to that of a screw dislocation along [121] as found in the previous study[83], but a very low migration barrier along [111], showing that M111 dislocations move obliquely. To provide conclusive proof of this mechanism, we simulated pure edge and M111 dislocation dipoles under no applied stress in bcc Fe at 350K. A snapshot is provided in Figure 4.21. We found that M111 dislocations glide freely under no applied stress in [111] directions. As a result we conclude that M111 dislocations move obliquely along [111] directions, a phenomenon not accessible to a continuum model and one which we expect to affect the motion of pinned M111 dislocations as they have a large barrier to motion perpendicular to their line direction. We finally note that the use of dislocation 'core units' provides a natural means of describing the transition from pure edge to M111- an inherently discrete interpretation.

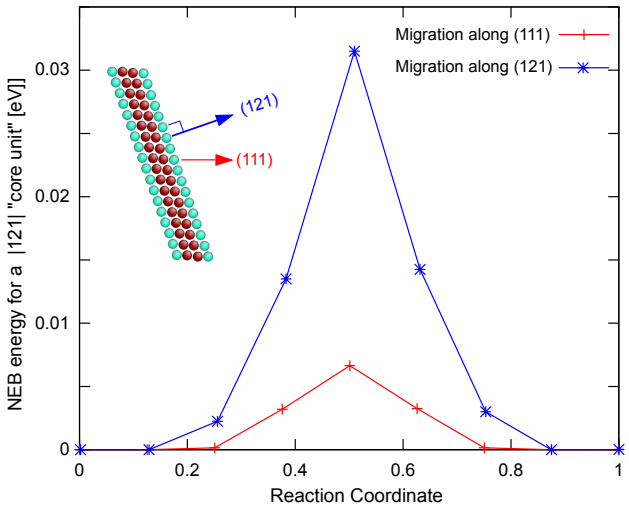

Figure 4.20.: NEB[84] calculations of Peierls barriers for various migration pathways of a M111 dislocation in bcc iron. We see the conventional (121) pathway perpendicular to the line direction gives a noticeably higher barrier than the (111) pathway proposed here. The (111) barrier is comparable to the highly glissile $1/2\langle 111\rangle(10\bar{1})$ edge dislocation and M111 dislocations are highly mobile at 300K. This is in contrast to previous work[83] which assumed M111 dislocations are immobile due to the large Peierls barrier along (121).

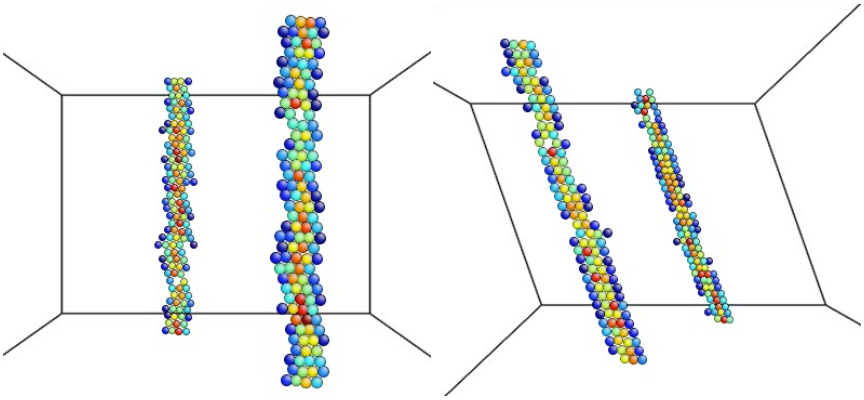

Figure 4.21.: Snapshots of $1/2\langle 111\rangle(10\bar{1})$ edge and M111 dislocation dipoles in bcc Fe at 350K. Under no applied stress both dislocation characters diffuse freely, providing conclusive evidence of the high mobility of M111 dislocations.

5. Properties of Coarse Grained Dislocations

There are two principal methods for simulating dislocation motion that avoid an explicit treatment of atomic dynamics: dislocation dynamics and kinetic Monte Carlo methods. In conventional dislocation dynamics codes the motion of dislocations is entirely deterministic [6]; the stochastic dislocation dynamics observed in MD simulations and experimentally cannot be simulated with such codes. The traditional technique to model thermally dominated motion is a master equation approach[11, 12, 13]. This assigns probabilities from the canonical ensemble to transitions between different system states, which are then implemented in a kinetic Monte Carlo simulation. However, the large state space available to even an isolated flexible dislocation quickly renders the technique extremely cumbersome. The assignment of a canonical distribution is hard or impossible to justify in non-equilibrium environments and while the logarithmic time scale employed improves efficiency it obscures comparison to the real-time trajectories given by experiment and atomistic simulation.

In this section we introduce a model which aims to reproduce the results from full atomistic simulation. The model we employ is the well known discrete Frenkel-Kontorova-Langevin (FKL) model[85, 86, 87] which treats the dislocation line as a discrete elastic string sitting in a periodic substrate potential. The representation of a dislocation as an elastic line was first used to model pinning by trapping sites[88] and due to its simplicity equivalent systems appear in many areas[46]. A discrete Langevin equation approach has recently been used to model the thermal motion of $(1/2)\langle 111\rangle$ prismatic and vacancy dislocation loops in bcc Fe by Derlet *et al.*[50]. However, the absence of a substrate potential rendered the model unable to capture any kink mechanisms and the discreteness had no relation to the crystallography

of the corresponding atomic system. In contrast, the spacing of nodes of the elastic string in our model is determined by the spacing of atomic planes normal to the dislocation line. We find this is essential to reproduce the structure and dynamics of kinks seen in atomistic simulations. While these discreteness effects have previously been investigated theoretically by Joós and Duesbery[87] in covalent materials there has been no investigation, to our knowledge, of the dynamical behaviour they predict.

First we obtain analytic expressions for the kink formation energy, width and migration barrier in terms of the parameters defining the FKL model. We then introduce the stochastic equations of motion which govern the system dynamics, obtaining an analytic expression identical in form to equation (4.5) for the kink diffusivity. By equating these analytic expressions to the values obtained for the kink formation energy, width, migration barrier and diffusivity from MD, we may solve numerically for the FKL model parameters.

Numerical integration of the stochastic equations of motion of the FKL model produces data which may be processed identically to that from atomistic simulation, allowing us to compare the statistical results obtained from both methods. We find the transport properties of kinks in the MD simulations and their FKL counterparts to be in excellent agreement over a wide range of temperature for different dislocations. In section 5.3 the parametrized FKL models are then used to investigate screw and edge dislocation mobilities at applied stresses too low to induce dislocation motion in MD.

We then move onto more general mathematical analysis of the FKL model in section 5.5, using modern homogenisation techniques to derive exact bounds on the center of mass mobility for a dislocation line or loop. We show that the free energy landscape always underestimates finite temperature migration barriers, and relate these findings to common models such as transition state theory.

5.1. The Frenkel-Kontorowa model

The FKL model treats a dislocation line as a discrete elastic string sitting in a periodic substrate potential. Many different shapes of the substrate potential used in the FKL model have been investigated[78]. However, the only qualitative change occurs in the presence of deep metastable minima, which imply the existence of a metastable core structure. As discussed above, even for the complex case of screw dislocations, recent *ab initio* calculations show the kink formation process to take place in the slip plane, with no metastable core structure. This allows us to take the substrate potential in the FKL model as a simple sinusoid, and is consistent with the approximation of taking a dislocation line to be a string of constant internal structure moving only in the slip plane.

The string itself is constructed from a set of harmonically coupled nodes spaced by a fixed distance a, which we set equal to the distance between atomic planes normal to the dislocation line. The string sits in a substrate potential of period L_P, which we set equal to the projection of the relevant kink vector normal to the dislocation line, often known as the kink height. As a result the two length scales of the model, a and L_P, are determined by the crystallography of the corresponding atomistic system.

Taking a co-ordinate system (x, y), where $\hat{\mathbf{x}}$ lies along the (unkinked) dislocation line direction and $\hat{\mathbf{y}}$ is normal to $\hat{\mathbf{x}}$ in the slip plane, each dislocation is represented by a discrete line of points $\{(na, u_n(t))\}$, where $n = 0, 1, 2, ..N$ and only the $\{u_n(t)\}$ vary with time. Each node is thus constrained to move only in the $\hat{\mathbf{y}}$ direction. The potential energy is as follows:

$$V\left(\{u_n\}\right) = \sum_{n=0}^{N} aV_P \sin^2\left(\pi \frac{u_n}{L_P}\right) + a\frac{\kappa}{2}\left(\frac{u_{n+1} - u_n}{a}\right)^2, \tag{5.1}$$

where V_P is the amplitude of the substrate potential and κ is the harmonic coupling strength, both in units of energy per unit length, with displaced periodic boundary conditions to account for the presence of the kink

$$u_{n+N}(t) = u_n(t) + L_P. \tag{5.2}$$

To obtain an analytic expression for the shape of the static kink we first take the continuum limit $a \to 0, N \to \infty$. In this limit, the system energy (5.1) with boundary conditions (5.2) is minimized by the soliton kink

$$u_{kink}(x - X) = \frac{L_P}{\pi}\left(\tan^{-1}\sinh\left(\frac{x - X}{w_0}\right) + \frac{\pi}{2}\right),$$

$$w_0 = \frac{L_P}{2\pi}\sqrt{\frac{2\kappa}{V_P}}, \tag{5.3}$$

where X is the kink position and $2w_0$ is the kink width, which is proportional to $\sqrt{\kappa/V_P}$. The solition kink (5.3) shape interpolates the numerically minimized discrete structure of (5.1) well. However, in the continuum limit the system energy (5.1) is independent of the kink position, while in the discrete system the energy varies periodically with the kink position as the continuous translation symmetry is broken, in direct analogy to the Peierls barrier for a dislocation. This position dependent energy produces the kink migration barrier discussed above. It may be shown[86, 87, 78] that substituting (5.3) into (5.1) gives

$$V\left(\{u_{kink}(na - X)\}\right) = \frac{w_0 V_P}{4} + \sum_{n=1}^{\infty} \tilde{V}_{mig}(n)\cos\left(\frac{2n\pi}{a}X\right),$$

$$\tilde{V}_{mig}(n) = \frac{V_P}{4a}\frac{n\pi w_0^2}{\sinh\left(n\pi w_0/a\right)}. \tag{5.4}$$

The first few $\tilde{V}_{mig}(n)$ are shown as functions of the equilibrium kink width $2w_0$ in Figure 5.1. We see that for realistic kink widths of more than $2a$ the leading term $\tilde{V}_{mig}(1)$ dominates by a factor of at least ten, allowing us to approximate the migration potential as a sinusoid of period a. The kink energy (5.4) has a minimum when the kink center of mass lies between two nodes, $X = na + a/2$, as in this configuration no node lies at the maximum of the substrate potential. This minimum kink energy, which should be equated to the formation energy from the relaxed atomistic simulation, is thus

$$E_{kink} = \frac{w_0 V_P}{4} - \frac{E_{mig}}{2}, \tag{5.5}$$

$$E_{mig} = 2\tilde{V}_{mig}(1) = \frac{V_P}{2a}\frac{\pi w_0^2}{\sinh\left(\pi w_0/a\right)}. \tag{5.6}$$

The form of the migration barrier E_{mig} provides insight into the observed behaviour of kinks in atomistic simulation. As can be seen in Figure 5.1, E_{mig} decreases rapidly with the equilibrium kink width, in agreement with the observation that the narrow kinks on edge dislocations have a significant migration barrier as compared to the essentially free motion of the wide kinks on screw dislocations. These significant effects would be entirely lost in any continuum model, emphasizing the importance of atomistic resolution in modelling dislocation dynamics.

5.2. Langevin simulation

We now introduce the stochastic equations of motion which govern the dynamics of the FKL model (5.1). We recall that the atomistic data was time-averaged. Applying the same procedure to our model is formally equivalent to taking a strong damping limit[15, 40] and thus permits a first order equation of motion for the node displacements. This approximation is supported by the absence of any ballistic motion, even over short time intervals, in the simulation data. The output from the stochastic model may thus be subjected to identical analysis as the output from atomistic simulation, allowing us to determine whether the data produced is statistically equivalent.

The thermal behaviour of the system is investigated through the stochastic

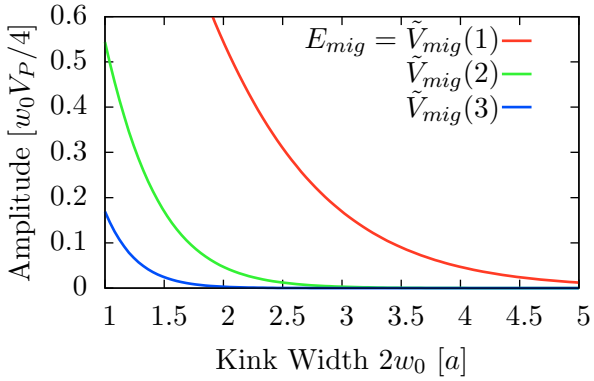

Figure 5.1.: The magnitude of the first three summands in the kink energy (5.4) as a function of the equilibrium kink width w_0. We see the leading term $\tilde{V}_{mig}(1)$ dominates but all three terms decrease rapidly with increasing w_0. (Color Online)

integration of first order Langevin equations[15], which balance a frictional force proportional to the velocity, $-\gamma_{line}v$, the conservative force $-\partial V/\partial u$ and a 'fluctuation force' which will be detailed below. This simplified equation of motion allows us to integrate the system on a much coarser timescale. In addition, any notion of a dislocation mass is assigned to the dissipation parameter γ_{line}, which measures the rate of momentum transfer from the dislocation to the heat bath. In this way we avoid the controversial concept of dislocation inertia as inertial effects were not exhibited in the atomistic simulations we wish to reproduce with this model. The first order equation of motion for our discrete system (5.1), with boundary conditions (5.2), is

$$\gamma_{line}\frac{du_n(t)}{dt} = -\frac{\partial}{\partial u_n}V(\{u_m\}) + \eta_n(t) \tag{5.7}$$

where γ_{line} is the dissipation parameter for the dislocation line and the $\{\eta_n(t)\}$ are independent Gaussian random variables[38] representing the stochastic force from the surrounding heat bath. They are defined under an ensemble average $\langle ... \rangle$ of all heat baths at a temperature T, possessing only an average and standard deviation by the central limit theorem. These read

$$\langle \eta_n(t) \rangle = 0, \quad \langle \eta_n(t)\eta_m(t') \rangle = 2\gamma_{line}T\delta_{nm}\delta(t'-t). \tag{5.8}$$

The amplitude of the fluctuations $\sqrt{2\gamma_{line}T}$ is uniquely determined by the fluctuation-dissipation theorem, which requires that the steady state solution to the Fokker-Planck equation associated with (5.7) is the canonical distribution[15]. The absence of any spatial correlation in the noise forces reflects the chaotic atomic dynamics of the surrounding heat bath and does not preclude any correlation in the dislocation motion; however the delta function $\delta(t'-t)$ is strictly the limiting case of a vanishingly small correlation time in the atomic collisions which constitute the heat bath[38]. This limit may be taken only when we operate on a sufficiently coarse timescale much longer than an individual collision, which is indeed the case in the first order equations of motion investigated here.

We now have a completely specified system; we will integrate the equations stochastically (5.7), using a pseudorandom number algorithm[89] to generate the stochastic forces (5.8). However, in order to have expressions

for all the quantities extracted from atomistic simulation in terms of the model parameters we must also derive the kink diffusion constant.
To do this, we obtain first the kink equation of motion, assuming that the kink position $X(t)$ is slowly varying in time in comparison to the fluctuations of the $\{u_n\}$, and that the kink shape suffers only small perturbations due to these fluctuations throughout its motion. It will be seen that these approximations still give excellent agreement with the results from stochastic integration, and allow us to equate the field center of mass to the kink position $X(t)$. To derive the kink equation of motion we evaluate the total velocity projected along the dislocation line. We consider segments connecting neighbouring nodes of the dislocation line and take the projection of the nodal velocity along the segment normal. We then take the projection of this normal along the line direction $\hat{\mathbf{x}}$ to obtain the contribution to the net projection from that segment. A very similar calculation is used when calculating the driving force on a ship's sail[90] and is formally equivalent to the derivation of the field momentum of (5.1) in the continuum limit[86]. It can be shown that this gives a kink velocity

$$\dot{X}(t) = \sum_n \frac{du_n(t)}{dt} \left(\frac{u_{n+1}(t) - u_n(t)}{a} \right). \tag{5.9}$$

Using (5.7), (5.4) and (5.3) we obtain the kink equation of motion

$$\gamma_{kink} \dot{X}(t) = \frac{\pi}{a} E_{mig} \sin \frac{2\pi X(t)}{a} + \eta(t), \tag{5.10}$$

where the kink dissipation parameter γ_{kink} is given by

$$\gamma_{kink} = \frac{L_P}{4\pi w_0} \gamma_{line}, \tag{5.11}$$

$\eta(t)$ is a one dimensional Gaussian random variable with an average and standard deviation

$$\langle \eta(t) \rangle = 0, \quad \langle \eta(t)\eta(t') \rangle = 2\gamma_{kink} T \delta(t' - t), \tag{5.12}$$

and E_{mig} is given in equation (5.5). We note that equation (5.11) shows the dissipation parameter for the dislocation line, γ_{line}, to be directly proportional to the dissipation parameter for the kink, γ_{kink}, and thus γ_{line} is also

temperature independent. Equation (5.10) describes a point particle undergoing one dimensional stochastic motion in a sinusoidal potential. Under an ensemble average the mean squared displacement exhibits diffusive behaviour with a diffusion constant (4.8), where now E_{mig} and γ_{kink} are given explicitly in terms of the free model parameters $V_P, \gamma_{line}, \kappa$ and the crystallographically determined L_P, a. By inverting the relations (5.3), (5.5) and (5.11) we may determine the model parameters for the dislocations considered here. With these parameters, the system (5.1) was first relaxed by a conjugate gradient algorithm, with the boundary conditions (5.2), to determine the formation energy and kink width, then the equations of motion (5.7) were stochastically integrated. The kink formed remains well defined at finite temperature. It can be seen that the data is identical in form to that produced from atomistic simulation, shown in Figure 4.3, with the kink trajectories extracted and analysed in an identical manner. Table 5.1 shows the results from these simulations as compared to the results from atomistic simulation, displaying excellent agreement over a wide range of temperature.

It is emphasized that the discreteness of the model is essential to produce a kink migration barrier. We also note that the discreteness, which is determined by the underlying crystallography through a and L_P, influences the kink formation energy as well as the migration barrier, as can be seen in equation (5.5). As we simulate a line of only ~ 500 nodes on a coarse time step of 10 ps, as opposed to the entire atomistic system of $700,000$ atoms on a very fine time step of 1 fs, we may generate data sets equivalent to those produced from atomistic simulation at around $\sim 10^{-7}$ of the computational cost. Therefore, despite the atomistic resolution along the line, the model affords enormous computational savings as compared with a full MD simulation. This significant efficiency gain allows us to simulate dislocation motion at experimental strain rates, while retaining atomistic resolution and a statistically rigorous temperature.

Dislocation System	Simulation Method	E_{kink} [eV]	E_{mig} [eV]	γ_{kink} [$m_u ps^{-1}$]
1/2[111]($1\bar{2}1$) Edge	MD	0.150	0.074	1.79
	FKL	0.148	0.072	1.74
[100](010) Edge	MD	0.510	0.222	2.61
	FKL	0.505	0.218	2.58
1/2[111]($1\bar{1}0$) Screw	MD	0.367	-	1.83
	FKL	0.367	-	1.82

Table 5.1.: Formation energies, migration energies and dissipation parameters obtained from MD and FKL simulations for kinks on the dislocations investigated here. The values were obtained by identical processing for each simulation technique. The MD data for kinks on screw dislocations is the average between left and right kinks as detailed in the text. Very good agreement between the MD and FKL parameters is seen.

5.3. Comparison of parametrised models to experiment

The parameters obtained from the kink diffusion simulations are now used to investigate the motion of straight dislocations at experimental stress levels. This important regime is not accessible to atomistic simulation for dislocations which have a large kink formation energy. Therefore, this is an ideal application of the FKL model. For a discrete dislocation segment of N nodes, we supplement the equations of motion (5.7) with a force per node f to induce drift of the dislocation line,

$$\gamma_{line}\frac{du_n(t)}{dt} = -\frac{\partial}{\partial u_n}V(\{u_m\}) + f + \eta_n(t), \tag{5.13}$$

with periodic boundary conditions

$$u_n(t) = u_{n+N}(t). \tag{5.14}$$

We then extract the position of the center of mass $\bar{u} = \sum_n u_n/N$ at each timestep, obtaining the ensemble average center of mass velocity $\langle\bar{v}\rangle$ in an

identical manner to that shown in equation (4.4),

$$\langle \bar{v} \rangle = \sum_{n=0}^{N-\tau/\Delta t} \frac{(\bar{u}_{n\Delta t+\tau} - \bar{u}_{n\Delta t})}{\tau(N - \tau/\Delta t)}. \tag{5.15}$$

To obtain the relationship between the force f and an applied stress, we recall the Peach-Koehler formula[5] for the force per unit length $\mathbf{f}_{PK}$ on a dislocation of Burgers vector $\mathbf{b}$ and line direction $\mathbf{t}$ under an applied stress σ,

$$\mathbf{f}_{PK} = (\sigma \cdot \mathbf{b}) \wedge \hat{\mathbf{t}}. \tag{5.16}$$

The nodal force f is then the projection of (5.16) along the displacement direction of the $\{u_n\}$, $\hat{\mathbf{u}}$, multiplied by the segment separation a. We apply a shear stress across the slip plane of magnitude $|\sigma|$ in the direction of the dislocation Burgers vector $\mathbf{b}$, resulting in a force per node of

$$f = a\mathbf{f}_{PK} \cdot \hat{\mathbf{u}} = a|\mathbf{b}||\sigma|. \tag{5.17}$$

We apply experimental stresses of 40 MPa, which corresponds to a very small force per node of $\sim 10^{-3}\text{eV}/L_P$. To demonstrate phenomena this discrete model can treat, we investigate the effect of segment length on dislocation velocity. Figures 5.2,5.3 show typical center of mass trajectories of $1/2[111](1\bar{1}0)$ screw and $[100](010)$ edge dislocation segments. Extracting the center of mass velocity through equation (5.15) over a wide range of segment lengths gave a length independent velocity for edge segments, whereas the velocity increased linearly with segment length as $0.013(4)s^{-1}$ at 300K for screw dislocations. This is in good agreement with the linear relationship of velocity with length of around $0.01s^{-1}$ at 300K for screw dislocation segments that has recently been observed experimentally[8]. We note that this gradient depends exponentially on temperature due to the activated nature of the dislocation migration.

We can understand these differences in terms of the discrete structure of the FKL dislocation lines. We have seen that the wide kinks on screw dislocations have a negligible migration barrier; as a result, once a double kink is formed it will move quickly under the applied stress until it meets another kink. For long segments we therefore expect the dislocation velocity to scale linearly with segment length due the increased number of possible locations

for kink nucleation, as observed. In contrast, as the narrow kinks on edge dislocations have a large kink migration barrier, comparable to the kink formation energy. As a result we expect the mobility always to be independent of the segment length as kink migration and kink nucleation occur on similar timescales. This behaviour, which is found only in a discrete line model, is expected to have consequences in many aspects of dislocation behaviour, for example the difference in the effect of impurities on the mobilities of edge and screw dislocations[5].

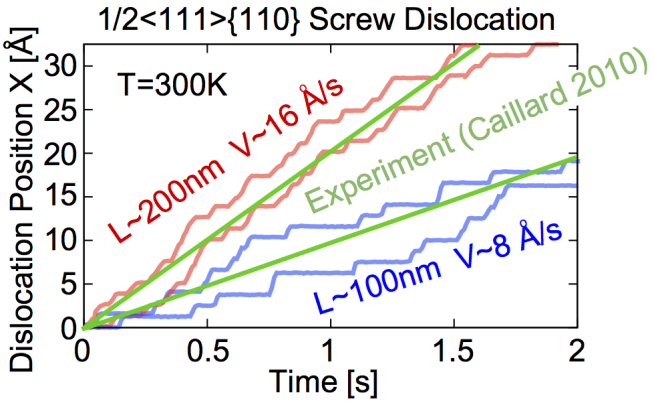

Figure 5.2.: Center of mass positions for two $1/2[111](1\bar{1}0)$ screw dislocation segments, under an applied stress of 40 MPa, at a temperature of 300K. The highly stepped motion reflects directly the nucleation of kinks, which then quickly propagate along the entire line due to the negligible kink migration barrier. As a result longer lines, which have a greater number of nucleation sites, have a velocity which increases linearly with segment length. The ensemble average velocities are in very good agreement with experimental measurements of screw dislocation velocities[8].

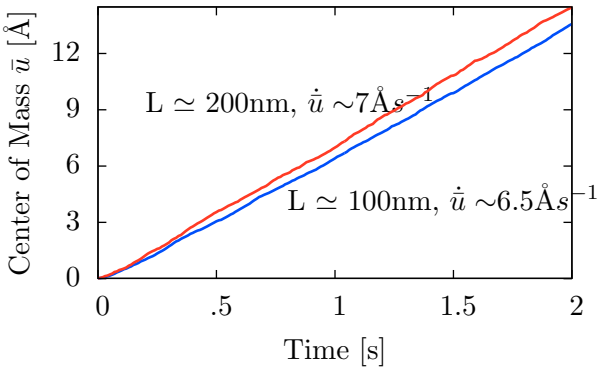

Figure 5.3.: Center of mass positions for two [100](010) edge dislocation segments, under an applied stress of 40 MPa, at a temperature of 600K. As the kink migration barrier is comparable to the kink formation energy double kink nucleation occurs on the same timescale as kink migration and thus the line propagates gradually. As a result the segment velocity is almost independent of the segment length, as distinct from screw dislocation segments, a feature not captured by a continuum line model.

5.4. Elastic Interactions in Double Kink Nucleation

A common criticism of the FKL model is its inability to capture the long range kink interaction predicted from elasticity and the different formation energies of left and right kinks seen in atomistic simulation. As the asymmetric kink formation energy was seen to result from the long range fields of the kinks, the simplest term which captures this behaviour is linear in the dislocation line gradient[85] and consequently will not affect the equations of motion as it may be integrated out of the Lagrangian[91]. Investigation of more complicated terms of cubic order in the line gradient is in principle possible, though the additional complexity would significantly affect the parametrisation procedure whilst very little difference was found in the diffusivities of left and right kinks, meaning that interaction effects would have to be studied in great detail. In effect the standard FKL model treats the localized, symmetric kink 'cores' shown in the lower panel of Figure 4.9.

Whilst the kink formation energy asymmetry is not immediately suited to

the FKL model, it is still possible to capture the long range interaction between kinks, allowing a direct assessment of kink interaction effects on screw dislocation motion in the physically important low stress, high temperature regime studied above. To achieve this we modify the node interaction term in the original FK model beyond nearest neighbours. In order to reproduce the observed $1/d$ kink-kink interaction energy for large kink-kink separation whilst retaining a typical line tension we will let the nodes interact through the following potential

$$V_{\mathrm{LR}} = a\frac{\kappa}{2}\sum_{ij}\frac{(u_{j+1}-u_j)(u_{i+1}-u_i)}{a^2\sqrt{1+(i-j)^2/\alpha^2}} + aV_P\sum_i \sin^2\left(\pi\frac{u_i}{L_P}\right), \tag{5.18}$$

where α controls the range of interaction. Some key differences from the standard FK model are best seen by taking the continuum limit, obtaining

$$V_{\mathrm{LR}} \to \frac{\kappa}{2}\int_{\mathbb{R}^{\not=}}\frac{u'(x)u'(y)}{\sqrt{1+(x-y)^2/a^2/\alpha^2}}\mathrm{d}x\mathrm{d}y + V_P\int_{\mathbb{R}}\sin^2\left(\pi\frac{u(x)}{L_P}\right)\mathrm{d}x. \tag{5.19}$$

We first calculate the dispersion relation in the free case ($V_P = 0$) by taking a spatial Fourier transform. For the standard FK model it clear that we have

$$\omega^2_{\mathrm{FK}}(k) = \frac{\kappa}{m}k^2, \tag{5.20}$$

which now becomes (using the convolution theorem)

$$\omega^2_{\mathrm{LR}}(k) = \frac{\kappa}{m}k^2K_0(k/\alpha), \tag{5.21}$$

where $K_0(k/\alpha)$ is the zeroth hyperbolic modified Bessel function[64]. This function rises sharply with k, meaning that high frequency modes have a much higher energy cost in this model, meaning high temperature fluctuations will be markedly different. We now derive the interaction energy of two widely separated kinks at x^A, x^B. Whilst we do not know the exact functional form for the kink profile $u(x - x^{A,B})$, in analogy to the FK model we assume that on a coarse length scale the profile gradient can be approximated by

$$u'(x - x^{A,B}) \simeq \sqrt{\frac{E_k}{\kappa}}\delta(x - x^{A,B}). \tag{5.22}$$

Substituting $u(x) = u(x - x^A) + u(x - x^B)$ into (5.19) we obtain an approximate far field interaction energy of

$$E_{\text{int}}(x^A - x^B) \simeq \frac{E_k}{\sqrt{1 + (x^A - x^B)^2/a^2/\alpha^2}} \to \frac{\alpha a E_k}{|x^A - x^B|}, \tag{5.23}$$

which exhibits the desired $1/d$ dependence observed in MD simulation and predicted by elasticity theory. This system may be stochastically integrated in an identical method to that detailed above. Figure 5.4 shows the free energy landscape (see the next section) of double kink nucleation for the FK chain and the long range chain for different values of α, both possessing a large κ/V_P ratio which ensures highly mobile, wide kinks. Whilst the free energy of the FK chain reaches a plateau quickly after double kink nucleation, the long range chain clearly shows a long range kink-kink interaction which can be determined to decay inversely with separation.

Figure 5.5 compares the drift velocity of a FK chain and a long range chain with a strong kink-kink interaction. Significantly we find that in the low stress regime, where the experimentally comparable results above were taken, the two chain have very similar drift velocities. This both challenges previous theories of screw dislocation mobility which rely on a kink-kink interaction to produce phenomenological mobility laws and explains how the FK model can accurately capture the experimental data even without the long-range kink interaction.

In the intermediate to high stress regime the two systems show quite distinct behaviour; the investigation of this motion is a topic for future work.

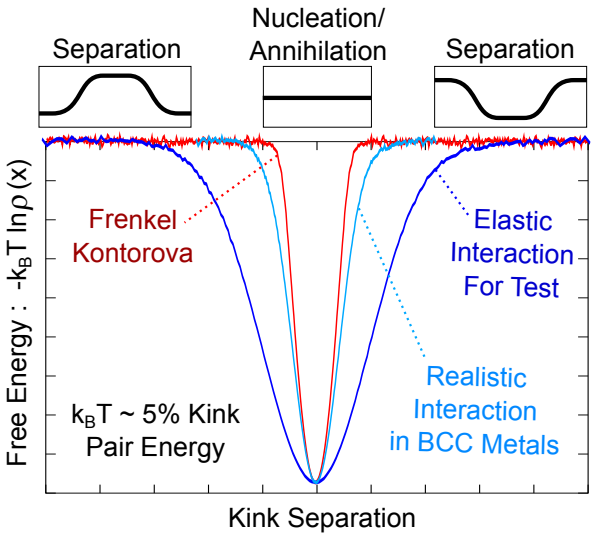

Figure 5.4.: Free energy obtained through a histogram method, see next section) of various long range chains and a FK chain. The long range chains clearly show a kink-kink interaction beyond the FK model.

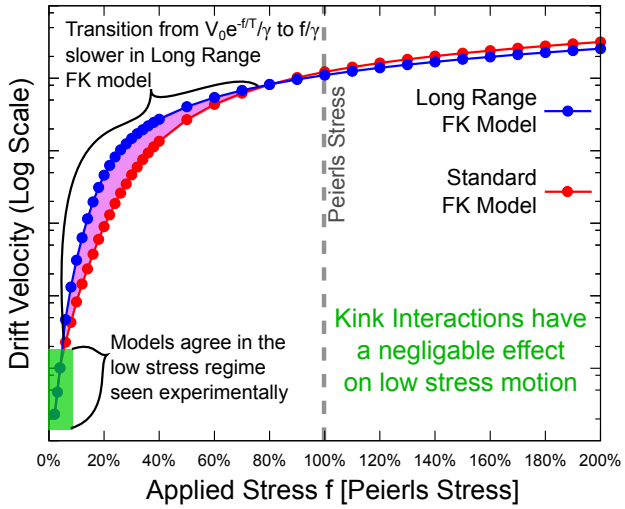

Figure 5.5.: Drift velocity for a FK and long range chains. We see the low stress mobility is unaffected by the long-range kink interaction, a significant result.

5.5. Homogenisation of the Frenkel-Kontorowa Chain

We now will look at the FKL model in a more general setting, though one which still has clear applications to dislocation theory. It is perhaps unsurprising that a chain of harmonically coupled particles, each executing one dimensional stochastic motion in a periodic potential, is one of the most extensively studied examples of many-body, non-linear dynamics. First studied by Prandtl[92] and Dehlinger[93] though often named after later work by Frenkel and Kontorova[94], the rich, kink bearing phenomenology has found application in dislocation theory[1, 95], polymer dynamics[96], molecular combustion[97], Josephson junctions[98], spin chains[99], earthquakes[100] and many other areas for decades[101, 102]. In the general case, illustrated in Figure 5.6, a Frenkel-Kontorova (FK) chain of N particles with one dimensional positions $\mathbf{x} = \{x_n\}_{n=1}^N$ has a potential energy

$$U(\mathbf{x}) = \frac{1}{2}\mathbf{x}\cdot\mathbf{K}\cdot\mathbf{x} + V(\mathbf{x}), \tag{5.24}$$

where $\mathbf{K}$ is a positive semi definite matrix representing the harmonic interaction and $V(\mathbf{x})$ is simply a sum of one dimensional periodic potentials $V_{1\mathrm{D}}(x) = V_{1\mathrm{D}}(x+L)$

$$V(\mathbf{x}) = \sum_{n=1}^{N} V_{1\mathrm{D}}(x_n). \tag{5.25}$$

The system is completed with chain boundary conditions, which will be periodic in the following. As the FK chain traditionally models the collective motion of some generalized charges, it is of central interest to know the transport properties of the chain center of mass

$$\bar{x} = \sum\nolimits_n x_n/N, \tag{5.26}$$

in particular the diffusivity D and by Einstein's relation the linear response mobility βD, where $\beta = 1/k_{\mathrm{B}}T$. Whilst it is known[103] that the center of mass is diffusive at asymptotic time, the actual value of the diffusion constant D has only been approximately evaluated for some special cases, in particular for long, continuous lines at low temperature, where the system has been considered as a dilute kink gas[104, 105]. In con-

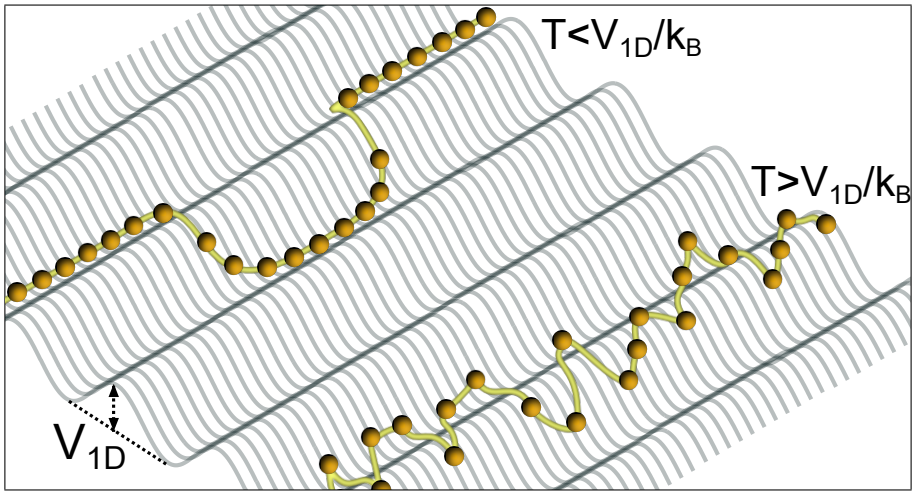

Figure 5.6.: A Frenkel-Kontorova chain. At low temperature (left) the chain moves through the kink mechanism, whilst at high temperature (right) internal fluctuations destroy any migration barrier.

trast, many applications of interest are to highly discrete chains over a wide temperature range which are often short due to either physical[98, 50] or computational[95, 66] restrictions. In this section I derive rigorous upper and lower bounds for D, giving important context for existing approaches such as transition state theory[62] and providing rigorous results for many body diffusive transport.

Through comparing the bounds to the well known point particle result[61, 106] it is shown that the upper bound represents diffusion in the free energy landscape of $\bar{x}$. The free energy barrier is often used as the finite temperate migration barrier[107]; these results show that this will always give an overestimate for the transport properties of the FK chain, an important result given the generality of this widely applied model.

The section is structured as follows. In subsection 5.5.1 the adjoint Fokker-Planck equation[40] is recalled, then multiscale analysis is employed to perform a diffusive rescaling in subsection 5.5.2, deriving an one dimensional evolution equation for the center of mass. The Cauchy-Schwartz inequality is then used to derive strict upper and lower bounds for the effective diffusion constant D. In subsection 5.5.3 I investigate limiting cases of the exact bounds, present numerical results in subsection 5.5.4 and propose a non-linear response through analogy to the famous point particle result of

Stratonovich[108, 109] in subsection 5.5.5, where surprisingly accurate results are found.

5.5.1. Adjoint Fokker-Planck equation

For later manipulations it will be beneficial to transform to a coordinate system which distinguishes the center of mass. This is achieved by diagonalising the interaction matrix $\mathbf{K}$, which will always have non-negative eigenvalues $\{\lambda_k\}_{k=1}^N$ and an orthonormal eigenbasis $\{\hat{\mathbf{v}}_k\}_{k=1}^N$. By the requirement that the interaction energy is unchanged under a rigid translation, there will always be a zero eigenvalue, $\lambda_1 = 0$, with the corresponding eigenvector $\hat{\mathbf{v}}_1$ having every element equal, projecting out the center of mass $\bar{x}$. The chain configuration vector $\mathbf{x}$ becomes

$$\mathbf{x} = \bar{x}\sqrt{N}\hat{\mathbf{v}}_1 + \sum_{k=2}^{N} a_k \hat{\mathbf{v}}_k \quad , \quad a_k = \mathbf{x} \cdot \hat{\mathbf{v}}_k, \tag{5.27}$$

which defines the desired co-ordinate system $(\bar{x}, \{a_k\})$. The potential energy (5.24) now reads

$$U(\bar{x}, \{a_k\}) = \sum_{k=2}^{N} \frac{1}{2}\lambda_k a_k^2 + V(\bar{x}, \{a_k\}), \tag{5.28}$$

where the substrate potential is explicitly

$$V(\bar{x}, \{a_k\}) = \sum_{n=1}^{N} V_{1\mathrm{D}} \left(\bar{x} + \sum_{k=2}^{N} a_k (\hat{\mathrm{v}}_k)_n \right), \tag{5.29}$$

which is clearly periodic in $\bar{x}$. One may now write down the adjoint Fokker-Planck equation[40], which governs the expected time evolution of a smooth function $\Phi(t; \bar{x}, \{a_k\})$ from some initial values $(\bar{x}, \{a_k\})$. For the investigation of transport properties, the adjoint Fokker-Planck equation is preferable to the Fokker-Planck equation as it is concerned with observables rather than probability densities, but any results may be rigorously transferred between the two presentations, in close analogy to the Schrödinger and Heisenberg representations of quantum mechanical operators[40]. For the

system (5.28) the adjoint Fokker-Planck equation reads

$$N\beta\gamma\frac{\partial\Phi}{\partial t} = \hat{\mathrm{L}}_{\mathrm{aFP}}\Phi \equiv -\beta\frac{\partial U}{\partial\bar{x}}\frac{\partial\Phi}{\partial\bar{x}} + \frac{\partial^2\Phi}{\partial\bar{x}^2} + N\sum_{k=2}^{N}\left(-\beta\frac{\partial U}{\partial a_k}\frac{\partial\Phi}{\partial a_k} + \frac{\partial^2\Phi}{\partial a_k^2}\right), \tag{5.30}$$

where $\hat{\mathrm{L}}_{\mathrm{aFP}}$ is the adjoint Fokker-Planck operator, U is given by (5.28) and γ is the friction parameter, which measures the rate of momentum transfer to the heat bath (a factor of $N\beta\gamma$ has been taken to the left hand side of (5.30) to simplify later notation). For the overdamped limit to be valid, which amounts to a 'Born-Oppenheimer' decoupling of position and momentum, γ is required to be much greater than the curvatures of U[38]. Familiar statistical mechanics arises upon averaging over the initial conditions and asking for the steady state; the condition for the probability density of states $\rho_\infty(\bar{x},\{a_k\})$ is

$$0 = \int_{\bar{x},\{a_k\}}\left(\hat{\mathrm{L}}_{\mathrm{aFP}}\Phi\right)\rho_\infty = \int_{\bar{x},\{a_k\}}\left(\hat{\mathrm{L}}^*_{\mathrm{aFP}}\rho_\infty\right)\Phi, \tag{5.31}$$

where $\hat{\mathrm{L}}^*_{\mathrm{aFP}}$ is the L^2 adjoint of $\hat{\mathrm{L}}_{\mathrm{aFP}}$[110], producing the overdamped Fokker-Planck (or Smolchowski) equation. As is well known, the unique solution is Gibbs' distribution

$$\hat{\mathrm{L}}^*_{\mathrm{aFP}}\rho_\infty = 0 \quad \Rightarrow \quad \rho_\infty = e^{-\beta U}/Z, \tag{5.32}$$

where Z is the partition function. Due to the periodicity of U in $\bar{x}$, the Fokker-Planck operator and thus any unique solution will also be periodic in $\bar{x}$; however, for the steady state (5.32) to exist in this case we require $\bar{x}\in[0,L]$, which clearly forbids diffusion. To extract a diffusion constant we will use multiscale analysis in the next subsection to investigate the diffusive dynamics of a coarse grained center of mass $\bar{\chi}\in[-\infty,\infty]$, which is asymptotically independent of $\bar{x}\in[0,L]$ as the scale separation diverges.

Throughout this section integrals over $\bar{x}$ and the $\{a_k\}$ will be denoted as $\int_{\bar{x},\{a_k\}}$, with the bounds of integration being $[0,L]$ for $\bar{x}$ and $[-\infty,\infty]$ for each a_k. Integrals over only the $\{a_k\}$ will be denoted as $\int_{\{a_k\}}$, again integrating over $[-\infty,\infty]$ for each a_k. The proof[110, 111, 112] of ergodicity

and the existence of an unique steady state (5.32) for potentials of the form (5.28) follows from the quadratic confinement of $\sum_p \lambda_p a_p^2/2$ and the boundedness of $V(\bar{x}, \{a_p\})$.

5.5.2. Multiscale analysis

The techniques used in the following are detailed in the recent book by Pavliotis and Stuart[39], an accessible introduction which contains extensive references, though it is believed that the present application to a many body system is new material.

The central idea behind multiscale analysis is that at long times unbound variables can have unbound expectation values, which will be much larger than any length scale imposed by the potential environment. In the present case the unbound variable is the center of mass $\bar{x}$, whose variance at asymptotic time diverges linearly and therefore will be much greater than the potential period L. As a result, to extract an effective diffusion constant one may work on a coarse grained time and length scale which will be insensitive to details of the underlying potential. This is often what occurs in simulation or experiment; it is achieved analytically through first rescaling time as

$$t \to \frac{t}{\epsilon^2} \quad , \quad 0 < \epsilon \ll 1, \tag{5.33}$$

then identifying the 'slow' spatial variable

$$\bar{\chi} = \epsilon \bar{x}. \tag{5.34}$$

Such an approach was first used by Hilbert to investigate hydrodynamic limits of the Boltzmann equation[113]. On a coarse time scale, of order one as $\epsilon \to 0$, the dynamics of $\bar{x}$ and the $\{a_k\}$ will be massively faster than those of $\bar{\chi}$. In particular, as $\bar{x}$ moves in a periodic potential it will fluctuate extremely rapidly, so that as $\epsilon \to 0$, $\bar{\chi}$ and $\bar{x}$ are scale separated and become independent variables. By this definition, the potential U only depends on $(\bar{x}, \{a_k\})$ as the fast variables will only have a homogenised affect on the slow variable $\bar{\chi}$. Employing the transformations (5.33), (5.34) and using the chain rule, consider functions $\Phi^\epsilon(\bar{\chi}, \bar{x}, \{a_k\})$ which solve the

adjoint Fokker-Planck equation[39]

$$N\beta\gamma\frac{\partial\Phi^\epsilon}{\partial t} = \frac{\partial^2\Phi^\epsilon}{\partial\bar{\chi}^2} + \frac{2}{\epsilon}\frac{\partial^2\Phi^\epsilon}{\partial\bar{x}\partial\bar{\chi}} - \frac{\beta}{\epsilon}\frac{\partial U}{\partial\bar{x}}\frac{\partial\Phi^\epsilon}{\partial\bar{\chi}} + \frac{1}{\epsilon^2}\hat{\mathrm{L}}_{\mathrm{aFP}}\Phi^\epsilon, \tag{5.35}$$

where $\hat{\mathrm{L}}_{\mathrm{aFP}}$ is defined in equation (5.30) and acts only on $(\bar{x}, \{a_k\})$. In the absence of any potential landscape, equation (5.35) would represent free diffusion for $\bar{\chi}$, justifying the scaling operations (5.33) and (5.34). By the aforementioned periodicity of U, Φ^ϵ will be periodic in $\bar{x}$[1]

meaning $\bar{x}$ can be constrained to take values in the interval $[0, L]$. To look for an explicit solution, perform a multiscale expansion of Φ^ϵ in orders of the small parameter ϵ,

$$\Phi^\epsilon = \Phi_0 + \epsilon\Phi_1 + \epsilon^2\Phi_2 + ..., \tag{5.36}$$

where at asymptotic time the solution will be given by Φ_0. Substituting (5.36) into (5.35) produces a hierarchy of equations in orders of $(1/\epsilon)$, reading

$$O\left(\frac{1}{\epsilon^2}\right) : \hat{\mathrm{L}}_{\mathrm{aFP}}\Phi_0 = 0, \tag{5.37}$$

$$O\left(\frac{1}{\epsilon}\right) : \hat{\mathrm{L}}_{\mathrm{aFP}}\Phi_1 - \beta\frac{\partial U}{\partial\bar{x}}\frac{\partial\Phi_0}{\partial\bar{\chi}} + 2\frac{\partial^2\Phi_0}{\partial\bar{x}\partial\bar{\chi}} = 0, \tag{5.38}$$

$$O\left(1\right) : \hat{\mathrm{L}}_{\mathrm{aFP}}\Phi_2 + \frac{\partial^2\Phi_0}{\partial\bar{\chi}^2} + 2\frac{\partial^2\Phi_1}{\partial\bar{\chi}\partial\bar{x}} - \beta\frac{\partial U}{\partial\bar{x}}\frac{\partial\Phi_1}{\partial\bar{\chi}} = N\beta\gamma\frac{\partial\Phi_0}{\partial t}. \tag{5.39}$$

To reduce these hierarchy of equations into a single effective equation for Φ_0 it is required to solve Poisson equations of the form

$$\hat{\mathrm{L}}_{\mathrm{aFP}} f(\bar{\chi}, \bar{x}, \{a_k\}, t) = g(\bar{\chi}, \bar{x}, \{a_k\}, t), \tag{5.40}$$

for two smooth functions f and g which satisfy the normalisation condition

[1] To see the $\bar{x}$-periodicity of any solution $\Phi(\bar{\chi}, \bar{x}, \{a_{p>0}\})$, note that $\hat{\mathrm{L}}_{\mathrm{aFP}}$ acts on $(\bar{x}, \{a_k\})$ and is invariant under a shift in $\bar{x}$ by nL, where n is an integer. For the solution $\Phi(\bar{x}+nL, \{a_{p>0}\})$ to be unique we thus require $\Phi(\bar{\chi}, \bar{x}+nL, \{a_{p>0}\})$=$\Phi(\bar{\chi}, \bar{x}, \{a_{p>0}\})$, giving the desired result.

$$\int_{\bar{x},\{a_k\}} \rho_\infty(\bar{x},\{a_k\})|f(\bar{\chi},\bar{x},\{a_k\},t)|^2 < \infty, \tag{5.41}$$

where ρ_∞ is given by (5.32), and is a restatement of the requirement that the expectation values are finite after a finite time. Due to the smoothness of the parabolic operator $\hat{\mathrm{L}}_{\mathrm{aFP}}$, it is well known[110, 39, 114] that (5.40) has a unique solution (up to constants) if and only if

$$\int_{\bar{x},\{a_k\}} \rho_\infty(\bar{x},\{a_k\})g(\bar{\chi},\bar{x},\{a_k\},t) = 0. \tag{5.42}$$

This condition may be justified by considering acting on (5.40) with ρ_∞ and integrating over the support of the exponent, which as defined above is $[0,L]$ for $\bar{x}$ and $(-\infty,\infty)$ for $\{a_k\}$. Providing the normalisation condition holds, use (5.31) and (5.40) to show

$$\int_{\bar{x},\{a_k\}} \rho_\infty g = \int_{\bar{x},\{a_k\}} f\hat{L}^*_{\mathrm{aFP}}\rho_\infty = 0. \tag{5.43}$$

Now apply the conditions (5.41), (5.42) to the equations (5.37), (5.38), (5.39), which are all of the form (5.40). The first equation, (5.37), acts on $(\bar{x},\{a_k\})$ and thus by uniqueness Φ_0 is a function only of $\bar{\chi}$ and t,

$$\Phi_0(\bar{\chi},\bar{x},\{a_k\},t) = \Phi_0(\bar{\chi},t). \tag{5.44}$$

Condition (5.41) requires that for a solution of (5.38) to exist

$$-\beta\int_{\bar{x},\{a_k\}} \rho_\infty \frac{\partial U}{\partial \bar{x}}\frac{\partial \Phi_0}{\partial \bar{\chi}} = \left(\int_{\bar{x},\{a_k\}} \frac{\partial \rho_\infty}{\partial \bar{x}}\right)\frac{\partial \Phi_0}{\partial \bar{\chi}} = 0, \tag{5.45}$$

which is clearly satisfied as ρ_∞ is periodic in $\bar{x}$. This allows one to try a separated variable solution of the form

$$\Phi_1(\bar{\chi},\bar{x},\{a_k\},t) = \phi(\bar{x},\{a_k\})\frac{\partial \Phi_0}{\partial \bar{\chi}}, \tag{5.46}$$

which when substituted into (5.38) gives

$$\hat{\mathrm{L}}_{\mathrm{aFP}}\phi = \frac{\partial U}{\partial \bar{x}}. \tag{5.47}$$

Finally, apply the condition (5.41) to (5.39). Multiply (5.39) by ρ_∞ and integrate over all $(\bar{x},\{a_k\})$. The Φ_2 term disappears by (5.43), to that after an integration by parts,

$$N\beta\gamma\frac{\partial\Phi_0}{\partial t}=\left(\int_{\bar{x},\{a_k\}}\rho_\infty\left(1+\frac{\partial\phi}{\partial\bar{x}}\right)\right)\frac{\partial^2\Phi_0}{\partial\bar{\chi}^2}. \tag{5.48}$$

Equation (5.48) is easily recognisable as an (adjoint) free diffusion equation in $\bar{\chi}$ with an effective diffusion constant

$$D=\frac{1}{N\beta\gamma}\int_{\bar{x},\{a_{p>0}\}}\rho_\infty\left(1+\frac{\partial\phi}{\partial\bar{x}}\right). \tag{5.49}$$

It simple to show that with $\Phi_0{=}\langle\bar{\chi}^2\rangle$ one obtains $\langle\bar{\chi}^2\rangle{=}2Dt$. Digressing briefly, the form of the reduced diffusivity can be understood by first considering the operator identity $\hat{\mathrm{L}}^{-1}=\int_0^\infty\exp(-\hat{\mathrm{L}}t)\mathrm{d}t$, which in conjunction with (5.47) gives $\phi=\frac{1}{N\gamma}\int_0^\infty\exp(-\hat{\mathrm{L}}t)\frac{\partial U}{\partial\bar{x}}\mathrm{d}t$ (as $\hat{L}/N\gamma$ is the propagation operator). This means $\phi(\bar{x},\{a_p\})$ is the total impulse for a given initial configuration $(\bar{x},\{a_p\})$. An integration by parts in (5.49) gives

$$D=\frac{1}{N\beta\gamma}+\frac{1}{(N\gamma)^2}\int_0^\infty\int_{\bar{x},\{a_{p>0}\}}\rho_\infty\frac{\partial U}{\partial\bar{x}}\exp(-\hat{\mathrm{L}}t)\frac{\partial U}{\partial\bar{x}}\mathrm{d}t, \tag{5.50}$$

which may be reconciled with the center of mass equation of motion $\dot{\bar{x}}(t)=\frac{-1}{N\gamma}\frac{\partial U}{\partial\bar{x}}+\frac{\eta(t)}{\sqrt{N\beta\gamma}}$ to give

$$D=\int_0^\infty\int_{\bar{x},\{a_{p>0}\}}\rho_\infty\langle\dot{\bar{x}}(0)\dot{\bar{x}}(t)|\bar{x},\{a_{p>0}\}\rangle\mathrm{d}t, \tag{5.51}$$

which is the well-known Green-Kubo relation $D=\int_0^\infty\langle\dot{\bar{x}}(0)\dot{\bar{x}}(t)\rangle\mathrm{d}t$.

We now return to finding bounds on D. To simplify the following presentation, I work with the reduced diffusivity $\tilde{D}=N\beta\gamma D$. Using (5.47) and (5.30), $\tilde{D}$ may be written

$$\tilde{D}=\int_{\bar{x},\{a_k\}}\rho_\infty\left(\left(1+\frac{\partial\phi}{\partial\bar{x}}\right)^2+\sum_{k=2}^{N}\left(\frac{\partial\phi}{\partial a_k}\right)^2\right). \tag{5.52}$$

I shall use both expressions (5.49), (5.52) in the following subsection where the Cauchy-Schwartz inequality[64] (CSI) is employed to obtain upper and

lower bounds for $\tilde{D}$. Using the normalisation condition (5.41), the CSI reads

$$\left(\int_{\bar{x},\{a_k\}} \rho_\infty f g\right)^2 \leq \left(\int_{\bar{x},\{a_k\}} \rho_\infty f^2\right)\left(\int_{\bar{x},\{a_k\}} \rho_\infty g^2\right). \tag{5.53}$$

For the special case here, where the functions under consideration are smooth, periodic and bounded in $\bar{x}$, one may again use (5.41) to write (See Appendix A.1)

$$\left(\int_{\{a_k\}} \rho_\infty f g\right) \leq \left(\int_{\{a_k\}} \rho_\infty f^2\right)\left(\int_{\{a_k\}} \rho_\infty g^2\right), \tag{5.54}$$

which holds for all $\bar{x} \in [0, L]$. To proceed, note that for any real function ϕ the following inequality is always satisfied

$$\begin{aligned}\tilde{D} &= \int_{\bar{x},\{a_k\}} \rho_\infty \left(\left(1+\frac{\partial\phi}{\partial\bar{x}}\right)^2 + \sum_{k=2}^{N}\left(\frac{\partial\phi}{\partial a_k}\right)^2\right) \\ &\geq \int_{\bar{x},\{a_k\}} \rho_\infty \left(1+\frac{\partial\phi}{\partial\bar{x}}\right)^2.\end{aligned} \tag{5.55}$$

Also define the 'harmonic chain' partition function

$$Z_\lambda = \int_{\{a_k\}} e^{-\beta\sum_k \lambda_k a_k^2/2} = \prod_{k=2}^{N}\sqrt{\frac{\pi}{\beta\lambda_k}}, \tag{5.56}$$

allowing one to write a useful quantity, a conditional average of $\exp(\pm\beta V)$ over all configurations with a center of mass $\bar{x}$ as

$$\langle e^{\pm\beta V}; \bar{x}\rangle = Z_\lambda^{-1}\int_{\{a_k\}} e^{\pm\beta V(\bar{x},\{a_k\})-\beta\sum_k \lambda_k a_k^2/2}, \tag{5.57}$$

meaning in particular that

$$\oint_{\bar{x}} \langle e^{-\beta V}; \bar{x}\rangle = Z_\lambda^{-1}\int_{\bar{x},\{a_k\}} e^{-\beta U(\bar{x},\{a_k\})} = \frac{Z}{Z_\lambda}, \tag{5.58}$$

where $U(\bar{x}, \{a_k\})$ is given by (5.28) and Z is the full partition function. To obtain a lower bound for $\tilde{D}$, use the fact that $\rho_\infty \exp(\beta V)$ is independent of $\bar{x}$ and the periodicity of ϕ in $\bar{x}$ to give

$$\int_{\bar{x},\{a_k\}} \left(1+\frac{\partial\phi}{\partial\bar{x}}\right)\rho_\infty e^{\beta V} = L\frac{Z_\lambda}{Z}. \tag{5.59}$$

Applying the Cauchy-Schwartz inequality (5.53) to (5.59), using (5.55), produces the first main result, a strict lower bound for the center of mass diffusivity,

$$D \geq D_{\mathrm{L}} = \frac{L^2/N\beta\gamma}{\oint_{\bar{x}}\langle e^{-\beta V};\bar{x}\rangle \mathrm{d}\bar{x} \oint_{\bar{y}}\langle e^{\beta V};\bar{y}\rangle \mathrm{d}\bar{y}}. \tag{5.60}$$

To derive an upper bound for D, multiply (5.47) by ρ_∞ and integrate over all $\{a_k\}$, but crucially not $\bar{x}$, to obtain

$$\int_{\{a_k\}} \left(1 + \frac{\partial \phi}{\partial \bar{x}}\right) \rho_\infty = \frac{\tilde{D}}{L}, \tag{5.61}$$

where I have integrated by parts and used (5.49). Applying the second Cauchy-Schwartz inequality (5.53) to (5.61) and using (5.55) results in

$$\frac{\tilde{D}^2}{L^2} \leq \frac{\tilde{D}}{L} \frac{\langle e^{-\beta V};\bar{x}\rangle}{\oint_{\bar{y}}\langle e^{-\beta V};\bar{y}\rangle \mathrm{d}\bar{y}}. \tag{5.62}$$

Whilst integration over $\bar{x}$ simply shows that the reduced diffusivity $\tilde{D} \leq 1$, dividing both sides by $\langle \exp(-\beta V);\bar{x}\rangle$ then integrating produces the second main result, a strict upper bound for the center or mass diffusivity,

$$D \leq D_{\mathrm{U}} = \frac{L^2/N\beta\gamma}{\oint_{\bar{x}}\langle e^{-\beta V};\bar{x}\rangle^{-1} \mathrm{d}\bar{x} \oint_{\bar{x}}\langle e^{-\beta V};\bar{y}\rangle \mathrm{d}\bar{y}}. \tag{5.63}$$

Both bounds benefit from a comparison to the well known diffusivity of a point particle moving in an one dimensional periodic potential $V_{1\mathrm{D}}(x) = V_{1\mathrm{D}}(x+L)$[61, 106]

$$D_{1\mathrm{D}} = \frac{L^2/\gamma\beta}{\int_0^L e^{-\beta V_{1\mathrm{D}}(x)}\mathrm{d}x \int_0^L e^{+\beta V_{1\mathrm{D}}(y)}\mathrm{d}y}. \tag{5.64}$$

Using (5.64) and the bounds (5.60), (5.63) it is simple to show[2] that to within unimportantant constants, the lower (L) and upper (U) bounds are equivalent to the diffusivity of a point particle moving in the periodic potential

$$F_{\mathrm{L,U}}(\bar{x}) = \pm k_{\mathrm{B}}T \ln\langle e^{\pm\beta V};\bar{x}\rangle. \tag{5.65}$$

In particular, from the definition (5.57), $\langle \exp(-\beta V);\bar{x}\rangle$ may be written as

[2] For the analogy to be complete we associate $Z{=}Z_\lambda \int_{\bar{x}}\langle \exp(-\beta V);\bar{x}\rangle$ for the chain with $Z{=}\int_x \exp(-\beta V_{1\mathrm{D}}(x))$ for the point particle.

$Z_\lambda^{-1}\int_{\{a_k\}}\exp(-\beta U)$, so that $F_{\rm U}$ is the Helmholtz free energy landscape of the center of mass[91]. As one may extract the free energy from simulation through a simple histogram method[107] it has become a popular measure of a finite temperature migration barrier, so it is significant that these results show $F_{\rm U}$ to be a lower bound to the true energy barrier experienced by this many body system. I now investigate limiting cases and present simulation results to validate the above analysis.

5.5.3. Limiting Cases

In the low temperature limit $\beta\to\infty$, one may evaluate the integrals over $\{a_k\}$ in the definition (5.57) of $\langle\exp(\pm\beta V);\bar{x}\rangle$ by the method of steepest descents[115]. These evaluations can then be used in a steepest descents evaluation of the bounds (5.60), (5.63).
As it has been seen that $\langle\exp(-\beta V);\bar{x}\rangle$ may be written as $Z_\lambda^{-1}\int_{\{a_k\}}\exp(-\beta U)$, at each value of $\bar{x}$ the integrand will be dominated by the set of coordinates $\{a_k^{\min}(\bar{x})\}$ which minimise U, with a set of $N-1$ second derivatives[3] $\{\omega_k(\bar{x})\}_{k=2}^N$. As a result the conditional average becomes

$$\langle e^{-\beta V};\bar{x}\rangle \xrightarrow[\beta\to\infty]{} \prod_{k=2}^{N}\sqrt{\frac{\lambda_k}{\omega_k(\bar{x})}}e^{-\beta U_{\min}(\bar{x})}, \tag{5.66}$$

where $U_{\min}(\bar{x})$ is the minimum energy of the system at a given value of $\bar{x}$. For a sufficiently long and stiff chains (where the largest eigenvalue of $\mathbf{K}$ is much greater than the magnitude of the on site potential, resulting in a wide, smooth kink profile) this will be the kink anti-kink pair energy $E_{\rm DK}$ for $\bar{x}=\bar{x}^{\rm DK}\gtrsim 2w_k/N$, where w_k is the kink width, unless the structure of $\mathbf{K}$ will give a long range kink interaction[101]. Additionally, one second derivative, say $\omega_2^{\rm DK}$, will become of order $1/N$ due to the vanishingly small kink pair translation barrier[116]. At $\bar{x}=0$ the chain will be straight, with curvatures

$$\omega_k(0)=V_{\rm 1D}''(0)+\lambda_k. \tag{5.67}$$

One may now evaluate the integrals of $\langle\exp(-\beta V);\bar{x}\rangle$ and its inverse in the upper bound (5.63), also by steepest descents at low temperature, which

[3] We emphasise that the N-1 positive curvatures will not in general be diagonal in the $\{a_k\}$ coordinates.

will be dominated by the maximum and minimum values of (5.66) respectively. Letting the Goldstone mode ω_2^{DK} vanish as $1/N$ and recognising that $U''_{\mathrm{min}}(0) = NV''_{\mathrm{1D}}(0)$, the low temperature upper bound reads

$$D_{\mathrm{U}} \to \frac{\sqrt{\pi V''_{\mathrm{1D}}(0)|U''^{\mathrm{DK}}_{\mathrm{min}}|}}{\gamma\sqrt{\beta}} \frac{\prod_{k=2}^{N}\sqrt{\lambda_k + V''_{\mathrm{1D}}(0)}}{\prod_{k=3}^{N}\sqrt{\omega_k^{\mathrm{DK}}}} e^{-\beta E_{\mathrm{DK}}}, \tag{5.68}$$

where $|U''^{\mathrm{DK}}_{\mathrm{min}}|$ is the largest negative curvature of U_{min} (see inset a) of Figure (5.7)). This expression is exactly the Arrhenius result of Kramers' transition state theory[62, 117], with a length (N) independent prefactor. As shown in subsection 5.5.5, when driving the chain with a homogeneous bias f the center of mass feels a force of Nf, meaning that the linear response drift velocity $Nf\beta D_{\mathrm{U}}$ is proportional to the length N, a recognised signature of the kink pair mechanism when the kink migration barrier vanishes[1].

The lower bound (5.60) requires a steepest descents evaluation of

$$\langle e^{\beta V}; \bar{x}\rangle = Z_\lambda^{-1} \int_{\{a_k\}} e^{\beta V(\bar{x},\{a_k\}) - \beta\sum_k \lambda_k a_k^2/2}, \tag{5.69}$$

at each value $\bar{x}$, which as $V > 0$ is dominated by the straight line $a_k = 0$, $k = 2, 3, ..N$ as $\beta \to \infty$. As a result the low temperature limit for D_{L} reads

$$\begin{aligned} D_{\mathrm{L}} \to & \frac{\sqrt{V''_{\mathrm{1D}}(0)|V''_{\mathrm{1D}}(L/2)|}}{\gamma} e^{-\beta N|V_{\mathrm{1D}}|} \\ & \times \prod_{k=2}^{N} \sqrt{\left(1 + \frac{V''_{\mathrm{1D}}(0)}{\lambda_k}\right)\left(1 + \frac{|V''_{\mathrm{1D}}(L/2)|}{\lambda_k}\right)}, \end{aligned} \tag{5.70}$$

as appropriate for essentially rigid motion. At high temperature, as $\beta \to 0$, one may perform an expansion of $\pm k_{\mathrm{B}}T \ln\langle\exp(\pm\beta V); \bar{x}\rangle$ in orders of $\beta|V_{\mathrm{1D}}|$, being a cumulant expansion for the effective potential[4][14]. The real periodic on-site potential is expanded in a Fourier series

$$V_{\mathrm{1D}}(x) = \mathrm{Re}\sum_{\mathrm{p}\in\mathbb{Z}} \tilde{\mathrm{V}}_{\mathrm{p}} \mathrm{e}^{\mathrm{i}2\pi\mathrm{p}x/\mathrm{L}} \tag{5.71}$$

[4] As the energy of the system can at most increase linearly with N, the n^{th} term in the expansion $\ln\langle\exp(\pm\beta V); \bar{x}\rangle$ is of order $N(\beta|V_{\mathrm{1D}}|)^n$, giving the convergence criteria $\beta|V_{\mathrm{1D}}| < 1$.

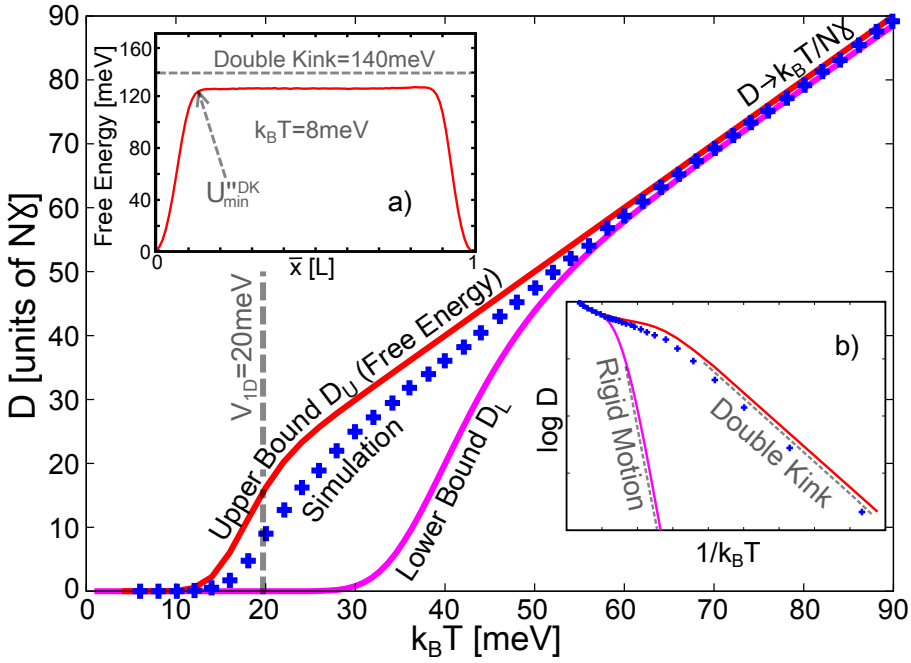

Figure 5.7.: Diffusivity of a 40 particle Sine-Gordon chain. The upper and lower bounds, equations (5.63) and (5.60), agree with simulation and (5.72) at high temperature and capture many important features at intermediate temperature. The diffusivity rises sharply once the thermal energy is greater than the particle barrier $|V_{1D}|$ (see main text). Inset a): The free energy barrier at low temperature. After a sharp nucleation period, the plateau represents kink pair separation. When the kink energy is comparable to the particle barrier, the plateau energy oscillates with the kink migration barrier[1]. Inset b): Arrhenius plot of the diffusivity along with the low temperature limits (5.68) and (5.70). The upper bound gives the correct kink pair activation energy.

and then use identities of Gaussian integrals and the definition (5.65) to write, to order $|\beta V_{1D}|$

$$F_{L,U}(\bar{x}) \xrightarrow[\beta\to 0]{} N\mathrm{Re}\sum_{p\in\mathbb{Z}} \tilde{V}_p e^{i2\pi px/L} e^{-p^2\sigma}, \tag{5.72}$$

where $\sigma = \sum_k 4\pi^2 k_B T/L^2\lambda_k$ is the mean squared fluctuation of a free harmonic chain[50]. As σ increases linearly with T, both bounds converge to an effective migration potential which attenuates exponentially fast with increasing temperature. The condition[5] for convergence of this expansion is $\beta|V_{1D}| < 1$ which can occur at temperatures well below the kink pair energy $\sim \sqrt{\lambda_{max}|V_{1D}|}$, where λ_{max} is the largest eigenvalue of $\mathbf{K}$[85].

5.5.4. Stochastic Simulation

To test these limiting expressions, consider the Sine-Gordon chain, a special case of (5.24),

$$U(\mathbf{x}) = \sum_{i=1}^{N} \frac{\kappa}{2a^2}(x_i - x_{i+1})^2 + |V_{1D}| \sin^2\left(\frac{\pi}{L}x_i\right), \tag{5.73}$$

where a is the horizontal spacing of nodes, $x_{N+1} = x_1$ and $\lambda_{k+1} = 4\sqrt{\kappa/a^2}\sin^2(k\pi/N)$[101]. It is well known that equilibrium averages may be obtained by ergodicity from stochastically integrating the overdamped Langevin equation[40]

$$\gamma\dot{x}_i = -\frac{\partial U(\mathbf{x})}{\partial x_i} + \sqrt{2\gamma k_B T}\eta_i(t) \tag{5.74}$$

where the $\{\eta_i(t)\}_{i=1}^N$ are Gaussian random variables of zero mean and variance $\langle\eta_i(t)\eta_j(t')\rangle = \delta_{ij}\delta(t-t')$. Let a, L=1 and choose γ for numerical stability. To show agreement with traditional transition state theory, I set the line tension κ=300meV to be much larger than the particle barrier $|V_{1D}|$=15meV; when κ and $|V_{1D}|$ are comparable, the discrete structure produces a significant kink migration barrier whose effects are reported in detail elsewhere[1]. Whilst the choice of energy units makes these numerical val-

[5] As the energy of the system can at most increase linearly with N, the n^{th} term in the expansion $\ln\langle\exp(\pm\beta V);\bar{x}\rangle$ is of order $N(\beta|V_{1D}|)^n$, giving the convergence criteria $\beta|V_{1D}| < 1$.

ues appropriate for a dislocation line the phenomenology the model exhibits is general and widely reported[85]. In particular, the exponential prefactor becomes inversely length dependent due to the lack of any Goldstone mode.

Using a high quality random number generator[89] to produce trajectories of $\sim 10^{11}$ timesteps, the average value of a function $f(\mathbf{x})$ was recorded for a value of $\bar{x} \in [0, L]$ to produce a Monte-Carlo evaluation of $\langle f(\mathbf{x}); \bar{x} \rangle$. To evaluate the free energy $F_{\mathrm{U}}(\bar{x})$ a histogram of center of mass values $\bar{x} \in [0, L]$ was populated to produce $Z_\lambda \langle \exp(-\beta U); \bar{x} \rangle = \exp(-\beta F_{\mathrm{U}}(\bar{x}))$. The results of these simulations are displayed in Figure (5.7), showing that the diffusivity is indeed bounded by (5.63) and (5.60). The free energy upper bound can be seen to provide a reasonable and qualitatively accurate approximation to the diffusivity at intermediate temperatures and, importantly, gives the correct activation energy at low temperature. The high temperature expansion (5.72) also becomes increasingly accurate once the thermal energy exceeds the particle barrier such that the convergence criterion $\beta |V_{1\mathrm{D}}| < 1$ is satisfied.

5.5.5. Non-Linear Response

To end, a DC bias f is applied to the FK chain, such that the one dimensional on-site potential becomes $V_{1\mathrm{D}}(x) - fx$. The effect of this bias is to break the symmetry of the system, meaning that the center of mass will drift with a velocity $\dot{\bar{\chi}}$. In the absence of any on site potential, it is simple to show that the free drift velocity is f/γ. Stratonovich[108, 109] found the response of an overdamped point particle to such a bias to be

$$\dot{x}_{1\mathrm{D}}(f) = \frac{L\left(1 - e^{-\beta f L}\right)/\beta\gamma}{\oint e^{-\beta(V_{1\mathrm{D}}(x) - fx)} \int_x^{x+L} e^{\beta(V_{1\mathrm{D}}(y) - fy)} \mathrm{d}y \mathrm{d}x}. \tag{5.75}$$

The effective one dimensional migration potentials $F_{\mathrm{L,U}}(\bar{x})$ implied by the diffusivity bounds suggest bounds $\dot{\bar{\chi}}_{\mathrm{L,U}}(f)$ on the non-linear response, through analogy to the Stratonovich result (5.75)

$$\dot{\bar{\chi}}_{\mathrm{L,U}}(f) = \frac{L\left(1 - e^{-\beta N f L}\right)/\beta N\gamma}{\oint e^{-\beta(F_{\mathrm{U}}(\bar{x}) - Nf\bar{x})} \int_{\bar{x}}^{\bar{x}+L} e^{\beta(F_{\mathrm{L,U}}(\bar{y}) - Nf\bar{y})} \mathrm{d}\bar{y} \mathrm{d}\bar{x}}, \tag{5.76}$$

These bounds have been compared to stochastic simulation as before; typical results are displayed in Figure (5.8). At low temperature the true result

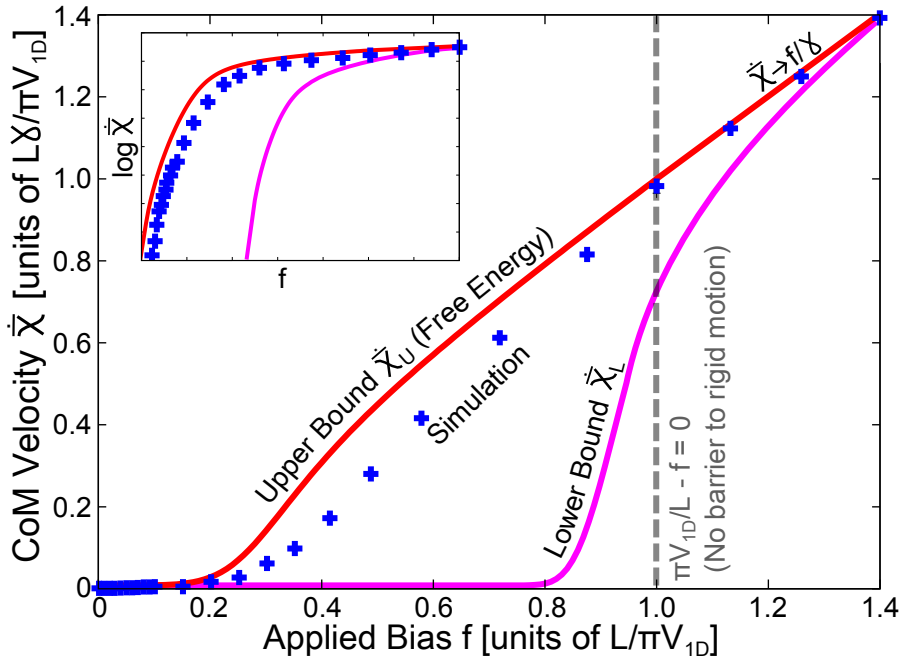

Figure 5.8.: Non-linear response the same 40 particle Sine-Gordon chain as above at low temperature $k_B T = 6$meV. Inset: log plot showing the low bias response. Whilst the lower bound of (5.76), $\dot{\bar{\chi}}_L$, only agrees at the highest bias, the 'free energy' upper bound $\dot{\bar{\chi}}_U$, is seen to show good agreement. The applied bias is expressed in proportion to the maximum gradient of the sinusoidal substrate potential, $\pi V_{1D}/L$; when $f > 1$ in these units the biased on site potential has no stationary points meaning a drift is expected even at zero temperature. As the bias increases further any affect of the on site potential disappears and one recovers the free drift law $\dot{\bar{\chi}} = f/\gamma$.

is much closer to the 'free energy' upper bound, which again agrees with the transition state theory approximation. At a given temperature, the properties of $\dot{\bar{\chi}}_U$ are identical to the point particle result, which is well documented[106]. This informative approximation to the low temperature non-linear response can be calculated at zero temperature in regimes where transition state theory is expected to apply, as the free energy landscape (5.66) can be calculated from a constrained static minimisation[95].

The main result of this section was that for the simple and widely employed model studied, the Helmholtz free energy landscape only gives a

lower bound for any migration barrier to bulk motion. This result was obtained through diffusively scaling the adjoint Fokker-Planck equation to isolate the long time limit and confirmed through extensive numerical simulation. An analogous relationship was also seen to hold for the non-linear response. Recalling that the free energy is an entropic maximum, it is not altogether surprising that the free energy pathway provides an upper bound on the diffusive transport; due to the simplicity and generality of (5.24), these results will hold for a wide range of physical systems. In future work, it would be interesting, using the approach developed here, to quantify the affect of both inertia and general particle interaction on many-body, non-linear, stochastic transport.

6. The Stochastic Force on Crystal Defects

In the course of this thesis we have seen that highly mobile crystal defects such as crowdions, kinks on screw dislocations and prismatic dislocation loops exhibit an anomalous temperature independent mobility unexplained by phonon scattering analysis. In this final chapter we derive new analytical expressions for the mobility of these defects, without any recourse to elasticity theory. We show how the expressions may be efficiently evaluated in molecular dynamics simulation, giving quantitative accuracy with traditional trajectory analysis, then discuss how a temperature independent mobility arises due to non-integrable effects forbidden in continuum approaches.

To recall the importance of γ we first recall the defect equation of motion $\dot{\mathbf{x}} = \boldsymbol{\gamma}^{-1} \cdot (\mathbf{f} + \boldsymbol{\eta}(t))$, where $\langle \boldsymbol{\eta}(t) \otimes \boldsymbol{\eta}(t') \rangle = 2\mathrm{k_B T} \boldsymbol{\gamma} \delta(t - t')$. This Langevin equation demonstrates that thermal defect motion is swiftly non-inertial and governed by a balance between the stochastic force $\boldsymbol{\eta}(t)$ and the Peach-Koehler 'configurational force' $\mathbf{f}$, which we derive in a new setting below. Crucially, small dislocation loops and point defects only respond to stress gradients[5] meaning the stochastic force is often more significant than the configurational force. For more extended defects the converse usually holds. In both cases $\boldsymbol{\gamma}$ controls the rate of important microstructural processes such as swelling and post-irradiation annealing[7]. As mentioned extensively in the above, no universal theory for $\boldsymbol{\gamma}$ exists.

Phonon scattering calculations (see end of chapter 2) and soliton models[118] predict that $\boldsymbol{\gamma}$ should increase linearly with temperature in the classical regime (i.e. $\boldsymbol{\gamma}$=$\mathrm{k_B T} \boldsymbol{\gamma}_\mathrm{w}$ where γ_w is a constant). Whilst this 'phonon wind' relationship is seen to hold, with varying degrees of quantitative agreement,

in molecular dynamics (MD) simulations of extended glissile dislocation lines[80, 69], no theory has explained the widely observed[50, 1, 47, 79, 65] temperature *independent* mobility ($\boldsymbol{\gamma} = \boldsymbol{\gamma}_0$) of glissile defects such as crowdions, kinks and prismatic dislocation loops, which exhibit the highly stochastic trajectories particularly sensitive to $\boldsymbol{\gamma}$.

To resolve this issue we start from a more general conceptual framework than the scattering theory approaches of the past. Using the Zwanzig projection technique[40], we find $\boldsymbol{\gamma}$ emerges as the time autocorrelation function of the projected defect force. We provide an accurate and efficient scheme to calculate this function in MD simulations and analytically evaluate $\boldsymbol{\gamma}$ without recourse to elasticity. In quantitative agreement with MD simulations of defects and dislocations, we find $\boldsymbol{\gamma} = \boldsymbol{\gamma}_0 + \mathrm{k_B T}\boldsymbol{\gamma}_\mathrm{w}$, where $\boldsymbol{\gamma}_0$ and $\boldsymbol{\gamma}_\mathrm{w}$ are given explicitly as tensorial derivatives of the potential energy of the defective crystal. We show that $\boldsymbol{\gamma}_0$ arises because the defect displacement vector is not an eigenvector of the Hessian, which is assumed implicitly in all previous treatments. We relate the relative magnitudes of $\boldsymbol{\gamma}_0$ and $\boldsymbol{\gamma}_\mathrm{w}$ to properties of the defect core structure. This manifestation of discreteness and non-integrability is reminiscent, though independent of, the Peierls barrier to dislocation motion[18].

6.1. Defect coordinates

We describe a crystal using a 3N-dimensional vector of atomic positions $\mathbf{X} \in \mathbb{R}^{3\mathrm{N}}$ and velocities $\dot{\mathbf{X}} \in \mathbb{R}^{3\mathrm{N}}$. In this treatment crystal defects are not elastic singularities but localised deformations, which may be assigned a set of $\mathrm{M} \ll \mathrm{N}$ 'position' labels $\mathbf{x}_\lambda \in \mathbb{R}^{3\mathrm{M}}$ and 'velocity' labels $\dot{\mathbf{x}}_\lambda \in \mathbb{R}^{3\mathrm{M}}$ to characterize the state of a defective crystal. Common methods for determining $\mathbf{x}_\lambda, \dot{\mathbf{x}}_\lambda$ include analysis of the atomic disregistry[6] or an energy filter[1], though in the following the only requirement is a repeatable protocol. By definition, the zero temperature configurations $\mathbf{X}{=}\mathbf{U}(\mathbf{x}_\lambda)$ of the crystal potential energy $V(\mathbf{X})$ may be entirely characterised by the parameters $\mathbf{x}_\lambda$, while variation of $\mathbf{U}(\mathbf{x}_\lambda)$ with $\mathbf{x}_\lambda$ can be determined through nudged elastic band calculations[84] or simply a finite difference derivative in the case of a defect with a wide core. To complete the discrete representation

of a crystal at finite temperature, we must include displacements due to thermal vibrations $\mathbf{\Phi} \in \mathbb{R}^{3N}$. The crystal configuration $\mathbf{X}$ at any given instant can now be expressed as

$$\mathbf{X} = \mathbf{\Phi} + \mathbf{U}(\mathbf{x}_\lambda)\,,\ \dot{\mathbf{X}} = \dot{\mathbf{\Phi}} + \dot{\mathbf{x}}_\lambda \cdot \boldsymbol{\partial}_\lambda \mathbf{U}(\mathbf{x}_\lambda), \tag{6.1}$$

where $\boldsymbol{\partial}_\lambda \mathbf{U} = \boldsymbol{\partial}/\boldsymbol{\partial}\mathbf{x}_\lambda \otimes \mathbf{U}(\mathbf{x}_\lambda) \in \mathbb{R}^{3M\times 3N}$. By introducing a defect position and velocity the coordinate set $\mathbf{\Phi} \oplus \dot{\mathbf{\Phi}} \oplus \mathbf{x}_\lambda \oplus \dot{\mathbf{x}}_\lambda$ has 6M more dimensions than $\mathbf{X} \oplus \dot{\mathbf{X}}$. To rectify this we require the vibrational displacements $\mathbf{\Phi}$ to be independent to the displacements caused by defect motion $\boldsymbol{\partial}_\lambda \mathbf{U}$, giving the 6M constraints[118]

$$\boldsymbol{\partial}_\lambda \mathbf{U} \cdot \mathbf{\Phi} = 0 \quad , \quad \boldsymbol{\partial}_\lambda \mathbf{U} \cdot \dot{\mathbf{\Phi}} = 0. \tag{6.2}$$

To obtain a dynamical equation for $\mathbf{x}_\lambda$, it now suffices[119] to project the exact equation of motion $m\ddot{\mathbf{X}} = -\boldsymbol{\nabla} V(\mathbf{X})$ onto the direction orthogonal to the crystal vibrations $\boldsymbol{\partial}_\lambda \mathbf{U}$. Defining an effective mass tensor $\tilde{\mathbf{m}} = m\boldsymbol{\partial}_\lambda \mathbf{U} \cdot (\boldsymbol{\partial}_\lambda \mathbf{U})^{\mathrm{T}}$, we exploit the time invariance of (6.2) to obtain $\tilde{\mathbf{m}} \cdot \ddot{\mathbf{x}}_\lambda - \dot{\mathbf{x}}_\lambda \cdot \boldsymbol{\partial}_\lambda^2 \mathbf{U} \cdot \dot{\mathbf{\Phi}} = -\boldsymbol{\partial}_\lambda (V + \dot{\mathbf{x}}_\lambda \cdot \tilde{\mathbf{m}} \cdot \dot{\mathbf{x}}_\lambda/2)$. Similar equations of motion are standard in dynamical quasiparticle theories[118, 119] and in common with other authors we will neglect the 'hydrodynamic' term $-\dot{\mathbf{x}}_\lambda \cdot \boldsymbol{\partial}_\lambda^2 \mathbf{U} \cdot \dot{\mathbf{\Phi}}$ and the effective kinetic energy gradient $-\dot{\mathbf{x}}_\lambda \cdot \boldsymbol{\partial}_\lambda \tilde{\mathbf{m}} \cdot \dot{\mathbf{x}}_\lambda/2$. This is justified as we consider the motion of only subsonic defects, and it can be shown that these terms are of order $|\dot{\mathbf{x}}_\lambda|/c \ll 1$, where c is the speed of sound. As a result, the defect coordinates evolve according to

$$\mathbf{m} \cdot \ddot{\mathbf{x}}_\lambda = \mathbf{f}_\lambda \equiv -\boldsymbol{\partial}_\lambda \mathbf{U} \cdot \boldsymbol{\nabla} V(\mathbf{X})\Big|_{\mathbf{X}=\mathbf{U}(\mathbf{x}_\lambda)+\mathbf{\Phi}}, \tag{6.3}$$

where we have defined the instantaneous defect force $\mathbf{f}_\lambda$ as the projection of the total force $-\boldsymbol{\nabla} V$ in the direction of defect motion $\boldsymbol{\partial}_\lambda \mathbf{U}$. The vibrational coordinates evolve in the subspace orthogonal to $\boldsymbol{\partial}_\lambda \mathbf{U}$, implying that $m\ddot{\mathbf{\Phi}} = -\left(\mathbb{I} - m(\boldsymbol{\partial}_\lambda \mathbf{U})^T \cdot \tilde{\mathbf{m}}^{-1} \cdot \boldsymbol{\partial}_\lambda \mathbf{U}\right) \cdot \boldsymbol{\nabla} V \equiv -\boldsymbol{\nabla}_{\mathbf{\Phi}} V$.

6.2. Relation to Eshelby's force on a singularity and the Peach-Koehler force

In the presence of weak external tractions $\mathbf{F}$ far from the defect core, $\mathbf{f}_\lambda$ is precisely the configurational force on a crystal defect first derived by Eshelby[120]. To see this, we vary the total energy

$$E = V(\mathbf{x}_\lambda) + \mathbf{F} \cdot \mathbf{U}(\mathbf{x}_\lambda), \tag{6.4}$$

to obtain $\mathbf{f}_\lambda = \mathbf{F} \cdot \boldsymbol{\partial}_\lambda \mathbf{U}(\mathbf{x}_\lambda)$.

The requirement that $\mathbf{F}$ is weak and applied far from the defect core is to ensure the linearity in $\mathbf{F}$ of the total energy (6.4); if the pertubation was non-linear the continuously parametrised set of minimum energy configurations $\mathbf{U}(\mathbf{x}_\lambda)$ would not be a global minimum in the presence of an external traction. We note that equivalence between elasticity and a fully non-linear discrete treatment is only expected to apply in this regime, but it is precisely these conditions that are realised in the vast majority of experimental observations.
To explicitly apply a surface traction, let $\mathbf{F}$ represent a force of $\pm A\hat{\mathbf{n}}\cdot\boldsymbol{\sigma} \in \mathbb{R}^3$ per atom for two bounding planes $\Sigma_\pm$, where A is the area per atom. The defect force is now

$$\mathbf{f}_\lambda = A \sum_{i \in \Sigma_+, \Sigma_-} \hat{\mathbf{n}} \cdot \boldsymbol{\sigma} \cdot \boldsymbol{\partial}_\lambda \mathbf{u}^i, \tag{6.5}$$

which has a continuum limit

$$\mathbf{f}_\lambda = \int_{\Sigma_+, \Sigma_-} \mathrm{d}\mathbf{S} \cdot \sigma \cdot \partial_\lambda \mathbf{u}(S), \tag{6.6}$$

where $\partial_\lambda \mathbf{u}(S)$ is the continuum interpolation of $\boldsymbol{\partial}_\lambda \mathbf{u}^i$, in direct agreement with Eshelby's result.

We now derive the Peach-Koehler force in this discrete framework. Consider an isolated straight dislocation of Burgers vector $\mathbf{b}$ lying along a lattice direction $\mathbf{t}$ between two bounding planes $\Sigma_\pm$ of normal $\pm\hat{\mathbf{n}}$ perpendicular to $\mathbf{t}$ and $\pm\hat{\mathbf{n}}$. A force of $\pm A\hat{\mathbf{n}} \cdot \boldsymbol{\sigma} \in \mathbb{R}^3$ per atom is applied to these planes, where $\boldsymbol{\sigma}$ is constant, inducing dislocation motion in the direct of the lattice

vector $\mathbf{a}$.

As before, in order to reconcile our non-linear discrete picture with elasticity, we require the bounding planes to be sufficiently far from the dislocation core to ensure that the displacement field is slowly varying, allowing us to make the finite difference approximation

$$\boldsymbol{\partial}_\lambda \mathbf{u}^i = \left(\mathbf{u}^{i+1} - \mathbf{u}^i - \mathbf{a}\right) \otimes \mathbf{a}/|\mathbf{a}|^2 + \mathrm{O}(|\delta\mathbf{u}|^2_\lambda), \tag{6.7}$$

where the indexing is chosen such that in a perfect crystal $\mathbf{x}^{i+1} - \mathbf{x}^i = \mathbf{a}$.

We recall that in this notation the conventional Peach-Koehler force per unit length of dislocation line reads[22]

$$\tilde{\mathbf{f}}^{\mathrm{PK}} = \hat{\mathbf{t}} \times \boldsymbol{\sigma} \cdot \mathbf{b}, \tag{6.8}$$

i.e the dislocation moves in a direction perpendicular to the line direction. However, it is important to note that the migration direction $\mathbf{a}$ need not be perpendicular to the line direction $\hat{\mathbf{t}}$. Whilst the glide motion of an infinitely long straight dislocation line in an elastic medium is contrained to one dimension by a continuous translation symmetry along the line direction, in a discrete crystal this symmetry becomes *discrete*. This introduces a two dimensional Peierls barrier *in the slip plane*, a new concept that is briefly explored above in the context of M111 dislocations. We now lack the vector calculus manipulations and continuum virtual work arguments used to derive the Peach-Koehler force. In general, we will only obtain agreement with the continuum Peach-Koehler force if we translate by a lattice vector to discount any work against the Peierls barrier and only consider the virtual work done perpendicular to the line direction along $|\mathbf{a}\times\hat{\mathbf{t}}|$, as the virtual work done parallel to the line direction has no equivalent in standard elasticity theory.

With these admissions, the discrete virtual work reads

$$\mathbf{f}_\lambda \cdot \mathbf{a} = |\mathbf{f}^{\mathrm{PK}}_\lambda||\mathbf{a}\times\hat{\mathbf{t}}| = A\left(\hat{\mathbf{n}}\cdot\boldsymbol{\sigma}\cdot\sum_{i\in\Sigma_+}(\mathbf{u}^{i+1}-\mathbf{u}^i-\mathbf{a}) - \hat{\mathbf{n}}\cdot\boldsymbol{\sigma}\cdot\sum_{i\in\Sigma_-}(\mathbf{u}^{i+1}-\mathbf{u}^i-\mathbf{a})\right), \tag{6.9}$$

where $\mathbf{f}^{\mathrm{PK}}_\lambda$ is the discrete Peach-Koehler force, which we are aiming to show

is equivalent to the conventional Peach-Koehler force $\mathbf{f}^{\mathrm{PK}}$. To evaluate (6.9), we partition the summation over $\Sigma_{\pm}$ into single atom wide strips j of $N_{\pm}$ atoms along $\mathbf{a}$, separated by the shortest in-plane lattice vector not equal to $\mathbf{a}$. As the number of strips will scale linearly with the total line length, we can divide the sum along one strip by the line length per atom $A/|\mathbf{a}\times\hat{\mathbf{t}}|$ and by the perpendicular displacement $|\mathbf{a}\times\hat{\mathbf{t}}|$ and thus obtain the magnitude of the force per unit length perpendicular to the dislocation line of $|\tilde{\mathbf{f}}_{\lambda}^{\mathrm{PK}}| = \mathbf{f}_{\lambda}\cdot\mathbf{a}/A$. To show the equivalence $\tilde{\mathbf{f}}_{\lambda}^{\mathrm{PK}} = \tilde{\mathbf{f}}^{\mathrm{PK}}$, we first note that in a perfect lattice we have by definition

$$\sum_{i\in j}(\mathbf{x}_{\lambda}^{i+1} - \mathbf{x}_{\lambda}^{i} - \mathbf{a}) = \mathbf{x}_{\lambda}^{N_{\pm}} - \mathbf{x}_{\lambda}^{0_{\pm}} - N_{\pm}\mathbf{a} = N_{\pm}\mathbf{a} - N_{\pm}\mathbf{a} = 0, \tag{6.10}$$

whilst in the general case the total strip vector $\mathbf{u}_{\lambda}^{N_{\pm}} - \mathbf{u}_{\lambda}^{0_{\pm}}$ will not be identical to the *ideal* strip vector $N_{\pm}\mathbf{a}$, meaning that (6.9) is proportional to the total disregistry $(\mathbf{u}_{\lambda}^{N_{+}} - \mathbf{u}_{\lambda}^{0_{+}} - N_{+}\mathbf{a}) - (\mathbf{u}_{\lambda}^{N_{-}} - \mathbf{u}_{\lambda}^{0_{-}} - N_{-}\mathbf{a})$. However, as the plane normal $\hat{\mathbf{n}}$ is perpendicular to $\hat{\mathbf{t}}$, it is simple to show that $|\hat{\mathbf{n}}\cdot\mathbf{r}| = |\hat{\mathbf{t}}\times\mathbf{r}|$ for any vector $\mathbf{r}$, meaning that, as $\tilde{\mathbf{f}}_{\lambda}^{\mathrm{PK}}$ is defined to be perpendicular to $\hat{\mathbf{t}}$,

$$\tilde{\mathbf{f}}_{\lambda}^{\mathrm{PK}} = \hat{\mathbf{t}}\times\boldsymbol{\sigma}\cdot\left((\mathbf{u}_{\lambda}^{N_{+}} - \mathbf{u}_{\lambda}^{0_{+}} - N_{+}\mathbf{a}) - (\mathbf{u}_{\lambda}^{N_{-}} - \mathbf{u}_{\lambda}^{0_{-}} - N_{-}\mathbf{a})\right), \tag{6.11}$$

which will coincide with $\tilde{\mathbf{f}}^{\mathrm{PK}}$ if the total disregistry $(\mathbf{u}_{\lambda}^{N_{+}} - \mathbf{u}_{\lambda}^{0_{+}} - N_{+}\mathbf{a}) - (\mathbf{u}_{\lambda}^{N_{-}} - \mathbf{u}_{\lambda}^{0_{-}} - N_{-}\mathbf{a}) = \mathbf{b}$.

To show this, we consider an edge and screw dislocation separately, as two results may be linearly combined in the general case. The disregistry can be simply determined in molecular dynamics simulation by introducing an isolated dislocation to an infinite orthorhombic 'slab' periodic in directions normal to the two bounding planes.

For an edge dislocation, a single dislocation can be stably contained in an orthorhombic box with no lattice rotation, meaning that $\mathbf{u}_{\lambda}^{N_{+}} - \mathbf{u}^{0_{+}} = \mathbf{u}_{\lambda}^{N_{-}} - \mathbf{u}^{0_{-}}$, and in a majority of cases the dislocation will glide in the direction of the Burgers vector so that $\mathbf{a} = \mathbf{b} \propto \hat{\mathbf{n}}\times\hat{\mathbf{t}}$. The total disregistry thus becomes $(N_{-} - N_{+})\mathbf{b}$. As there must be one more atomic plane above the slip plane than below, we find that $(\mathbf{u}_{\lambda}^{N_{+}} - \mathbf{u}_{\lambda}^{0_{+}} - N_{+}\mathbf{a}) - (\mathbf{u}_{\lambda}^{N_{-}} - \mathbf{u}_{\lambda}^{0_{-}} - N_{-}\mathbf{a}) = \mathbf{b}$ as required.

For a screw dislocation $N_+ = N_-$; however, through pairwise comparison of strips on different planes the slip plane before and after the Volterra process we can conclude that $\mathbf{u}_\lambda^{N_+} - \mathbf{u}^{0_+} - \mathbf{u}_\lambda^{N_-} - \mathbf{u}^{0_-} = \mathbf{b}$. To see this, consider an atom wide strip perpendicular to the dislocation line with long side $N\mathbf{a}$ and area Nab which before the Volterra process will be identical above and below the slip plane. After the Volterra process, one plane will be left unchanged, whilst the other plane will be sheared to form a parallelogram of area Nab but long side vector $N\mathbf{a}+\mathbf{b}$. Whilst there are of course other choices of strip, the requirement of a change in 'base' strip vector $\mathbf{a}$ will still induce a net disregistry $(\mathbf{u}_\lambda^N - \mathbf{u}_\lambda^0 - N\mathbf{a}) - (\mathbf{u}_\lambda^N - \mathbf{u}_\lambda^0 - N\mathbf{a}) = \mathbf{b}$ as required. We now return to considering the dynamical stochastic aspects of dislocation motion.

6.3. Removing the vibrational coordinates

From the form of the potential energy $V(\mathbf{U}(\mathbf{x}_\lambda)+\mathbf{\Phi})$, it is clear that the evolution of the defect and vibrational coordinates are coupled, as they must be for a frictional force to exist. However, for highly mobile subsonic defects, which necessarily possess a wide defect core[18], the defect coordinates may be considered as slowly varying compared to the vibrational coordinates, a conclusion which will be explicitly demonstrated in molecular dynamics simulation below. Over a Debye period $\tau_{\rm D} \sim a/c \sim$ 0.1ps, where a is the lattice parameter, the displacements of any atom due to thermal vibrations will approximately average to zero, with an oscillation amplitude of $\sim \tau_{\rm D}\sqrt{{\rm k_B T}/m}$. Since the defect speed will be approximately $\dot{x}_\lambda \sim \sqrt{{\rm k_B T}/\tilde{m}} \ll c$, the displacement of any one atom due to defect motion in a time interval $\tau_{\rm D}$ will be at most $\tau_{\rm D}\|\boldsymbol{\partial}_\lambda \mathbf{U}\|_\infty \sqrt{{\rm k_B T}/\tilde{m}}$, where $\|\boldsymbol{\partial}_\lambda \mathbf{U}\|_\infty$ is the largest component of $\boldsymbol{\partial}_\lambda \mathbf{U}$. These calculations imply that if $\|\boldsymbol{\partial}_\lambda \mathbf{U}\|_\infty \ll |\boldsymbol{\partial}_\lambda \mathbf{U}|$, then the displacement due to defect motion will be much less than the magnitude of displacements due to thermal motions, which implies that the $\mathbf{\Phi}$ are effectively ergodic over a timescale $\sim \tau_{\rm D}$ where the defect coordinates are essentially stationary. But the condition $\|\boldsymbol{\partial}_\lambda \mathbf{U}\|_\infty \ll |\boldsymbol{\partial}_\lambda \mathbf{U}|$ amounts to a requirement that the deformation associated with the defect is spread over many atomic sites, which is always satisfied by highly mobile defects with a wide core. We therefore assume that vibrational displacements average to

zero over periods of ∼0.1ps whilst the defect remains effectively stationary, an assumption that we will test explicitly when calculating the defect force autocorrelation.

We can exploit this separation of timescales to remove thermal vibrations from the defect equation of motion using the formalism of dimensional reduction by Zwanzig[40, 41]. In this formalism the solution of the 'fast' equation of motion for $\mathbf{\Phi}$ is substituted into the 'slow' equation of motion for $\mathbf{x}_\lambda$. It may be shown, to order τ_{D}^3, that $\mathbf{\Phi}, \dot{\mathbf{\Phi}}$ are adiabatic with respect to $\mathbf{x}_\lambda, \dot{\mathbf{x}}_\lambda$ and ergodic over the partial Gibbs distribution

$$\langle ... \rangle \equiv Z^{-1}(\mathbf{x}_\lambda) \int_{\mathbf{\Phi}, \dot{\mathbf{\Phi}}} ... \, e^{-\beta \left[V(\mathbf{U}(\mathbf{x}_\lambda) + \mathbf{\Phi}) + m \dot{\mathbf{\Phi}} \cdot \dot{\mathbf{\Phi}} / 2 \right]}, \tag{6.12}$$

where $Z(\mathbf{x}_\lambda) = \exp(-\beta F(\mathbf{x}_\lambda))$ is the partial partition function and we integrate on the hypersurface defined by (6.2). The defect coordinates now evolve on a coarse timescale τ_D and follow the stochastic equation of motion

$$\tilde{\mathbf{m}} \cdot \ddot{\mathbf{x}}_\lambda(t) = -\boldsymbol{\gamma} \cdot \dot{\mathbf{x}}_\lambda(t) + \langle \mathbf{f}_\lambda \rangle + \boldsymbol{\eta}(t). \tag{6.13}$$

It is usual in dislocation dynamics to neglect the inertial term $\tilde{\mathbf{m}} \cdot \ddot{\mathbf{x}}_\lambda(t)$, which is valid when the potential energy landscape is slowly varying over the thermal length $\sqrt{\mathrm{k_B T} / \tilde{m} |\boldsymbol{\gamma}|}$[15]. In (6.13) we have introduced the expected force $\langle \mathbf{f}_\lambda \rangle = -\langle \boldsymbol{\partial}_\lambda V \rangle = -\boldsymbol{\partial}_\lambda F$, the stochastic force $\boldsymbol{\eta}(t)$, where $\langle \boldsymbol{\eta}(t) \otimes \boldsymbol{\eta}(t') \rangle = 2\mathrm{k_B T} \boldsymbol{\gamma} \delta(t - t')$, and our central quantity, the friction matrix $\boldsymbol{\gamma}$. In this timescale separated regime it is a standard result that $\boldsymbol{\gamma}$ is proportional to the time integral of the force autocorrelation $C(\tau)$, namely

$$\boldsymbol{\gamma} \equiv (\mathrm{k_B T})^{-1} \int_0^\infty C(\tau) \mathrm{d}\tau, \tag{6.14}$$

where by ergodicity $C(\tau) \equiv \langle \mathbf{f}_\lambda(\tau) \mathbf{f}_\lambda(0) \rangle - \langle \mathbf{f}_\lambda(0) \rangle^2$ may be expressed as

$$C(\tau) = \lim_{t \to \infty} \left[\int_0^t \frac{\mathbf{f}_\lambda(t' + \tau) \mathbf{f}_\lambda(t')}{t} \mathrm{d}t' - \left(\int_0^t \frac{\mathbf{f}_\lambda(t')}{t} \mathrm{d}t' \right)^2 \right]. \tag{6.15}$$

We evaluate $C(\tau)$, and hence $\boldsymbol{\gamma}$, in two ways: first by deriving in closed form the thermal averages (6.12) and second by numerical calculation of $\mathbf{f}_\lambda(t)$ in MD simulation.

6.4. Analytic derivation

To derive an expression for $\boldsymbol{\gamma}$ we expand the potential energy V and the defect force $\mathbf{f}_\lambda$ in powers of $\boldsymbol{\Phi}$. For the evaluation of the partition function the constraints (6.2) and the requirement that the $\mathbf{U}(\mathbf{x}_\lambda)$ describes the zero temperature configurations results in an expansion

$$V = V(\mathbf{x}_\lambda) + \frac{1}{2}\boldsymbol{\Phi}\cdot\boldsymbol{\nabla}^2_{\boldsymbol{\Phi}}V\cdot\boldsymbol{\Phi} + \frac{1}{3!}\boldsymbol{\Phi}\cdot\boldsymbol{\nabla}^3_{\boldsymbol{\Phi}}V:\boldsymbol{\Phi}\otimes\boldsymbol{\Phi} + ..., \tag{6.16}$$

where all inner products are with respect to $\boldsymbol{\Phi}$ and all partial derivatives are evaluated at $\mathbf{X} = \mathbf{U}(\mathbf{x}_\lambda)$. Although $\boldsymbol{\nabla}_{\boldsymbol{\Phi}}V = 0$ (so that $m\ddot{\boldsymbol{\Phi}} = -\boldsymbol{\nabla}^2_{\boldsymbol{\Phi}}V\cdot\boldsymbol{\Phi} + O(\Phi^2)$) there is no restriction on the existence of *mixed* derivatives $\boldsymbol{\partial}_\lambda\boldsymbol{\nabla}^n_{\boldsymbol{\Phi}}V \neq 0$. This is important as these mixed derivatives couple the defect and vibrational coordinates, as can be seen in the defect force expansion

$$\mathbf{f}_\lambda = \boldsymbol{\partial}_\lambda V(\mathbf{x}_\lambda) + \boldsymbol{\partial}_\lambda\boldsymbol{\nabla}_{\boldsymbol{\Phi}}V\cdot\boldsymbol{\Phi} + \frac{1}{2}\boldsymbol{\partial}_\lambda\boldsymbol{\nabla}^2_{\boldsymbol{\Phi}}V:\boldsymbol{\Phi}\otimes\boldsymbol{\Phi} + ..., \tag{6.17}$$

We now truncate V to quadratic order in $\boldsymbol{\Phi}$ in the Gibbs distribution (6.12), allowing us to explicitly evaluate the expectation values in terms of the 3(N-M) dimensional vibrational eigenset $\{\omega_l, \mathbf{v}_l\}$, where $\boldsymbol{\nabla}^2_{\boldsymbol{\Phi}}V\cdot\mathbf{v}_l = -m\omega_l^2\mathbf{v}_l$.

This truncation neglects any thermal expansion arising from the purely vibrational anharmonicities $\boldsymbol{\nabla}^3_{\boldsymbol{\Phi}}V$,$\boldsymbol{\nabla}^4_{\boldsymbol{\Phi}}V$. In Appendix A.2 we systematically include these terms to produce an expression for $\boldsymbol{\gamma}$ up to linear order in temperature. it is shown that the anomalous temperature independent mobility $\boldsymbol{\gamma}_0$ by these additional terms.

This quadratic approximation means we suppress any thermal expansion $\langle\boldsymbol{\Phi}\rangle \sim \mathrm{k_B T}(\boldsymbol{\nabla}^2_{\boldsymbol{\Phi}}V)^{-1}\cdot\boldsymbol{\nabla}^3_{\boldsymbol{\Phi}}V : (\boldsymbol{\nabla}^2_{\boldsymbol{\Phi}}V)^{-1}$. While it is a straightforward matter to include these terms, they cannot affect the temperature independent mobility and are in general negligible for metals below the melting temperature[30]. Using a quadratic Gibbs distribution, the expected force is found to be $\langle\mathbf{f}_\lambda\rangle = -\boldsymbol{\partial}_\lambda(V - \mathrm{T}S)$, where S is the harmonic entropy $\mathrm{k_B}\sum_l \log\omega_l$[121]; to evaluate $C(\tau)$ we evolve the vibrational coordinates $\boldsymbol{\Phi}$ from a given $\mathbf{x}_\lambda$. This is justified by the timescale separation and achieved by evaluating propagator terms of the form

$$\langle\boldsymbol{\Phi}(t)\otimes\boldsymbol{\Phi}(0)\rangle = \sum_l \frac{\mathrm{k_B T}}{m\omega_l^2}\mathbf{v}_l\otimes\mathbf{v}_l\cos(\omega_l t). \tag{6.18}$$

As appropriate for non-conservative dynamics, the propagator is evaluated using only the initial conditions $\langle \mathbf{\Phi}(0) \otimes \mathbf{\Phi}(0) \rangle = \sum_l \mathrm{k_B T}/m\omega_l^2 \mathbf{v}_l \otimes \mathbf{v}_l$ and consequently is closely related to the *retarded* Green's function $\mathbf{G}(t) = \Theta(t)(\mathrm{k_B T})^{-1} \langle \mathbf{\Phi}(t) \otimes \mathbf{\Phi}(0) \rangle$[122]. All that now remains is to perform elementary Gaussian integrations to obtain our main result

$$\begin{aligned} \boldsymbol{\gamma} = & \int_0^\infty \boldsymbol{\partial}_\lambda \boldsymbol{\nabla}_{\mathbf{\Phi}} V \cdot \mathbf{G}(t) \cdot \boldsymbol{\partial}_\lambda \boldsymbol{\nabla}_{\mathbf{\Phi}} V \, \mathrm{d}t \\ & + \frac{k_\mathrm{B} T}{2} \int_0^\infty \mathrm{Tr} \left(\boldsymbol{\partial}_\lambda \boldsymbol{\nabla}^2_{\mathbf{\Phi}} V \cdot \mathbf{G}(t) \cdot \boldsymbol{\partial}_\lambda \boldsymbol{\nabla}^2_{\mathbf{\Phi}} V \cdot \mathbf{G}(t) \right) \mathrm{d}t \\ & + \frac{k_\mathrm{B} T}{2} \int_0^\infty \boldsymbol{\partial}_\lambda \boldsymbol{\nabla}_{\mathbf{\Phi}} V \cdot \mathbf{G}(t) \cdot \boldsymbol{\partial}_\lambda \boldsymbol{\nabla}^3_{\mathbf{\Phi}} V : \mathbf{G}(t) \, \mathrm{d}t \end{aligned} \tag{6.19}$$

We see that the friction coefficient takes the form $\boldsymbol{\gamma} = \boldsymbol{\gamma}_0 + \mathrm{k_B T} \boldsymbol{\gamma}_\mathrm{w}$, with the new *temperature independent* $\boldsymbol{\gamma}_0$ a function of the mixed quadratic derivative $\boldsymbol{\partial}_\lambda \boldsymbol{\nabla}_{\mathbf{\Phi}} V$, and the temperature dependent $\mathrm{k_B T} \boldsymbol{\gamma}_\mathrm{w}$ a function of the mixed cubic and quartic derivatives $\boldsymbol{\partial}_\lambda \boldsymbol{\nabla}^2_{\mathbf{\Phi}} V$ and $\boldsymbol{\partial}_\lambda \boldsymbol{\nabla}^3_{\mathbf{\Phi}} V$. These terms may in principle be evaluated after diagonalising $\boldsymbol{\nabla}^2_{\mathbf{\Phi}} V$ to obtain $\{\omega_l, \mathbf{v}_l\}$ and computing the tensorial derivatives $\boldsymbol{\partial}_\lambda \boldsymbol{\nabla}^n_{\mathbf{\Phi}} V$ (See Appendix A.3). However, in common with modern methods to evaluate dispersion relations[123], we have found dynamical measurement of the thermal averages to be much more efficient than complete diagonalisation of the vibrational Hessian $\boldsymbol{\nabla}^2_{\Phi} V$.

6.5. Numerical evaluation

We have developed a method to calculate $\mathbf{f}_\lambda(t)$ by MD simulation, which yields $C(\tau)$ and hence $\boldsymbol{\gamma}$, yielding a numerical evaluation of the analytic expressions (6.19). In an ensemble of MD runs, with no stress applied, we time average the output for each run $\mathbf{X}(t)$ using a coarse grained time step between $\tau_D/4$ and τ_D to give $\langle \mathbf{X} \rangle$. To eliminate any errors we find the zero temperature configuration $\mathbf{U}_\lambda$ which minimises $|\boldsymbol{\partial}_\lambda \langle \mathbf{X} \rangle - \boldsymbol{\partial}_\lambda \mathbf{U}|^2$. The calculated $\boldsymbol{\partial}_\lambda \mathbf{U}$ is then used to project out the defect force $\mathbf{f}_\lambda(t) = -\boldsymbol{\partial}_\lambda \mathbf{U} \cdot \boldsymbol{\nabla} V(\mathbf{X}(t))$ over the same averaging time interval that produced $\langle \mathbf{X} \rangle$. We have found this method to be robust to variation in the averaging period and especially efficient for short line segments or nanoscale defects, where the zero temperature structures are typically related by rigid translation[124]. An example of such calculations is shown in Figure 6.1 for

a 7 atom SIA cluster in tungsten, which exhibits the anomalous temperature independent mobility $\boldsymbol{\gamma} = \boldsymbol{\gamma}_0$[65], and in Figure 6.2 for a highly mobile edge dislocation in iron, which exhibits a mixed temperature dependence $\boldsymbol{\gamma} = \gamma_0 + \mathrm{k_B T}\boldsymbol{\gamma}_\mathrm{w}$[47]. In both cases we see that $C(\tau)$ loses all coherence after the first zero at $\sim \tau_\mathrm{D}/2$ over which time the defect is observed to be essentially stationary. This validates our assumption of timescale separation between thermal vibrations and defect motion. We identify the subsequent FAC signal as noise because it flattens with the system and ensemble size, limiting the integration $C(\tau)$ only to the first zero. As shown in the figures this method gives values in excellent agreement with conventional trajectory analysis. We also calculated the FAC for the 7-atom SIA ($\boldsymbol{\partial}_\lambda \boldsymbol{\nabla}_{\boldsymbol{\Phi}} V \cdot \mathbf{G}(t) \cdot \boldsymbol{\partial}_\lambda \boldsymbol{\nabla}_{\boldsymbol{\Phi}} V$) via full diagonalisation of $\boldsymbol{\nabla}^2_{\boldsymbol{\Phi}} V$. We find excellent agreement with the dynamical method, as shown in Figure (6.1).

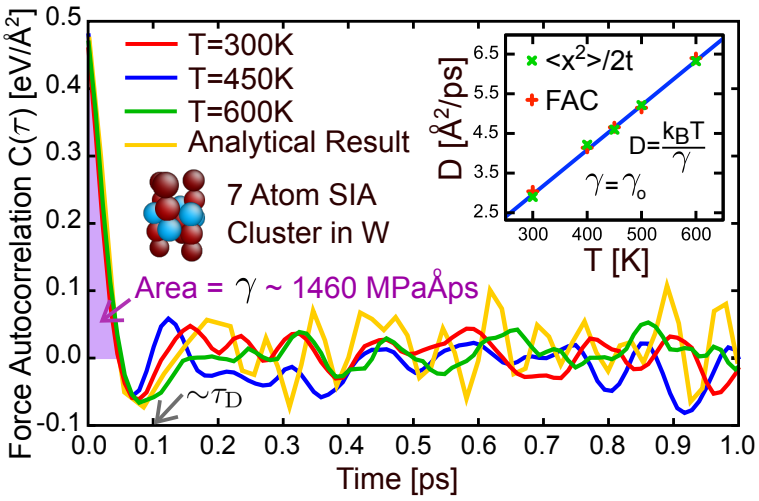

Figure 6.1.: Evalution of the defect force autocorrelation (FAC) in unbiased molecular dynamics simulation at three temperatures and the first analytic term in (6.19) for a 7 atom SIA cluster in tungsten using LAMMPS[51] and an interatomic potential by Marinica *et al.*[43]. We see a very similar peak in all methods which loses coherence after a time period $\sim \tau_D/2$, and we approximate the time integral in (6.19) by the area under this first peak. Inset: Comparison of the predicted diffusivity $D = \mathrm{k_B T}/\gamma$ and the direct measurement $D = \langle x^2 \rangle / 2t$. (Color Online)

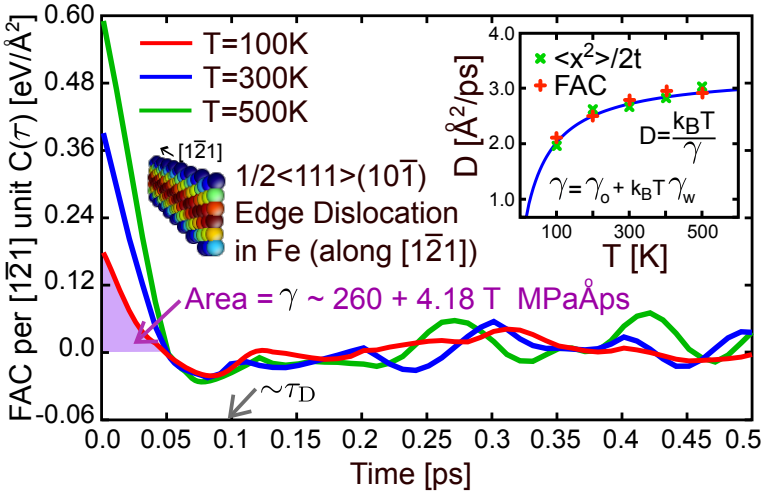

Figure 6.2.: Evaluation of $C(\tau)$ for a $1/2\langle 111\rangle(10\bar{1})$ edge dislocation in Fe, using an interatomic potential by Gordon *et al.*[52], normalised to the unit length $a|[1\bar{2}1]| \sim 7$Å. The FAC increases with temperature such that $\boldsymbol{\gamma}=\boldsymbol{\gamma}_0 + \mathrm{k_B T}\gamma_\mathrm{w}$, exhibiting both anomalous and 'phonon wind' drag. Inset: Comparison with direct measurement of the diffusivity. The values are in quantitative agreement with finite stress simulations[47]. (Color Online)

6.6. Discussion

Terms similar to (6.19) appear in phonon scattering predictions of $\boldsymbol{\gamma}$, where they may be interpreted diagrammatically, with $\boldsymbol{\partial}_\lambda \boldsymbol{\nabla}^n_{\boldsymbol{\Phi}} V$ approximately representing a vertex of one defect with n phonons[33, 125]. In this continuum picture, defects and phonons are separable to harmonic order, conserving energy and momentum in collisions. As a result each term in (6.19) becomes dependent on the phase space available for the scattering process it represents. The anomalous term $\boldsymbol{\gamma}_0$ is forbidden in such models as it represents the pure absorption or emission of a phonon, a process which has a vanishing phase space for subsonic defect speeds due to the linear phonon dispersion relation[125]. It turns out that the second term in (6.19) dominates, describing a two-phonon elastic scattering process known as the 'phonon wind'. With a cubic anharmonicity parameter A[23] this term has an approximate magnitude $\sim \mathrm{k_B T}(A/\mu)^2\tau_D$, where μ is the shear modulus, in agreement with more detailed continuum treatments[33]. However, the prediction $\boldsymbol{\gamma}_0 = 0$ from continuum analysis does not explain the observed

simulation results.

To see how the present treatment allows an anomalous temperature independent mobility, we express $\boldsymbol{\gamma}_0$ in the eigenbasis $\{\mathbf{v}_k\}$ of the vibrational Hessian $\boldsymbol{\nabla}^2_{\boldsymbol{\Phi}} V$. Using (6.18) and the expansion $\boldsymbol{\partial}_\lambda \boldsymbol{\nabla}_{\boldsymbol{\Phi}} V = \sum_k \mathbf{v}_k \boldsymbol{\partial}_\lambda \nabla_k V$, where $\nabla_k = \mathbf{v}_k \cdot \boldsymbol{\nabla}_{\boldsymbol{\Phi}}$, the temperature independent component $\boldsymbol{\gamma}_0$ reads $\int_0^\infty \sum_k (\boldsymbol{\partial}_\lambda \nabla_k V)^2/(m\omega_k)^2 \cos(\omega_k t) \mathrm{d}t$. For this term to vanish, as in all continuum theories, we require $\boldsymbol{\partial}_\lambda \nabla_k V = 0$. But this implies that the defect displacement operator $\boldsymbol{\partial}_\lambda \mathbf{U}$ is an eigenvector of the total Hessian $\boldsymbol{\nabla}^2 V$ as the 'off-diagonal' terms $\boldsymbol{\partial}_\lambda \nabla_k V$ that mix $\boldsymbol{\partial}_\lambda \mathbf{U}$ and the vibrational modes must vanish. We have explicitly demonstrated that this is not the case; it is precisely this effect, which relies on the weaker identification of a defect as a localised deformation that is not an eigenvector of the Hessian, in contrast to a canonical quantity separable from vibrations, that gives rise to $\boldsymbol{\gamma}_0$. Of course, anharmonic vibrations still affect the dynamics in a manner which becomes analogous to typical scattering theories in a continuum picture, giving the 'phonon wind' term $\mathrm{k_B T} \boldsymbol{\gamma}_{\mathrm{w}}$ in (6.19). These terms are appreciable for only extended line dislocations which significantly deform the host lattice, while the anomalous $\boldsymbol{\gamma}_0$ is the leading term for nanoscale defects which are typically elastically neutral in the far field. For some extended dislocations in close packed crystals the defect translational operator is very nearly an eigenvector of the Hessian, implying that the anomalous mobility vanishes and $\boldsymbol{\gamma} \sim \mathrm{k_B T} \boldsymbol{\gamma}_{\mathrm{w}}$[80]. But in general we have found this not to be the case, with the mixed dependence $\boldsymbol{\gamma} = \boldsymbol{\gamma}_0 + \mathrm{k_B T} \boldsymbol{\gamma}_{\mathrm{w}}$ occurring across a wide range of crystal defects.

We believe our explict form for $\boldsymbol{\gamma}$ is a new result. It may be used to parametrise accurately deterministic ($\dot{x} = \boldsymbol{\gamma}^{-1} \cdot \mathbf{f}$) or stochastic ($\dot{x} = \boldsymbol{\gamma}^{-1} \cdot (\mathbf{f} + \boldsymbol{\eta}(t))$) defect mobility laws. The result was obtained by identifying defects through a projection operator with no recourse to elasticity. An anomalous temperature independent mobility $\boldsymbol{\gamma} \sim \gamma_0$ arises because the displacement vector corresponding to defect motion is not an eigenvector of the Hessian, in violation of elasticity theory or soliton-like models, where vibrations are canonical. This finding highlights the importance of intrinsically discrete (i.e. atomistic) analysis to understand nanoscale crystal plasticity. Finally, we note that the form of $\boldsymbol{\gamma}_0$ in (6.19) is closely analogous to the famous Kac-Zwanzig heat bath formula[40]. But rather than a random array of harmonic oscillators with a constant coupling strength we have here the

vibrational modes of the entire crystal coupling to a localised deformation through $\boldsymbol{\partial}_\lambda \boldsymbol{\nabla}_{\boldsymbol{\Phi}} V$.

7. Conclusions and Outlook

A primary goal of this doctoral project was to correctly coarse grain a dislocation to include thermal fluctuations and understand the wide range of behaviour governed by these fluctuations.

To achieve this coarse graining, it became clear that the dislocation line must posses a crystallographically structured nodal discretisation, *and no finer*. This was apparent as the emergent discreteness effects, such as kink migration barriers, could be analytically calculated and explicitly compared to molecular dynamics simulations.

This strongly showed that we must adopt a fundamentally discrete picture to understand defects on the atomic scale. Once adopted, many ambiguities of dislocation theory disappear, at the cost of a more complicated and novel conceptual framework. For example, we found that the structure of a dislocation core is best thought of as periodically repeating 'units'- a concept that has no meaning in a continuum picture. This protocol was essential to understand the formation and migration of M111 dislocations. For example, the core unit model provides a natural explanation for the stability of M111 dislocations despite their increased length in a continuum picture. This protocol also proved central to the developed concepts of the kink vector.

In summary, the results, interpretation and coarse graining of a wide range of molecular dynamics simulations shows that the conventional continuum field theories of elasticity are ill suited to capturing fluctuating nanoscale phenomena of thermal dynamics. This was manifest in the inability of continuum theories to explain the temperature independent mobility of many nanoscale defects.

To resolve this problem we developed a completely new approach, defining the stochastic dynamics of crystal defects through the Zwanzig projection operator technique, with no recourse to elasticity. This technique allowed a first explicit expression for the defect mobility and explained the temperature independent mobility of nanoscale defects, which arose because in all

previous theories friction was introduced as a perturbation to a quadratic Hamiltonian which already contained defects. This implicitly assumed that defect motion is an eigenmode, an assumption we explicitly showed to be false.

In future work we plan to extend this projection operator technique to defects which have a large migration barrier. This is complicated as the timescale separation essential to produce the effective defect Langevin equation cannot be made in the large migration barrier case, as the climbing of large barriers occurs at the wave speed. This means the resultant motion will be not be Markovian and the friction kernel will depend on space and time. The general investigation of such non-Markovian model represent an active area of current research[126].

Returning to the coarse grained models these atomistic techniques are designed to inform, we also made a first rigorous investigation of the stochastic dynamics of the non-linear discrete models which proved essential for thermal defects and have additionally been used in a wide range of fields. Significantly, we found that the free energy landscape with respect to a collective coordinate such as the center of mass will always underestimate the actual mobility of the system with respect to the same collective coordinate. This immediately raises the question 'What reduced equation of motion can give the correct mobility?'. Clearly the answer to this question is closely related to the Zwanzig projection technique, but the relation to the free energy landscape is at first sight unclear.

Future applications of the coarse grained dislocation model we have developed are extensive. In particular, we plan to apply the model to thermally activated shear loop growth in the presence of point defects such as carbon and vacancies, to gain a quantitative understanding of the brittle to ductile transition. More generally, it is hoped the techniques developed in this thesis, in particular our explicit expression for $\boldsymbol{\gamma}$ and the method of its evaluation, may be used to provide further connections between analytic heat bath models and the stochastic thermal dynamics of real systems.

A. Appendices

A.1. Proof of (5.54)

As ρ_∞ and the test functions f, g are periodic and bounded in $\bar{x}$, we may always expand $\sqrt{\rho_\infty} f$ (or $\sqrt{\rho_\infty} g$) as

$$\sqrt{\rho_\infty} f = \sum_{n=0}^{n=\infty} \tilde{f}_n(\{a_k\}) \cos(\frac{2\pi n}{L}\bar{x}) + \tilde{f}_{n+N}(\{a_k\}) \sin(\frac{2\pi n}{L}\bar{x}), \tag{A.1}$$

where we have suppressed any $\bar{\chi}$ or t dependence as they may be considered constant in the following. The normalisation condition (5.41) may now be writen as

$$\frac{L}{2} \sum_{n=0}^{n=\infty} \left(\int_{\{a_k\}} \tilde{f}_n^2(\{a_k\}) + \tilde{f}_{n+N}^2(\{a_k\}) \right) < \infty, \tag{A.2}$$

implying that the real $\tilde{f}_n(\{a_k\})$ must be square integrable functions, i.e. that

$$\int_{\{a_k\}} \tilde{f}_n^2(\{a_k\}) < \infty. \tag{A.3}$$

This means the functions satisfy a Cauchy-Schwartz inequality of the form

$$\left(\int_{\{a_k\}} \tilde{f}_n \tilde{f}_m \right)^2 \leq \left(\int_{\{a_k\}} \tilde{f}_n^2 \right) \left(\int_{\{a_k\}} \tilde{f}_m^2 \right), \tag{A.4}$$

where the arguments of the functions have been omitted for brevity. For each value of $\bar{x} \in [0, L]$ the trigonometric functions in (A.1) may be considered coefficients in a linear sum of square integrable functions. As any linear combination of square integrable functions is also a square integrable function, any two linear combinations will also satisfy a Cauchy-Schwartz inequality of the form (A.4). Taking $\sqrt{\rho_\infty} f$ and $\sqrt{\rho_\infty} g$ for these two linear combinations gives the desired proof of the pointwise inequality (5.54). Note that (5.54) is not derived explicitly from (5.53).

A.2. Full expression for the defect friction including thermal expansion terms

In the main text it was assumed that the Gibbs distribution used to calculate thermal averages was quadratic in the vibrational coordinates. This assumption allowed for anharmonic terms in the defect-vibrational coupling, but did not allow for the purely vibrational anharmonic terms that account for thermal expansion. In the following we account for these additional anharmonic terms perturbatively, deriving expressions for vibrational expectation values up to quadratic order in temperature. It is shown that our main result, an analytic expression for the anomalous temperature independent component of the defect mobility, is unaffected by the additional anharmonic vibrational terms and it is argued that in general these terms have a negligible effect below the melting temperature. We recall from the main text that all reported molecular dynamics simulations find the classical mobility of highly mobile crystal defects takes the form

$$\boldsymbol{\gamma} = \boldsymbol{\gamma}_0 + \mathrm{k_B T}\boldsymbol{\gamma}_\mathrm{w}. \tag{A.5}$$

It was shown in the main text that $\boldsymbol{\gamma}$ is equal to the integral of the autocorrelation function for the defect force

$$\boldsymbol{\gamma} = (\mathrm{k_B T})^{-1} \int_0^\infty \langle \mathbf{f}_\lambda(t)\mathbf{f}_\lambda(0)\rangle - \langle \mathbf{f}_\lambda(t)\rangle\langle \mathbf{f}_\lambda(0)\rangle \mathrm{d}t, \tag{A.6}$$

where the defect force is given by

$$\mathbf{f}_\lambda = \boldsymbol{\partial}_\lambda V(\mathbf{x}_\lambda) + \boldsymbol{\partial}_\lambda \boldsymbol{\nabla}_{\boldsymbol{\Phi}} V \cdot \boldsymbol{\Phi} + \frac{1}{2}\boldsymbol{\partial}_\lambda \boldsymbol{\nabla}^2_{\boldsymbol{\Phi}} V : \boldsymbol{\Phi}\otimes\boldsymbol{\Phi} + \frac{1}{3!}\boldsymbol{\Phi}\cdot\boldsymbol{\partial}_\lambda \boldsymbol{\nabla}^3_{\boldsymbol{\Phi}} V : \boldsymbol{\Phi}\otimes\boldsymbol{\Phi} + ... \tag{A.7}$$

Our task is to evaluate the autocorrelation function for the defect force including all possible terms up to quadratic order in temperature in order to produce an analytical expression for the defect mobility up to linear order in temperature.

In principle, the thermal averages $\langle ... \rangle$ are taken over all initial configu-

rations $\mathbf{\Phi}_0, \dot{\mathbf{\Phi}}_0$ consistent with a fixed defect position $\mathbf{x}_\lambda$, namely

$$\langle ... \rangle \equiv Z^{-1}(\mathbf{x}_\lambda) \int_{\mathbf{\Phi}_0, \dot{\mathbf{\Phi}}_0} ... \, e^{-\beta \left[V(\mathbf{U}(\mathbf{x}_\lambda)+\mathbf{\Phi}) + m\dot{\mathbf{\Phi}}\cdot\dot{\mathbf{\Phi}}/2 \right]}, \tag{A.8}$$

where potential energy at fixed $\mathbf{x}_\lambda$ reads

$$V(\mathbf{U}(\mathbf{x}_\lambda)+\mathbf{\Phi}) = V + \frac{1}{2}\mathbf{\Phi}\cdot\boldsymbol{\nabla}^2_{\mathbf{\Phi}} V \cdot \mathbf{\Phi} + \frac{1}{3!}(\mathbf{\Phi}\otimes\mathbf{\Phi}) : \boldsymbol{\nabla}^3_{\mathbf{\Phi}} V \cdot \mathbf{\Phi} + \frac{1}{4!}(\mathbf{\Phi}\otimes\mathbf{\Phi}) : \boldsymbol{\nabla}^4_{\mathbf{\Phi}} V : (\mathbf{\Phi}\otimes\mathbf{\Phi}) + ... \tag{A.9}$$

We have suppressed the argument in $V(\mathbf{U}(\mathbf{x}_\lambda))$ for clarity.

Before making any assumptions about the nature of the thermal expectation values it is straightforward to show that the autocorrelation function for the defect force is given to quartic order in the vibrations by (using the shorthand $\mathbf{\Phi}(t) = \mathbf{\Phi}_t$ and $0 \leftrightarrow t$ for repeated expressions with an interchange of $0, t$)

$$\begin{aligned}
&\langle \mathbf{f}_\lambda(t)\mathbf{f}_\lambda(0)\rangle - \langle \mathbf{f}_\lambda(t)\rangle\langle \mathbf{f}_\lambda(0)\rangle = \boldsymbol{\partial}_\lambda\boldsymbol{\nabla}_{\mathbf{\Phi}} V \cdot (\langle \mathbf{\Phi}_t \otimes \mathbf{\Phi}_0\rangle - \langle \mathbf{\Phi}_t\rangle \otimes \langle \mathbf{\Phi}_0\rangle) \cdot \boldsymbol{\partial}_\lambda\boldsymbol{\nabla}_{\mathbf{\Phi}} V \\
&+ \frac{1}{2}\boldsymbol{\partial}_\lambda\boldsymbol{\nabla}_{\mathbf{\Phi}} V \cdot (\langle \mathbf{\Phi}_t \otimes \mathbf{\Phi}_t \otimes \mathbf{\Phi}_0\rangle - \langle \mathbf{\Phi}_t \otimes \mathbf{\Phi}_t\rangle \otimes \langle \mathbf{\Phi}_0\rangle + 0 \leftrightarrow t) \cdot \boldsymbol{\partial}_\lambda\boldsymbol{\nabla}^2_{\mathbf{\Phi}} V \\
&+ \frac{1}{4}\boldsymbol{\partial}_\lambda\boldsymbol{\nabla}^2_{\mathbf{\Phi}} V : (\langle \mathbf{\Phi}_t \otimes \mathbf{\Phi}_t \otimes \mathbf{\Phi}_0 \otimes \mathbf{\Phi}_0\rangle - \langle \mathbf{\Phi}_t \otimes \mathbf{\Phi}_t\rangle \otimes \langle \mathbf{\Phi}_0 \otimes \mathbf{\Phi}_0\rangle) : \boldsymbol{\partial}_\lambda\boldsymbol{\nabla}^2_{\mathbf{\Phi}} V \\
&+ \frac{1}{6}\boldsymbol{\partial}_\lambda\boldsymbol{\nabla}^3_{\mathbf{\Phi}} V \cdot : (\langle \mathbf{\Phi}_t \otimes \mathbf{\Phi}_t \otimes \mathbf{\Phi}_t \otimes \mathbf{\Phi}_0\rangle - \langle \mathbf{\Phi}_t \otimes \mathbf{\Phi}_t \otimes \mathbf{\Phi}_t\rangle \otimes \langle \mathbf{\Phi}_0\rangle + 0 \leftrightarrow t) \cdot \boldsymbol{\partial}_\lambda\boldsymbol{\nabla}_{\mathbf{\Phi}} V
\end{aligned} \tag{A.10}$$

In the main text we curtailed the vibrational potential to quadratic order in $\mathbf{\Phi}$ allowing analytical evaluations of thermal averages over the multivariate Gaussian distribution

$$\langle ... \rangle_0 \equiv Z^{-1}(\mathbf{x}_\lambda) \int_{\mathbf{\Phi}_0, \dot{\mathbf{\Phi}}_0} ... \, e^{-\beta \left[\mathbf{\Phi}\cdot\boldsymbol{\nabla}^2_{\mathbf{\Phi}} V \cdot \mathbf{\Phi}/2 + m\dot{\mathbf{\Phi}}\cdot\dot{\mathbf{\Phi}}/2 \right]}, \tag{A.11}$$

so that we can evaluate the retarded Green's function $\mathbf{G}(t)$ in terms of the eigenset $\{\omega_l, \mathbf{v}_l\}$:

$$\mathbf{G}(t) \equiv \Theta(t)(\mathrm{k_B T})^{-1}\langle \mathbf{\Phi}_t \otimes \mathbf{\Phi}_0\rangle_0 = \Theta(t) \sum_l \frac{\cos(\omega_l t)}{m\omega_l^2} \mathbf{v}_l \otimes \mathbf{v}_l. \tag{A.12}$$

Using Wick's theorem to reduce all expectation values to products of Green's

functions we can immediately write the defect mobility to linear order in temperature under the harmonic vibration approximation as

$$\begin{aligned}
\boldsymbol{\gamma} &= \boldsymbol{\gamma}_0 + \mathrm{k_B T}\boldsymbol{\gamma}_\mathrm{w} \\
\boldsymbol{\gamma}_0 &= \int_0^\infty \boldsymbol{\partial}_\lambda \boldsymbol{\nabla}_{\boldsymbol{\Phi}} V \cdot \mathbf{G}(t) \cdot \boldsymbol{\partial}_\lambda \boldsymbol{\nabla}_{\boldsymbol{\Phi}} V \mathrm{d}t \\
\boldsymbol{\gamma}_\mathrm{w} &= \int_0^\infty \frac{1}{2} \mathrm{Tr} \boldsymbol{\partial}_\lambda \boldsymbol{\nabla}^2_{\boldsymbol{\Phi}} V \cdot \mathbf{G}(t) \cdot \boldsymbol{\partial}_\lambda \boldsymbol{\nabla}^2_{\boldsymbol{\Phi}} V \cdot \mathbf{G}(0) + \mathbf{G}(0) : \boldsymbol{\partial}_\lambda \boldsymbol{\nabla}^3_{\boldsymbol{\Phi}} V \cdot \mathbf{G}(t) \cdot \boldsymbol{\partial}_\lambda \boldsymbol{\nabla}_{\boldsymbol{\Phi}} V \mathrm{d}t
\end{aligned} \tag{A.13}$$

which is precisely the result quoted in the main text.

We are now in a position to account for the purely vibrational anharmonicities analytically by expanding the full Gibbs distribution (A.8) to leading order in $\boldsymbol{\nabla}^{3,4}_{\boldsymbol{\Phi}} V$, resulting in an approximate thermal average in terms of quadratic averages (A.11)

$$\begin{aligned}
\langle ... \rangle \simeq &\left(\langle ... \rangle_0 - \frac{\beta}{3!} \langle (\boldsymbol{\Phi}_0 \otimes \boldsymbol{\Phi}_0) : \boldsymbol{\nabla}^3_{\boldsymbol{\Phi}} V \cdot \boldsymbol{\Phi}_0 ... \rangle_0 - \frac{\beta}{4!} \langle (\boldsymbol{\Phi}_0 \otimes \boldsymbol{\Phi}_0) : \boldsymbol{\nabla}^4_{\boldsymbol{\Phi}} V : (\boldsymbol{\Phi}_0 \otimes \boldsymbol{\Phi}_0) ... \rangle_0 \right) \\
&\times \left(1 + \frac{\mathrm{k_B T}}{8} \mathbf{G}(0) : \boldsymbol{\nabla}^4_{\boldsymbol{\Phi}} V : \mathbf{G}(0) \right),
\end{aligned} \tag{A.14}$$

where the last term comes from the change in the partition function. This gives expectation values of (again using Wick's theorem)

$$\langle \boldsymbol{\Phi}_t \rangle = -\frac{\mathrm{k_B T}}{2} \mathbf{G}(0) : \boldsymbol{\nabla}^3_{\boldsymbol{\Phi}} V \cdot \mathbf{G}(t) - \frac{(\mathrm{k_B T})^2}{16} (\mathbf{G}(0) : \boldsymbol{\nabla}^4_{\boldsymbol{\Phi}} V : \mathbf{G}(0)) \mathbf{G}(0) : \boldsymbol{\nabla}^3_{\boldsymbol{\Phi}} V \cdot \mathbf{G}(t) + O(\mathrm{T}^3), \tag{A.15}$$

$$\langle \boldsymbol{\Phi}_t \otimes \boldsymbol{\Phi}_0 \rangle = \mathrm{k_B T} \mathbf{G}(t) - \frac{(\mathrm{k_B T})^2}{2} \mathbf{G}(t) \cdot \big(\mathbf{G}(0) : \boldsymbol{\nabla}^4_{\boldsymbol{\Phi}} V \big) \cdot \mathbf{G}(0) + O(\mathrm{T}^3) \tag{A.16}$$

$$\langle \boldsymbol{\Phi}_t \otimes \boldsymbol{\Phi}_t \rangle = \mathrm{k_B T} \mathbf{G}(0) - \frac{(\mathrm{k_B T})^2}{2} \mathbf{G}(t) \cdot \big(\mathbf{G}(0) : \boldsymbol{\nabla}^4_{\boldsymbol{\Phi}} V \big) \cdot \mathbf{G}(t) + O(\mathrm{T}^3) \tag{A.17}$$

$$\langle \boldsymbol{\Phi}_t \otimes \boldsymbol{\Phi}_t \otimes \boldsymbol{\Phi}_0 \rangle = -\frac{(\mathrm{k_B T})^2}{2} \big(\mathbf{G}(0) : \boldsymbol{\nabla}^3_{\boldsymbol{\Phi}} V \cdot \mathbf{G}(t) \big) \otimes \mathbf{G}(t) - \frac{(\mathrm{k_B T})^2}{8} \big(\mathbf{G}(0) : \boldsymbol{\nabla}^3_{\boldsymbol{\Phi}} V \cdot \mathbf{G}(0) \big) \otimes \mathbf{G}(0) + O(\mathrm{T}^3) \tag{A.18}$$

$$\langle \boldsymbol{\Phi}_t \otimes \boldsymbol{\Phi}_0 \otimes \boldsymbol{\Phi}_0 \rangle = -\frac{(\mathrm{k_B T})^2}{2} \left(\mathbf{G}(0) : \boldsymbol{\nabla}^3_{\boldsymbol{\Phi}} V \cdot \mathbf{G}(0) \right) \otimes \mathbf{G}(t) - \frac{(\mathrm{k_B T})^2}{8} \left(\mathbf{G}(0) : \boldsymbol{\nabla}^3_{\boldsymbol{\Phi}} V \cdot \mathbf{G}(t) \right) \otimes \mathbf{G}(0) + O(T^3) \tag{A.19}$$

whilst higher order expectation values are unaffected by the additional terms to quadratic order in temperature.

It is a straight forward matter to substitute these expressions in the formal result (A.10) to obtain a complete expression for the defect mobility up to linear order in temperature including the effects of thermal expansion. The rather lengthy resulting expression reads

$$\begin{aligned}
&\boldsymbol{\gamma} = \boldsymbol{\gamma}_0 + \mathrm{k_B T} \boldsymbol{\gamma}_{\mathrm{w}} + O(\mathrm{T}^2) \\
&\boldsymbol{\gamma}_0 = \int_0^\infty \boldsymbol{\partial}_\lambda \boldsymbol{\nabla}_{\boldsymbol{\Phi}} V \cdot \mathbf{G}(t) \cdot \boldsymbol{\partial}_\lambda \boldsymbol{\nabla}_{\boldsymbol{\Phi}} V \mathrm{d}t \\
&\boldsymbol{\gamma}_{\mathrm{w}} = \int_0^\infty \frac{1}{2} \mathrm{Tr} \boldsymbol{\partial}_\lambda \boldsymbol{\nabla}^2_{\boldsymbol{\Phi}} V \cdot \mathbf{G}(t) \cdot \boldsymbol{\partial}_\lambda \boldsymbol{\nabla}^2_{\boldsymbol{\Phi}} V \cdot \mathbf{G}(0) + \mathbf{G}(0) : \boldsymbol{\partial}_\lambda \boldsymbol{\nabla}^3_{\boldsymbol{\Phi}} V \cdot \mathbf{G}(t) \cdot \boldsymbol{\partial}_\lambda \boldsymbol{\nabla}_{\boldsymbol{\Phi}} V \\
&- \frac{1}{2} \boldsymbol{\partial}_\lambda \boldsymbol{\nabla}_{\boldsymbol{\Phi}} V \cdot \left(\mathbf{G}(t) \cdot \left(\mathbf{G}(0) : \boldsymbol{\nabla}^4_{\boldsymbol{\Phi}} V \right) \cdot \mathbf{G}(0) + \frac{1}{2} \mathbf{G}(0) : \boldsymbol{\nabla}^3_{\boldsymbol{\Phi}} V \cdot \mathbf{G}(t) \otimes \mathbf{G}(0) : \boldsymbol{\nabla}^3_{\boldsymbol{\Phi}} V \cdot \mathbf{G}(0) \right) \cdot \boldsymbol{\partial}_\lambda \boldsymbol{\nabla}_{\boldsymbol{\Phi}} V \\
&+ \frac{1}{4} \boldsymbol{\partial}_\lambda \boldsymbol{\nabla}^2_{\boldsymbol{\Phi}} V : \left(\frac{3}{4} \mathbf{G}(0) \otimes \mathbf{G}(0) : \boldsymbol{\nabla}^3_{\boldsymbol{\Phi}} V \cdot \mathbf{G}(0) - (\frac{1}{4} \mathbf{G}(0) + \mathbf{G}(t)) \otimes \mathbf{G}(0) : \boldsymbol{\nabla}^3_{\boldsymbol{\Phi}} V \cdot \mathbf{G}(t) \right) \cdot \boldsymbol{\partial}_\lambda \boldsymbol{\nabla}_{\boldsymbol{\Phi}} V \mathrm{d}t
\end{aligned} \tag{A.20}$$

We now highlight important points drawn from the above expressions that indicate the additional thermal expansion terms have a negligible effect on defect mobilities below the melting temperature.

Firstly, a central result of the main text is an expression for the anomalous temperature independent component of the mobility $\boldsymbol{\gamma}_0$ that all existing theories of defect mobility fail to capture. This expression is explicitly evaluated after diagonalising the vibrational Hessian and quantitatively agrees with numerical results from molecular dynamics simulation. As can be seen in the above, the additional thermal expansion terms have strictly no effect on $\boldsymbol{\gamma}_0$ meaning this central result is unchanged.

In contrast, for the temperature dependent damping term $\mathrm{k_B T} \boldsymbol{\gamma}_{\mathrm{w}}$ it can be seen that there are are many additional terms due to thermal expansion. However, we note that all of the additional thermal expansion terms are of at

least cubic order in the Green's fuction $\mathbf{G}$, meaning that they approximately represent a four body interaction process (one body being the defect itself). If such high order interaction processes were of appreciable magnitude we would expect to see significant thermal expansion as well as a quadratic temperature dependence in the defect mobility (just as three body processes contribute to $\mathrm{k_B T}\boldsymbol{\gamma}_{\mathrm{w}}$), neither of which was observed in our simulations or in the large body of existing work. Consequently we believe that the succinct form for $\boldsymbol{\gamma}_{\mathrm{w}}$ presented in (A.13) and the main text captures all the relevant physical processes.

A.3. Tensorial derivatives of an embedded atom potential

The potential energy for a set of atoms $\{\mathbf{x}^i\}$ interacting through an embedded atom potential are typically of the form

$$U(\{\mathbf{x}^i\}) = U_1[\lambda] - U_{1/2}[\omega] \quad , \quad U_C[\phi] = \sum_i \left(\sum_{j \neq i} \phi(r^{ij}) \right)^C \equiv \sum_i \Theta_i^C, \tag{A.21}$$

where $r^{ij} = |\mathbf{x}^i - \mathbf{x}^j| > 0$ is the Euclidean distance between atoms i and j, λ is a pair potential term and ω, the keystone of the embedded atom method, represents the electronic density. In practice these potential terms are neglected once r^{ij} exceeds some cut-off radius $r_{\max}$.

A.3.1. Derivatives of the pairing function ϕ

The embedded atom potential (A.21) is built from pair-potential functions $\phi(|\mathbf{x}_i - \mathbf{x}_j|) = \phi^{ij}$ between pairs ij. To simplify later notation, we now define the first, second, third and fourth derivatives, which by the translational invariance of the argument will have permutation symmetry in the cartesian

directions $\alpha, \beta, \gamma, \epsilon \in (x, y, z)$-

$$\chi^{ij}_{\alpha} \equiv \frac{\partial \phi^{ij}}{\partial x^i_\alpha} = -\frac{\partial \phi^{ij}}{\partial x^j_\alpha} = \chi^{[ij]}{}_{\alpha}, \quad \Rightarrow \frac{\partial \Theta^C_i}{\partial x^k_\alpha} = C\Theta^{C-1}_i \sum_m \chi^{[km]}_\alpha (\delta_{ik} + \delta_{im}) \tag{A.22}$$

$$\Psi^{ij}_{\alpha\beta} \equiv \frac{\partial \chi^{ij}_\alpha}{\partial x^i_\beta} = -\frac{\partial \chi^{ij}_\alpha}{\partial x^j_\beta} = \frac{\partial \chi^{ji}_\alpha}{\partial x^j_\beta} = \Psi^{(ij)}_{(\alpha\beta)}, \quad \Rightarrow \frac{\partial \chi^{[ij]}_\alpha}{\partial x^k_\beta} = (\delta_{ik} - \delta_{jk})\Psi^{(ij)}_{(\alpha\beta)} \tag{A.23}$$

$$\Upsilon^{ij}_{\alpha\beta\gamma} \equiv \frac{\partial \Psi^{ij}_{\alpha\beta}}{\partial x^i_\gamma} = -\frac{\partial \Psi^{ij}_{\alpha\beta}}{\partial x^j_\gamma} = \Upsilon^{[ij]}_{(\alpha\beta\gamma)} \quad \Rightarrow \frac{\partial \Psi^{(ij)}_{(\alpha\beta)}}{\partial x^k_\gamma} = (\delta_{ik} - \delta_{jk})\Upsilon^{[ij]}_{(\alpha\beta\gamma)} \tag{A.24}$$

$$\Xi^{ij}_{\alpha\beta\gamma\epsilon} \equiv \frac{\partial \Upsilon^{ij}_{\alpha\beta\gamma}}{\partial x^i_\epsilon} = -\frac{\partial \Upsilon^{ij}_{\alpha\beta\gamma}}{\partial x^j_\epsilon} = \Xi^{(ij)}_{(\alpha\beta\gamma\epsilon)} \quad \Rightarrow \frac{\partial \Upsilon^{[ij]}_{(\alpha\beta\gamma)}}{\partial x^k_\epsilon} = (\delta_{ik} - \delta_{jk})\Xi^{(ij)}_{(\alpha\beta\gamma\epsilon)}, \tag{A.25}$$

where $[], ()$ indicate the antisymmetric and symmetric permutation symmetry. Practically, the Cartesian derivatives $\chi, \Psi, \Upsilon, \Xi$ of $\phi(r)$ are evaluated in spherical polar coordinates though we omit these standard results as there is quite enough algebra already. To aid the following, we also define the 'reduced' quantities

$$\bar{\Theta}^{C-n}_i \equiv \frac{C!}{(C-n)!}\Theta^{C-n}_i \quad , \quad \bar{\chi}^i_\alpha \equiv \sum_m \chi^{im}_\alpha \quad , \quad \bar{\Psi}^i_{\alpha\beta} \equiv \sum_m \Psi^{im}_{\alpha\beta} \quad \text{etc.}$$
$$\frac{\partial \bar{\Psi}^i_{\alpha\beta}}{\partial x^k_\gamma} = \delta_{ik}\bar{\Upsilon}^i_{\alpha\beta\gamma} - \Upsilon^{ik}_{\alpha\beta\gamma} \quad \text{etc.} \tag{A.26}$$

A.3.2. First and Second Derivatives

With these definitions, we can immediately write

$$\frac{\partial U_C}{\partial x^i_\alpha} = C\sum_m \Theta^{C-1}_m \frac{\partial \Theta_m}{\partial x^i_\alpha} = C\sum_m \Theta^{C-1}_m \sum_n \chi^{[in]}_\alpha (\delta_{mi} + \delta_{mn}) = C\sum_m \chi^{[im]}_\alpha (\Theta^{C-1}_i + \Theta^{C-1}_m), \tag{A.27}$$

$$\begin{aligned}\frac{\partial^2 U_C}{\partial x_\alpha^i \partial x_\beta^j} &= C\sum_m \frac{\partial \chi_\alpha^{[im]}}{\partial x_\beta^j}(\Theta_i^{C-1} + \Theta_m^{C-1}) + C(C-1)\sum_m \chi_\alpha^{[im]}(\frac{\partial \Theta_i}{\partial x_\beta^j}\Theta_i^{C-2} + \frac{\partial \Theta_m}{\partial x_\beta^j}\Theta_m^{C-1}) \\ &= C\sum_m \Psi_{\alpha\beta}^{(im)}(\delta_{ij} - \delta_{mj})(\Theta_i^{C-1} + \Theta_m^{C-1}) \\ &+ C(C-1)\sum_{mn} \chi_\alpha^{[im]}\chi_\beta^{[jn]}(\delta_{ij} + \delta_{in})\Theta_i^{C-2} + \chi_\alpha^{[im]}\chi_\beta^{[jn]}(\delta_{mj} + \delta_{mn})\Theta_m^{C-2}\end{aligned} \tag{A.28}$$

Which in our reduced notation reads

$$\begin{aligned}\frac{\partial U_C}{\partial x_\alpha^i} &= \bar{\chi}_\alpha^i \bar{\Theta}_+^{C-1}\sum_m \chi_\alpha^{im}\bar{\Theta}_i^{C-1}, \\ \frac{\partial^2 U_C}{\partial x_\alpha^i \partial x_\beta^j} &= -\Psi_{\alpha\beta}^{(ij)}(\bar{\Theta}_i^{C-1} + \bar{\Theta}_j^{C-1}) + \sum_m \chi_\alpha^{im}\chi_\beta^{jm}\bar{\Theta}_m^{C-2} \\ &+ \sum_{(p\bar{\alpha},q\bar{\beta})\in\mathbb{P}(i\alpha,j\beta)} \chi_{\bar{\alpha}}^{pq}\bar{\chi}_{\bar{\beta}}^{q}\bar{\Theta}_q^{C-2} + \delta_{ij}\left(\bar{\Psi}_{\alpha\beta}^i\bar{\Theta}_i^{C-1} + \sum_m \Psi_{\alpha\beta}^{im}\bar{\Theta}_m^{C-1} + \bar{\chi}_\alpha^i\bar{\chi}_\beta^i\Theta_i^{C-2},\right)\end{aligned} \tag{A.29}$$

where the index-coordinate permutation sum is explicitly

$$(p\bar{\alpha}, q\bar{\beta}) = (i\alpha, j\beta), (j\beta, i\alpha). \tag{A.30}$$

As any analytic partial derivative must be invariant to the order of differentiation, it will be advantageous to group terms in higher order derivatives as sums over such index-coordinate permutations. The overbars on the Greek coordinate symbols are used to distinguish them from the coordinate symbols outside of such sums.

A.3.3. Third Derivative

The above expressions represent a more succinct representation of results derived elsewhere. We now continue to higher derivatives, using the rules and notation developed above. Whilst the intermediate algebra is lengthy, it is straightforward and therefore omitted in the interest of clarity. The permuation operation will now generate the six terms

$$\mathbb{P}^3 : (p\bar{\alpha}, q\bar{\beta}, r\bar{\gamma}) = (i\alpha, j\beta, k\gamma), (i\alpha, k\gamma, j\beta), (j\beta, k\gamma, i\alpha), (j\beta, i\alpha, k\gamma), (k\gamma, i\alpha, j\beta), (k\gamma, j\beta, i\alpha). \tag{A.31}$$

This significant reduction in the number of terms allows us to write the third order tensorial derivative as

$$\begin{aligned}\frac{\partial^3 U_C}{\partial x^i_\alpha \partial x^j_\beta \partial x^k_\gamma} &= \delta_{ijk}\left(\bar{\Upsilon}^i_{\alpha\beta\gamma}\bar{\Theta}^{C-1}_i + \sum_m \Upsilon^{im}_{\alpha\beta\gamma}\bar{\Theta}^{C-1}_m + \bar{\Psi}^i_{(\alpha\beta}\bar{\chi}^i_{\gamma)}\bar{\Theta}^{C-2}_i + \bar{\chi}^i_\alpha\bar{\chi}^i_\beta\bar{\chi}^i_\gamma\bar{\Theta}^{C-3}_i\right) \\ &+ \sum_m \chi^{im}_\alpha\chi^{jm}_\beta\chi^{km}_\gamma\bar{\Theta}^{C-3}_m + \sum_{\forall\mathbb{P}^3}\Psi^{pq}_{\bar{\alpha}\bar{\beta}}\chi^{pr}_{\bar{\gamma}}\bar{\Theta}^{C-2}_p + \frac{1}{2!}\bar{\chi}^p_{\bar{\alpha}}\chi^{pq}_{\bar{\beta}}\chi^{pr}_{\bar{\gamma}}\bar{\Theta}^{C-3}_p \\ &+ \sum_{\forall\mathbb{P}^3}\frac{1}{2!}\delta_{pq}\left(-\Upsilon^{pr}_{\bar{\alpha}\bar{\beta}\bar{\gamma}}(\bar{\Theta}^{C-1}_p + \bar{\Theta}^{C-1}_r) + \sum_m \Psi^{pm}_{\bar{\alpha}\bar{\beta}}\chi^{rm}_{\bar{\gamma}}\Theta^{C-2}_m + \Psi^{pr}_{\bar{\alpha}\bar{\beta}}\bar{\chi}^r_{\bar{\gamma}}\bar{\Theta}^{C-2}_r\right) \\ &- \frac{1}{2!}\delta_{pq}\left(\Psi^{pr}_{\bar{\gamma}(\bar{\beta}}\bar{\chi}^p_{\bar{\alpha})}\bar{\Theta}^{C-2}_p + \bar{\Psi}^p_{\bar{\alpha}\bar{\beta}}\chi^{pr}_{\bar{\gamma}}\bar{\Theta}^{C-2}_p + \bar{\chi}^p_{\bar{\alpha}}\bar{\chi}^p_{\bar{\beta}}\chi^{pr}_{\bar{\gamma}}\bar{\Theta}^{C-3}_p\right),\end{aligned} \tag{A.32}$$

where $\delta_{ijk} = \delta_{ij}\delta_{jk}$ is a 'rank three' diagonal tensor. Parentheses around coordinates imply expansions such as

$$-\Psi^{pr}_{\gamma(\beta}\bar{\chi}^p_{\alpha)}\bar{\Theta}^{C-2}_p = -\Psi^{pr}_{\gamma\beta}\bar{\chi}^p_\alpha\bar{\Theta}^{C-2}_p - \Psi^{pr}_{\gamma\alpha}\bar{\chi}^p_\beta\bar{\Theta}^{C-2}_p, \tag{A.33}$$

with similar expansions for $(\alpha\beta\gamma)$. In the above, every term inside a permutation sum is degenerate under a *single* coordinate swap, and so have multiplicity of 2! (If we included the other terms in a permutation sum, their complete permutation symmetry would in this case give them a multiplicity of $3! = 6$). This means that the total permutation sum could be replaced by the cyclic permutation sum in this case of three variables. However, when we go to the fourth derivative, the combination of higher order delta functions and more complicated terms will destroy this equivalence.

A.3.4. Fourth Derivative

Clearly the longest expression, the fourth derivative reads

$$
\begin{aligned}
\frac{\partial^4 U_C}{\partial x^i_\alpha \partial x^j_\beta \partial x^k_\gamma \partial x^l_\epsilon} &= \delta_{ijkl}\left(\bar{\Xi}^i_{\alpha\beta\gamma\epsilon}\bar{\Theta}^{C-1}_i + \sum_m \Xi^{im}_{\alpha\beta\gamma\epsilon}\bar{\Theta}^{C-1}_m + \left(\bar{\Upsilon}^i_{(\alpha\beta\gamma}\bar{\chi}^i_{\epsilon)} + \bar{\Psi}^i_{(\alpha\beta}\bar{\Psi}^i_{\gamma\epsilon)}\right)\bar{\Theta}^{C-2}_i\right) \\
&+ \delta_{ijkl}\left(\bar{\Psi}^i_{(\alpha\beta}\bar{\chi}^i_\gamma\bar{\chi}^i_{\epsilon)}\bar{\Theta}^{C-3}_i + \bar{\chi}^i_\alpha\bar{\chi}^i_\beta\bar{\chi}^i_\gamma\bar{\chi}^i_\epsilon\bar{\Theta}^{C-4}_i\right) \\
&+ \sum_{\forall\mathbb{P}^4}\frac{1}{3!}\delta_{pqr}\left(-\Xi^{ps}_{\bar{\alpha}\bar{\beta}\bar{\gamma}\bar{\epsilon}}\left[\bar{\Theta}^{C-1}_p + \bar{\Theta}^{C-1}_s\right] + \sum_m \Upsilon^{pm}_{\bar{\alpha}\bar{\beta}\bar{\gamma}}\chi^{sm}_{\bar{\epsilon}}\bar{\Theta}^{C-2}_m + \Upsilon^{ps}_{\bar{\alpha}\bar{\beta}\bar{\gamma}}\bar{\chi}^s_{\bar{\epsilon}}\bar{\Theta}^{C-2}_s\right) \\
&- \sum_{\forall\mathbb{P}^4}\frac{1}{3!}\delta_{pqr}\left(\bar{\chi}^p_{\bar{\alpha}}\bar{\chi}^p_{\bar{\beta}}\bar{\chi}^p_{\bar{\gamma}}\bar{\chi}^{ps}_{\bar{\epsilon}}\bar{\Theta}^{C-4}_p - \left[\Upsilon^{ps}_{\bar{\epsilon}(\bar{\alpha}\bar{\beta}}\bar{\chi}^p_{\bar{\gamma})} + \bar{\Upsilon}^p_{\bar{\alpha}\bar{\beta}\bar{\gamma}}\chi^{ps}_{\bar{\epsilon}} + \Psi^{ps}_{\bar{\epsilon}(\bar{\alpha}}\bar{\Psi}^p_{\bar{\beta}\bar{\gamma})}\right]\bar{\Theta}^{C-2}_p\right) \\
&+ \sum_{\forall\mathbb{P}^4}\frac{1}{3!}\delta_{pqr}\left(\left[\bar{\Psi}^p_{(\bar{\alpha}\bar{\beta}}\bar{\chi}^p_{\gamma)}\chi^{ps}_{\bar{\epsilon}} + \Psi^{pr}_{\bar{\epsilon}(\bar{\alpha}}\bar{\chi}^p_\beta\bar{\chi}^p_{\bar{\gamma})}\right]\bar{\Theta}^{C-3}_p\right) + \sum_m \chi^{im}_\alpha\chi^{jm}_\beta\chi^{km}_\gamma\chi^{lm}_\epsilon\bar{\Theta}^{C-4}_m \\
&+ \sum_{\forall\mathbb{P}^4}\frac{1}{2!2!}\delta_{pq}\delta_{rs}\left(\Xi^{pr}_{\bar{\alpha}\bar{\beta}\bar{\gamma}\bar{\epsilon}}\bar{\Theta}^{C-1}_p - \Upsilon^{pr}_{\bar{\alpha}\bar{\beta}(\bar{\gamma}}\bar{\chi}^r_{\bar{\epsilon})}\bar{\Theta}^{C-2}_r + \bar{\Psi}^p_{\bar{\alpha}\bar{\beta}}\Psi^{pr}_{\bar{\gamma}\bar{\epsilon}}\bar{\Theta}^{C-2}_p + \bar{\chi}^p_{\bar{\alpha}}\bar{\chi}^p_{\bar{\beta}}\Psi^{pr}_{\bar{\gamma}\bar{\epsilon}}\bar{\Theta}^{C-3}_p\right) \\
&+ \sum_{\forall\mathbb{P}^4}\frac{1}{2!2!}\delta_{pq}\delta_{rs}\left(\frac{1}{2}\sum_m \Psi^{pm}_{\bar{\alpha}\bar{\beta}}\Psi^{rm}_{\bar{\gamma}\bar{\epsilon}}\bar{\Theta}^{C-2}_m\right) \\
&+ \sum_{\forall\mathbb{P}^4}\frac{1}{2!}\delta_{pq}\left(\Upsilon^{pr}_{\bar{\alpha}\bar{\beta}\bar{\gamma}}\left(\chi^{ps}_{\bar{\epsilon}}\bar{\Theta}^{C-2}_p + \chi^{rs}_{\bar{\epsilon}}\bar{\Theta}^{C-2}_r\right) - \Psi^{ps}_{\bar{\alpha}\bar{\beta}}\Psi^{rs}_{\bar{\gamma}\bar{\epsilon}}\bar{\Theta}^{C-2}_s + \Psi^{ps}_{\bar{\alpha}\bar{\beta}}\chi^{rs}_{\bar{\gamma}}\bar{\chi}^s_{\bar{\epsilon}}\bar{\Theta}^{C-3}_s\right) \\
&+ \sum_{\forall\mathbb{P}^4}\frac{1}{2!}\delta_{pq}\Psi^{pr}_{\bar{\gamma}(\bar{\beta}}\bar{\chi}^p_{\bar{\alpha})}\bar{\chi}^{ps}_{\bar{\epsilon}}\bar{\Theta}^{C-3}_p - \frac{1}{2!}\Psi^{pq}_{\bar{\alpha}\bar{\beta}}\chi^{pr}_{\bar{\gamma}}\chi^{ps}_{\bar{\epsilon}}\bar{\Theta}^{C-3}_p \\
&+ \sum_{\forall\mathbb{P}^4}\frac{1}{2!2!}\delta_{pq}\left(\Psi^{pr}_{\bar{\gamma}(\bar{\alpha}}\Psi^{ps}_{\bar{\beta})\bar{\epsilon}}\bar{\Theta}^{C-2}_p + \bar{\Psi}^p_{\bar{\alpha}\bar{\beta}}\chi^{pr}_{\bar{\gamma}}\chi^{ps}_{\bar{\epsilon}}\bar{\Theta}^{C-3}_p + \sum_m \Psi^{pm}_{\bar{\alpha}\bar{\beta}}\chi^{rm}_{\bar{\gamma}}\chi^{sm}_{\bar{\epsilon}}\bar{\Theta}^{C-3}_m\right) \\
&+ \sum_{\forall\mathbb{P}^4}\frac{1}{2!2!}\delta_{pq}\bar{\chi}^p_{\bar{\alpha}}\bar{\chi}^p_{\bar{\beta}}\chi^{pr}_{\bar{\gamma}}\chi^{ps}_{\bar{\epsilon}}\bar{\Theta}^{C-4}_p - \frac{1}{3!}\bar{\chi}^p_{\bar{\alpha}}\chi^{pq}_{\bar{\beta}}\chi^{pr}_{\bar{\gamma}}\chi^{ps}_{\bar{\epsilon}}\bar{\Theta}^{C-4}_p.
\end{aligned}
\tag{A.34}
$$

Phew. The last term can trivially be taken outside the sum, as it has full permutation symmetry.
If you have read this far, we would like to point out that all of this was done by hand as no symbolic algebra program could handle a) the generic form of the pair potential and b) give the massive reduction afforded by the permutational sums.

Depressingly, the above expression cannot be evaluted for many popular

emperical potentials as they use cubic splines which have no fourth derivative. In general a splined function does not satisfy Taylor's theorem, but the complicated function which populated the spline *does*, meaning that to produce the fourth order dynamics in the spline we need knowledge of many different points up to the second derivative rather than the knowledge of four derivatives at one point.

Nevertheless, we have written a code to evalutate the all the above terms via a summing scheme which iterates the indicies of the tensor rather than the terms, a technique which affords massive efficiency savings. This code has been tested on fully analytic potentials such as Sutton-Chen and Lenard-Jones[28]. We plan to release a version of this code in the future these higher order tensorial derivatives have potential application in the study of non-linear vibrational states (glasses,crystalline polymers etc). Thank you for reading.

List of Tables

List of Figures

Bibliography

[1] T D Swinburne, S L Dudarev, S P Fitzgerald, M R Gilbert, and A P Sutton. Theory and simulation of the diffusion of kinks on dislocations in bcc metals. *Physical Review B*, 87(6):64108, 2013.

[2] T D Swinburne. Collective transport in the discrete Frenkel-Kontorova model. *Physical Review E*, 88(1):012135, 2013.

[3] A Stukowski, D Cereceda, T D Swinburne, and J Marian. Thermally-activated non-Schmid glide of screw dislocations in W using atomistically-informed kinetic Monte Carlo simulations. *International Journal of Plasticity*, 65(0):108–130, 2015.

[4] T D Swinburne, S L Dudarev, and A P Sutton. Classical Mobility of Highly Mobile Crystal Defects. *Physical Review Letters*, 113(21):215501, 2014.

[5] J P Hirth and J Lothe. *Theory Of Dislocations*. Malabar, FL Krieger, 1991.

[6] V V Bulatov and W Cai. *Computer Simulations Of Dislocations*. Oxford University Press, 2003.

[7] I Cook. Materials research for fusion energy. *Nature Materials*, 5:77–80, 2006.

[8] D Caillard. Kinetics of dislocations in pure Fe. Part I. In situ straining experiments at room temperature. *Acta Materialia*, 58(9):3493–3503, 2010.

[9] K Arakawa, K Ono, M Isshiki, K Mimura, M Uchikoshi, and H Mori. Observation of the One-Dimensional Diffusion of Nanometer-Sized Dislocation Loops. *Science*, 318(5852):956–959, 2007.

[10] K Arakawa, T Amino, and H Mori. Direct observation of the coalescence process between nanoscale dislocation loops with different Burgers vectors. *Acta Materialia*, 59(1):141–145, 2011.

[11] T S Hudson, S L Dudarev, and A P Sutton. Confinement of interstitial cluster diffusion by oversized solute atoms. *Proceedings of the Royal Society of London. A. Mathematical and Physical Sciences*, 460(2049):2457–2475, 2004.

[12] N N Kumar, P V Durgaprasad, B K Dutta, and G K Dey. Modeling of radiation hardening in ferritic/martensitic steel using multi-scale approach. *Computational Materials Science*, 53(1):258–267, 2012.

[13] T S Hudson, S L Dudarev, M J Caturla, and A P Sutton. Effects of elastic interactions on post-cascade radiation damage evolution in kinetic Monte Carlo simulations. *Philosophical Magazine*, 85(4-7):661–675, 2005.

[14] L E Reichl. *A Modern Course in Statistical Physics*. Physics Textbook. Wiley-VCH, 2009.

[15] W Coffey, Y P Kalmykov, and J T Waldron. *The Langevin Equation: With Applications to Stochastic Problems in Physics, Chemistry, and Electrical Engineering*. World Scientific Series in Contemporary Chemical Physics. World Scientific, 2004.

[16] J A Frenkel. Zur theorie der elastizitätsgrenze und der festigkeit kristallinischer körper. *Zeitschrift für Physik*, 37(7-8):572–609, 1926.

[17] G I Taylor. The mechanism of plastic deformation of crystals. Part I. Theoretical. *Proceedings of the Royal Society of London. A. Mathematical and Physical Sciences*, pages 362–387, 1934.

[18] R E Peierls. The size of a dislocation. *Proceedings of the Royal Society of London*, 52:34, 1940.

[19] X Tang, S Lou, and Y Zhang. Localized excitations in (2+ 1)-dimensional systems. *Physical Review E*, 66(4):46601, 2002.

[20] S Flach. Conditions on the existence of localized excitations in nonlinear discrete systems. *Physical Review E*, 50(4):3134, 1994.

[21] M Lazar and G A Maugin. Nonsingular stress and strain fields of dislocations and disclinations in first strain gradient elasticity. *International Journal of Engineering Science*, 43(13):1157–1184, 2005.

[22] L D Landau and E M Lifshits. *Elasticity Theory*. Pergamon Press, 1975.

[23] D J Bacon, D M Barnett, and R O Scattergood. Anisotropic Continuum Theory of Lattice Defects. Progress in materials science. Pergamon Press, 1978.

[24] J A Dieudonné. *Foundations of modern analysis*, volume 286. Academic press New York, 1960.

[25] H Kleinert. *Gauge Fields in Condensed Matter: disorder fields, phase transitions; Vol. II, Stresses and defects: differential geometry, crystal melting*. World Scientific, 1989.

[26] G Q Xu and M J Demkowicz. Healing of nanocracks by disclinations. *Physical Review Letters*, 111(14):145501, 2013.

[27] D J Griffiths. *Introduction to electrodynamics*, volume 3. prentice Hall Upper Saddle River, NJ, 1999.

[28] A P Sutton and R W Balluffi. *Interfaces In Crystalline Materials*. Monographs on the Physics And Chemistry of Materials. Oxford University Press, USA, 2007.

[29] V Vitek. Theory of the Core Structures of Dislocations in BCC Metals. *Crystal Lattice Defects*, 5(1668):pp. 1–34, 1974.

[30] N W Ashcroft and N D Mermin. *Solid state physics*. Holt-Saunders International Editions: Science : Physics. Holt, Rinehart and Winston, 1976.

[31] S M Keralavarma, T Cagin, A Arsenlis, and A A Benzerga. Power-Law Creep from Discrete Dislocation Dynamics. *Physical Review Letters*, 109(26):265504, 2012.

[32] F R N Nabarro. The Interaction of Screw Dislocations and Sound Waves. *Proceedings of the Royal Society of London. A. Mathematical and Physical Sciences*, 209:278–290, 1951.

[33] V I Alshits and V L Indenbom. Phonon and electron drag of dislocations. In *5 th Internat. Conf. on Internal Friction and Ultrasonic Attenuation in Crystalline Solids, 1975, 2, 162-176*, 1975.

[34] M Lazar and H K Kirchner. Dislocation loops in anisotropic elasticity: displacement field, stress function tensor and interaction energy. *Philosophical Magazine*, pages 1–12, 2012.

[35] M E A Peskin and D V Schroeder. *An Introduction To Quantum Field Theory*. The Advanced Book Program. Basic Books, 1995.

[36] R Brown. XXVII. A brief account of microscopical observations made in the months of June, July and August 1827, on the particles contained in the pollen of plants; and on the general existence of active molecules in organic and inorganic bodies. *The Philosophical Magazine, or Annals of Chemistry, Mathematics, Astronomy, Natural History and General Science*, 4(21):161–173, 1828.

[37] A Einstein. Über die von der molekularkinetischen Theorie der Wärme geforderte Bewegung von in ruhenden Flüssigkeiten suspendierten Teilchen. *Annalen der Physik*, 322(8):549–560, 1905.

[38] F Reif. *Fundamentals of Statistical and Thermal Physics*. McGraw-Hill series in fundamentals of physics. Waveland Press, 2008.

[39] G A Pavliotis and A M Stuart. *Multiscale Methods: Averaging and Homogenization*. Texts in Applied Mathematics. Springer, 2008.

[40] R Zwanzig. *Nonequilibrium Statistical Mechanics*. Oxford University Press, 2001.

[41] A J Chorin, O H Hald, and R Kupferman. Optimal prediction and the Mori-Zwanzig representation of irreversible processes. *Proceedings of the National Academy of Sciences*, 97(7):2968–2973, 2000.

[42] R M Martin. *Electronic Structure: Basic Theory and Practical Methods*. Cambridge University Press, 2004.

[43] M C Marinica, L Ventelon, M R Gilbert, L Proville, S L Dudarev, J Marian, G Bencteux, and F Willaime. Interatomic potentials for

modelling radiation defects and dislocations in tungsten. *Journal of Physics: Condensed Matter*, 25(39):395502, 2013.

[44] M Born and R Oppenheimer. Zur Quantentheorie der Molekeln. *Annalen der Physik*, 389(20):457–484, 1927.

[45] M S Daw and M I Baskes. Embedded-atom method: Derivation and application to impurities, surfaces, and other defects in metals. *Physical Review B*, 29(12):6443, 1984.

[46] A S Argon. *Strengthening Mechanisms in Crystal Plasticity*. Oxford Series on Materials Modelling. Oxford Univ. Press, Oxford, 2008.

[47] S Queyreau, J Marian, M R Gilbert, and B D Wirth. Edge dislocation mobilities in bcc Fe obtained by molecular dynamics. *Physical Review B*, 84(6):64106, 2011.

[48] G. Monnet and D. Terentyev. Structure and mobility of the 12¡111¿112 edge dislocation in BCC iron studied by molecular dynamics. *Acta Materialia*, 57(5):1416–1426, 2009.

[49] D Rodney and L Proville. Stress-dependent Peierls potential: Influence on kink-pair activation. *Physical Review B*, 79(9):94108, 2009.

[50] P M Derlet, M R Gilbert, and S L Dudarev. Simulating dislocation loop internal dynamics and collective diffusion using stochastic differential equations. *Physical Review B*, 84(13):134109, 2011.

[51] S Plimpton. Fast Parallel Algorithms for Short-Range Molecular Dynamics. *Journal Computational Physics*, 117:1–19, 1995.

[52] P A Gordon, T Neeraj, and M I Mendelev. Screw dislocation mobility in BCC Metals: a refined potential description for α-Fe. *Philosophical Magazine*, 91(30):3931–3945, 2011.

[53] E Clouet, L Ventelon, and F Willaime. Dislocation Core Energies and Core Fields from First Principles. *Physical Review Letters*, 102(5):55502, 2009.

[54] V V Bulatov, J F Justo, W Cai, and S Yip. Kink Asymmetry and Multiplicity in Dislocation Cores. *Physical Review Letters*, 79:5042–5045, 1997.

[55] G Wang, A Strachan, T Cagin, and W A Goddard. Atomistic simulations of kinks in 1/2a?111? screw dislocations in bcc tantalum. *Physical Review B*, 68(22):224101, 2003.

[56] L Ventelon, F Willaime, and P Leyronnas. Atomistic simulation of single kinks of screw dislocations in α-Fe. *Journal of Nuclear Materials*, 386388:26–29, 2009.

[57] E Clouet, S Garruchet, H Nguyen, M Perez, and C S Becquart. Dislocation interaction with C in α-Fe: A comparison between atomic simulations and elasticity theory. *Acta Materialia*, 56(14):3450–3460, 2008.

[58] C Li-Qun, W Chong-Yu, and Y Tao. Atomistic simulation of kink structure on edge dislocation in bcc iron. *Chinese Physics B*, 17(2):662, 2008.

[59] J Chang, W Cai, V V Bulatov, and S Yip. Dislocation motion in BCC metals by molecular dynamics. *Materials Science and Engineering: A*, 2001.

[60] S L Dudarev, M R Gilbert, K Arakawa, H Mori, Z Yao, M L Jenkins, and P M Derlet. Langevin model for real-time Brownian dynamics of interacting nanodefects in irradiated metals. *Physical Review B*, 81(22):224107, 2010.

[61] S Lifson and J L Jackson. On the Self-Diffusion of Ions in a Polyelectrolyte Solution. *Journal of Chemical Physics*, 36:2410–2414, 1962.

[62] P Hänggi, P Talkner, and M Borkovec. Reaction-rate theory: fifty years after Kramers. *Reviews of Modern Physics*, 62:251–342, 1990.

[63] A Einstein and R Fürth. *Investigations on the Theory of the Brownian Movement*. Dover Books on Physics. Dover Publications, 1956.

[64] M Abramowitz and I A Stegun. *Handbook of Mathematical Functions: With Formulas, Graphs, and Mathematical Tables*. Applied mathematics series. Dover Publications, 1965.

[65] S L Dudarev. The non-Arrhenius migration of interstitial defects in bcc transition metals. *Comptes Rendus Physique*, 9(34):409–417, 2008.

[66] M R Gilbert, S Queyreau, and J Marian. Stress and temperature dependence of screw dislocation mobility in α-Fe by molecular dynamics. *Physical Review B*, 84(17):174103, 2011.

[67] J Marian, B D Wirth, A Caro, B Sadigh, G R Odette, J M Perlado, and T de la Rubia. Dynamics of self-interstitial cluster migration in pure α-Fe and Fe-Cu alloys. *Physical Review B*, 65(14):144102, 2002.

[68] Z Rong, Y N Osetsky, and D J Bacon. A model for the dynamics of loop drag by a gliding dislocation. *Philosophical Magazine*, 85(14):1473–1493, 2005.

[69] D J Bacon, Y Osetsky, and D Rodney. Dislocations obstacle interactions at the atomic level. In J P Hirth and L Kubin, editors, *Dislocations in Solids*, volume 15, pages 1–90. Elsevier Science, 2009.

[70] G Leibfried. Über den einfluß thermisch angeregter schallwellen auf die plastische deformation. *Zeitschrift für Physik*, 127(4):344–356, 1950.

[71] V Vitek. Core structure of screw dislocations in body-centred cubic metals : relation to symmetry and interatomic bonding. *Philosophical Magazine*, 84:415–428, 2004.

[72] S L Dudarev and P M Derlet. A 'magnetic' interatomic potential for molecular dynamics simulations. *Journal of Physics: Condensed Matter*, 17(44):7097, 2005.

[73] M I Mendelev, S Han, D J Srolovitz, G J Ackland, D Y Sun, and M Asta. Development of new interatomic potentials appropriate for crystalline and liquid iron. *Philosophical Magazine*, 83(35):3977–3994, 2003.

[74] M Itakura, H Kaburaki, and M Yamaguchi. First-principles study on the mobility of screw dislocations in bcc iron. *Acta Materialia*, 60(9):3698–3710, 2012.

[75] L Ventelon and F Willaime. Generalized stacking-faults and screw-dislocation core-structure in bcc iron: A comparison between ab initio calculations and empirical potentials. *Philosophical Magazine*, 90(7-8):1063–1074, 2010.

[76] J Li, C-Z Wang, J Chang, W Cai, V V Bulatov, K-M Ho, and S Yip. Core energy and Peierls stress of a screw dislocation in bcc molybdenum: A periodic-cell tight-binding study. *Physical Review B*, 70(10):104113, 2004.

[77] R G A Veiga, M Perez, C S Becquart, E Clouet, and C Domain. Comparison of atomistic and elasticity approaches for carbon diffusion near line defects in α-iron. *Acta Materialia*, 59(18):6963–6974, 2011.

[78] A Seeger and P Schiller. In W P Mason and R N Thurston, editors, *Physical Acoustics: Principles and Methods*, volume 3 A, chapter 8. Academic Press, New York, 1966.

[79] L A Zepeda-Ruiz, J Rottler, B D Wirth, R Car, and D J Srolovitz. Self-interstitial transport in vanadium. *Acta Materialia*, 53(7):1985–1994, 2005.

[80] E Bitzek and P Gumbsch. Dynamic aspects of dislocation motion: atomistic simulations. *Materials Science and Engineering: A*, 400:40–44, 2005.

[81] M Yamaguchi and V Vitek. Core structure of nonscrew 1/2 (111) dislocations on (110) planes in bcc crystals. I. Core structure in an unstressed crystal. *Journal of Physics F: Metal Physics*, 3(3):523, 1973.

[82] V Vitek and M Yamaguchi. Core structure of nonscrew 1/2 (111) dislocations on (110) planes in bcc crystals. II. Peierls stress and the effect of an external shear stress on the cores. *Journal of Physics F: Metal Physics*, 3(3):537, 1973.

[83] K Kang, V V Bulatov, and W Cai. Singular orientations and faceted motion of dislocations in body-centered cubic crystals. *Proceedings of the National Academy of Sciences*, 109(38):15174–15178, 2012.

[84] G Henkelman, B P Uberuaga, and H Jonsson. A climbing image nudged elastic band method for finding saddle points and minimum energy paths. *The Journal of Chemical Physics*, 113(22):9901–9904, 2000.

[85] O M Braun and Y S Kivshar. Nonlinear dynamics of the FrenkelKontorova model. *Physics Reports*, 306(12):1–108, 1998.

[86] A M Kosevich. *The Crystal Lattice: Phonons, Solitons, Dislocations, Superlattices*. J Wiley & Sons, 2006.

[87] B Joós and M S Duesbery. Dislocation kink migration energies and the Frenkel-Kontorowa model. *Physical Review B*, 55(17):11161–11166, 1997.

[88] A Granato and K Lucke. Theory of Mechanical Damping Due to Dislocations. *Journal of Applied Physics*, 27(6):583–593, 1956.

[89] M Saito and M Matsumoto. SIMD-Oriented Fast Mersenne Twister: a 128-bit Pseudorandom Number Generator. In Alexander Keller, Stefan Heinrich, and Harald Niederreiter, editors, *Monte Carlo and Quasi-Monte Carlo Methods 2006*, pages 607–622. Springer Berlin Heidelberg, 2008.

[90] C A Marchaj. *Sail performance: techniques to maximize sail power*. International Marine/McGraw-Hill, 2002.

[91] L D Landau and E M Lifshits. *The classical theory of fields*, volume 2. Butterworth-Heinemann, 1975.

[92] L Prandtl. Ein Gedankenmodell zur kinetischen Theorie der festen Körper. *ZAMM-Journal of Applied Mathematics and Mechanics/Zeitschrift für Angewandte Mathematik und Mechanik*, 8(2):85–106, 1928.

[93] U Dehlinger. Zur Theorie der Rekristallisation reiner Metalle. *Annalen der Physik*, 394(7):749–793, 1929.

[94] T A Kontorova and Y I Frenkel. On the theory of plastic deformation and twinning I, II. *Zh. Eksp. Teor. Fiz*, 8(89-95):1340–1368, 1938.

[95] L Proville, D Rodney, and M C Marinica. Quantum effect on thermally activated glide of dislocations. *Nature Materials*, 2012.

[96] A Wall, J N Coleman, and M S Ferreira. Physical mechanism for the mechanical reinforcement in nanotube-polymer composite materials. *Physical Review B*, 71(12):125421, 2005.

[97] I Derényi and T Vicsek. Cooperative transport of Brownian particles. *Physical Review Letters*, 75(3):374–377, 1995.

[98] K G Fedorov and A L Pankratov. Crossover of the Thermal Escape Problem in Annular Spatially Distributed Systems. *Physical Review Letters*, 103(26):260601, 2009.

[99] K Fesser. Stochastic motion of Sine-Gordon-solitons and the spin-correlation function of CsNiF 3. *Zeitschrift für Physik B Condensed Matter*, 39(1):47–52, 1980.

[100] N I Gershenzon, V G Bykov, and G Bambakidis. Strain waves, earthquakes, slow earthquakes, and afterslip in the framework of the Frenkel-Kontorova model. *Physical Review E*, 79(5):56601, 2009.

[101] Oleg M Braun and Yuri S Kivshar. *The Frenkel-Kontorova Model: Concepts, Methods, and Applications*. Texts and Monographs in Physics. Springer, 2004.

[102] P Hänggi and F Marchesoni. Artificial Brownian motors: Controlling transport on the nanoscale. *Reviews of Modern Physics*, 81(1):387, 2009.

[103] T Schneider and E Stoll. Long-time behavior and dynamic scaling properties of displacement fluctuations in the sine-Gordon chain. *Physical Review B*, 22(1):395–399, 1980.

[104] F J Alexander, Salman Habib, and A Kovner. Statistical mechanics of kinks in 1+ 1 dimensions: Numerical simulations and double-Gaussian approximation. *Physical Review E*, 48(6):4284, 1993.

[105] S Habib and G Lythe. Dynamics of Kinks: Nucleation, Diffusion, and Annihilation. *Physical Review Letters*, 84(6):1070–1073, 2000.

[106] H Risken. *The Fokker-Planck Equation: Methods of Solution and Applications*. Springer Series in Synergetics Series. Springer-Verlag, 1996.

[107] S Kumar, J M Rosenberg, D Bouzida, R H Swendsen, and P A Kollman. The weighted histogram analysis method for free-energy cal-

culations on biomolecules. I. The method. *Journal of Computational Chemistry*, 13(8):1011–1021, 1992.

[108] P I Kuznetsov, R L Stratonovich, and V I Tikhonov. *Non-linear transformations of stochastic processes*. Pergamon Press, 1965.

[109] R L Stratonovich. *Topics in the theory of random noise*, volume 2. Taylor & Francis US, 1967.

[110] S N Ethier and T G Kurtz. *Markov processes: characterization and convergence*, volume 282. Wiley, 2009.

[111] G A Pavliotis and A Vogiannou. Diffusive transport in periodic potentials: Underdamped dynamics. *Fluctuation and Noise Letters*, 8(02):155–173, 2008.

[112] M Ottobre and G A Pavliotis. Asymptotic analysis for the generalized Langevin equation. *Nonlinearity*, 24(5):1629, 2011.

[113] D Hilbert. Begründung der kinetischen Gastheorie. *Mathematische Annalen*, 72:562–577, 1912.

[114] M Hairer and G A Pavliotis. From ballistic to diffusive behavior in periodic potentials. *Journal of Statistical Physics*, 131(1):175–202, 2008.

[115] P Debye. Näherungsformeln für die Zylinderfunktionen für grosse Werte des Arguments und unbeschränkt veränderliche Werte des Index. *Mathematische Annalen*, 67(4):535–558, 1909.

[116] K Ohsawa and E Kuramoto. Activation energy and saddle point configuration of high-mobility dislocation loops: A line tension model. *Physical Review B*, 72(5):54105, 2005.

[117] H A Kramers. Brownian motion in a field of force and the diffusion model of chemical reactions. *Physica*, 7(4):284–304, 1940.

[118] F Marchesoni, C Cattuto, and G Costantini. Elastic strings in solids: Thermal nucleation. *Physical Review B*, 57(13):7930–7936, 1998.

[119] R Boesch, P Stancioff, and C R Willis. Hamiltonian equations for multiple-collective-variable theories of nonlinear Klein-Gordon

equations: A projection-operator approach. *Physical Review B*, 38(10):6713, 1988.

[120] J D Eshelby. The force on an elastic singularity. *Proceedings of the Royal Society of London. A. Mathematical and Physical Sciences*, 244(877):87–112, 1951.

[121] A P Sutton. Temperature-dependent interatomic forces. *Philosophical Magazine*, 60(2):147–159, 1989.

[122] C R Galley. Classical Mechanics of Nonconservative Systems. *Physical Review Letters*, 110(17):174301, 2013.

[123] L T Kong. Phonon dispersion measured directly from molecular dynamics simulations. *Computer Physics Communications*, 182(10):2201–2207, 2011.

[124] W H Zhou, C G Zhang, Y G Li, and Z Zeng. Creeping motion of self interstitial atom clusters in tungsten. *Scientific Reports*, 4:5096, 2014.

[125] S L Dudarev. Thermal mobility of interstitial defects in irradiated materials. *Physical Review B*, 65(22):224105, 2002.

[126] L Stella, C D Lorenz, and L Kantorovich. Generalized Langevin equation: An efficient approach to nonequilibrium molecular dynamics of open systems. *Physical Review B*, 89(13):134303, 2014.